5-2016

Material Characterization and Finite Element Simulations of Aluminum Alloy Sheets During Non-Isothermal Forming Process

Nan Zhang
Clemson University, nzhang3@g.clemson.edu

MATERIAL CHARACTERIZATION AND FINITE ELEMENT SIMULATIONS OF ALUMINUM ALLOY SHEETS DURING NON-ISOTHERMAL FORMING PROCESS

A Dissertation
Presented to
the Graduate School of
Clemson University

In Partial Fulfillment
of the Requirements for the Degree
Doctor of Philosophy
Automotive Engineering

---

by
Nan Zhang
May 2016

Accepted by:
Dr. Fadi Abu-Farha, Committee Chair
Dr. Srikanth Pilla
Dr. Robert Prucka
Dr. Gang Li

ABSTRACT

The utilization of more non-ferrous materials is one of the key factors to succeed out of the constantly increasing demand for lightweight vehicles in automotive sector. Aluminum-magnesium alloys have been identified as the most promising substitutions to the conventional steel without significant compromise in structural stiffness and strength. However, the conventional forming methods to deform the aluminum alloy sheets are either costly or insufficient in formability which limit the wide applications of aluminum alloy sheets. A recently proposed non-isothermal hot stamping approach, which is also referred as *Hot Blank – Cold Die* (HB-CD) stamping, aims at fitting the commercial grade aluminum alloy sheets, such as AA5XXX and AA7XXX, into high-volume and cost-effective production for automotive sector. In essence, HB-CD is a mutation of the conventional hot stamping approach for boron steel (22MnB5) which deforms the hot blank within the cold tool set. By elevating the operation temperature, the formability of aluminum alloy sheets can be significantly improved. Meanwhile, heating the blank only and deforming within the cold tool sets allow to reduce the energy and time consumed. This research work aims at conducting a comprehensive investigation of HB-CD with particular focuses on material characterization, constitutive modeling and coupled thermo-mechanical finite element simulations with validation.

The material properties of AA5182-O, a popular commercial grade of aluminum alloy sheet in automotive sector, are obtained through isothermal tensile testing at temperatures from 25℃ to 300℃, covering a quasi-static strain-rate range (0.001-0.1s^{-1}). As the state-of-the-art non-contact strain measurement technique, *digital image correlation*

(DIC) system is utilized to evaluate the stress-strain curves as well as to reveal the details of material deformation with full-field and multi-axis strain measurement. Material anisotropy is characterized by extracting the evolving yield stresses and Lankford coefficients (r-value) at various temperatures with specimens in 0^{o}, 45^{o} and 90^{o} to the rolling direction. Besides, thermally-activated deformation mechanisms, dynamic strain ageing and dislocation climb, are identified to control the material deformation at the ambient-to-warm temperature range. For biaxial loading condition, the hydraulic bulge test has been performed and the evaluated effective stress-strain curve is found to be identical to that from uniaxial tests.

A new piece-wised temperature-dependent phenomenological constitutive model has been developed to describe and predict the evolving stress-strain curves within the experimental condition. The power-law model is chosen for temperature ranges from 25℃ to 100℃ where negative strain rate sensitivity is observed. At elevated temperatures, a new model has been developed and expressed as the product of two power-law models. This proposed model has been proved to be capable of capturing both strain hardening and thermal softening behaviors of material, even for perfect plasticity with large strain conditions.

To account for the directionality of the material properties in sheet metal, Yld2000-2d, which has been proved to be one of the most accurate and efficient yield functions for aluminum alloys in numerical analysis, is selected as the anisotropic yield function in this work. Eight parameters in Yld2000-2d have been determined and calibrated using the experimental results from uniaxial and biaxial testing of AA5182-O. Moreover, those eight

parameters are fitted in to the temperature-dependent functions, hence the evolution of yield surface is predictable in response to the temperature changes. It is noticed that the material carries more anisotropy at ambient temperatures and tends to approach the isotropic behavior when the temperature elevated to 300℃.

The strain-based and stress-based forming limit diagrams (FLD) of AA5182-O at various temperatures have been constructed by calculating the theoretical M-K model with Newton method and backtracking algorithm. The obtained FLDs are found to be instructive and will be applied in the post-processing of FE simulation for stamping so as to identify the critical area of failure.

The developed constitutive model and modified yield function are implemented in the form of user defined subroutine (VUMAT) in ABAQUS/Explicit. An explicit stress integration algorithm has been selected for the stress integration with rate-depend viscoplasticity model at temperature higher than 150℃. In the low temperature range, the Newton method and cutting plane algorithm are utilized to update the stress tensor with a classic elastoplastic constitutive model. To validate the VUMAT, a non-isothermal tensile testing has been performed with aids of infrared thermal camera and DIC. The heat transfer coefficients in FE model are calibrated with captured thermal images. With appropriate selection of mesh size and mass scaling factor, the punch load vs. displacement curve obtained from the simulation perfectly correlates the experimental result.

DEDICATION

This thesis is dedicated to

Mengqi Zhao

my beloved wife

who is always beside me with her patience, unconditional love,

and endless support.

Xiaoke (Ariana) Zhang

my daughter

Thanks for your presence at this moment of my life. Your smile

encourages me to accomplish this work.

ACKNOWLEDGMENTS

I am feeling grateful and would like to express my deepest appreciation to Dr. Fadi Abu-Farha who is the greatest mentor in my entire life and has been providing continuous support during my PhD study.

I would like to thank my committee members: Dr. Srikanth Pilla, Dr. Robert Prucka, and Dr. Gang Li. You all helped me a lot in the most suffering part of my research with professional knowledge and patients.

Thanks Songhao Li, Xiaoqing Cao, Peng Zhang, Wei Zuo, Xueyi Wang, Xunan Hao, and Liang Yu. You all are my best friends for my life.

To all who have supported and guided me on my career path to PhD over the years at Iowa State University and Clemson University, you have my sincere appreciation. I can never accomplish this work without your support.

Finally, I am grateful to have the National Science Foundation (NSF) supporting this work under grant # CMMI-1254670.

TABLE OF CONTENTS

Table of Contents (Continued) Page

LIST OF FIGURES

Page

List of Figures (Continued) Page

List of Figures (Continued) Page

List of Figures (Continued) Page

Table of Figures (Continued) Page

LIST OF TABLES

Page

CHAPTER 1: INTRODUCTION

1.1 Aluminum Alloy Sheets in Automotive Sector

During the past few decades, the more and more strict regulations on exhaust emission control are increasing the demand of fuel-economy vehicles in market. As a consequence, the automotive industry pays enormous efforts to reduce the vehicle curb weight in order to improve the fuel efficiency. The most effective approach for weight reduction is to replace the conventional steel with lightweight non-ferrous materials, such as aluminum-magnesium alloys and carbon fiber. Over the past 50 years, various of materials started to be applied to vehicles and passenger car body structure has experienced a transition from all-mild-steel to mixed materials [1]. In this intensive material competition in automotive sector, aluminum alloys become the most promising candidates due to the good strength-to-weight ratio. So far, a lot of parts in a modern vehicle are being produced by aluminum castings, such as engine block and wheels. Meanwhile, wrought aluminum alloys are also attracting increasing interests today, especially for the use of exterior panels. Several OEMs have already launched their “all-aluminum” car models. As the first high-volume vehicle built with all-aluminum body, the 2015 Ford F-150 pickup is probably the most impressive one which weighs 700lbs lighter than last generation due to the extensive use of aluminum in structure.

However, a larger scale applications of aluminum alloy sheets in automotive industry are still limited. This could ascribe to two main reasons from the perspective view of manufacture: (1) the raw material cost of aluminum alloys is approximately two to three

times higher than that of steel and (2) the formability of aluminum alloy sheets is significant lower than that of steel in ambient temperatures and hence does not permit forming too complex parts. In addition, serrated yielding and the Portevin-Le Chartelier (PLC) effect, commonly observed between room temperature and 100℃ in many grades of aluminum alloy sheets [2-4], adversely affect the surface quality of the material and thus exclude it from application in outer body panels. To address the formability issue, elevating the forming temperature is conventionally applied to enhance the flowability of material.

1.2 A Critical Review of Warm/Hot Forming of Aluminum Alloy Sheets

Typically, forming the sheet metals at elevated temperatures is referred as warm/hot forming. In general, warm/hot forming is intended to improve material formability by reducing the activation energy and activating particular deformation mechanisms. For aluminum-magnesium alloys, superplastic forming (SPF) and quick plastic forming (QPF) are the very typical hot forming methods which require the forming temperatures above recrystallization temperature. Flow behavior, formability and deformation mechanisms have been investigated for several AA5xxx sheets at a wide range of SPF/QPS conditions [5-8]. The extreme tensile ductility (>200%) in both methods enable forming complex parts that could not be formed by conventional techniques (cold forming).

SPF uses gas pressure to slowly deform the sheet into the die and has been widely used for spacecraft and airplanes manufacture. However, considering the low strain rate (<0.001) required by process, the annual volume of SPF is extremely low and the process cost is significantly high which is unfit for automotive industry. In addition, the material

in SPF needs to carry fine grain microstructure in order to fully expand the forming limit. This will even boost the total cost for this process. Similar to SPF, QPF process also uses hot gas to form the aluminum alloys into the die. However, the working temperature for QPF is generally in a lower temperature range, from 400℃ to 510℃, for aluminum alloy sheet metals. The major contribution by QPF is reducing the cycle time of SPF by applying greater pressure (250~500 psi) [9]. QPF has also gained significant interest, and even automotive use, with several 5xxx alloys [10]. However, the process cost for QPF has not been scaled down to be acceptable for mass production. Generally speaking, although hot forming of aluminum alloy sheets can significantly improve the material formability, the high material cost (fine-grained material), high labor cost (long cycle time), low production volume and tremendous energy cost (working temperature), have put a major constraint on their use on a large scale in automotive industry.

Warm forming process requires a much lower temperature range (~150 to ~300℃). Apparently, the formability in warm forming process is not as good as that in hot forming. Many commercial grades aluminum alloy sheets, such as AA5xxx sheets, still exhibit decent improvement in formability compared to that at ambient temperatures. Evidence to this can be seen in AA5182-O; one of the most popular automotive grade Al-Mg sheet materials [11-13]. At the same time, PLC effect can be eliminated in this temperature range. In spite of this, warm sheet forming operations have not gained an appreciable level of application in the automotive sector. Some works investigated the material behavior during warm hydroforming where the sheets are deformed by warm fluid/gas [14-16]. The fact that the setup is heated in warm forming implies considerable amounts of energy (even

though the temperatures are lower than SPF/QPF) and limitation to the forming speeds. On the other hand, this technique is not suitable to produce panels which is mainly completed by conventional stamping.

Overall, raising the forming temperature is so far the most effective method to increase material forming limit for aluminum alloy sheets, but the considerable energy cost is also inevitable, especially for hot forming techniques, which is challenging to fit an automotive environment. Minimizing the energy consumed while still maintaining a decent formability is the possible breakthrough to spread the application of aluminum alloy sheets in automotive industry.

1.3 Hot Blank – Cold Die (HB-CD)

An alternative process, referred to as hot blank – cold die (HB-CD) stamping, is proposed as a compromise between cold and warm/hot forming processes, to advance the use of lightweight sheet materials. A schematic of the process is shown in Figure 1-1. In it, the blank is heated to a selected temperature and then transferred to a cold die/press to be stamped into a particular geometry. In general, heating the blank provides the boost in formability needed to form the part; heating only the blank and keeping the temperature of tool sets as low as possible imply much lower energy consumed compared to any form of warm/hot forming. Additionally, stamping in cold dies means a fit to the current stamping infrastructure, and the ability to achieve similar production volumes. Literally, HB-CD stamping is simply equivalent to “hot stamping of boron steels”; the approach is similar, yet the temperatures are much lower, there is no need for additional quenching

component/process. Hot stamping of boron steels is a widely used process; almost every car produced today has a hot-stamped component. HB-CD has thus great potentials for forming hard-to-deform non-ferrous materials (aluminum and magnesium) into cost-effective high-volume automotive components.

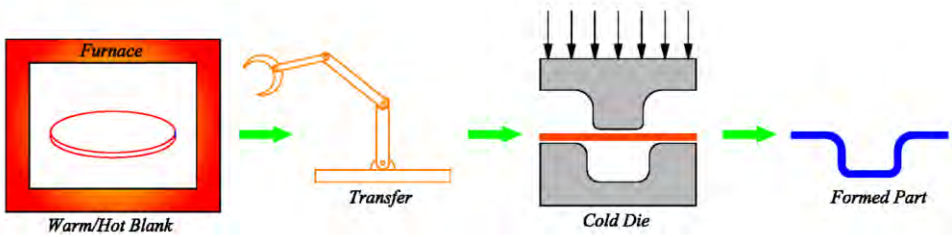

Figure 1-1: Schematic of the Hot Blank – Cold Die (HB-CD) stamping process

1.4 Research Objects and Layout

Though the process is simple, the non-isothermal nature of material deformation during HB-CD could be very complex. Considering the uniqueness of HB-CD process, the temperature gradient over the blank will critically determine the material flow. In literature, numerous studies were dedicated to traditional sheet metal forming process with aluminum alloy sheets, such as forging and deep drawing, presumed the isothermal environment [17-20]. Non-isothermal condition is commonly come across in the deep drawing investigation [21-26]. It has been widely proved that creating appropriate temperature distribution over blank will contribute to better formability. Unlike the extensive investigations on non-isothermal deep drawing, there are no a lot of works focus on hot stamping with automotive aluminum alloy sheets published until recent five years. Bariani et al. experimentally proved the feasibility of hot stamping with AA5083 in industrial trials [27]. The group

from Ford Motor Co. led by Harrison and Luckey demonstrated the possibility of hot stamping a B-pillar outer panel with AA7075 [28]. Only a slight drop in ultimate strength and hardness as compared to the as-received material was noticed in the formed part. Choi et al. developed a two-step forming process to stamp A-pillar cover out of AA6xxx sheets [29]. Although several works have completed the hot stamping with aluminum alloy sheets, the material characterization and model development are still not adequately addressed from the perspective view of research in the literature. In fact, no investigation has been published on a comprehensive study of hot stamping with aluminum alloy sheets, including advanced material properties characterization, material model development, and finite element simulations.

Therefore, this research aims at developing a systematic approach, from material characterization to finite element simulations, to investigate the deformation of aluminum alloy sheets during the non-isothermal forming processes.

The following dissertation is arranged and split into four parts:

(i) Examine the material behavior with tensile testing over a wide range of conditions, mainly temperatures spanning between the initial temperature of the blank (~300℃) and room temperature. Extract the true stress-strain curves of material in response to various temperatures and strain rates. Identify the deformation mechanisms in different temperature ranges. Inspect the material anisotropy by evaluating r-value and analyzing bulge test.

(ii) Develop a constitutive model that can capture the material flow behavior at different experimental conditions. Fix the coefficients for anisotropic yield function at different temperatures. Construct the material forming limit diagram, from room temperature to 300℃, using Marciniak-Kuczynski (M-K) model.

(iii) Compare the explicit and implicit stress integration algorithms. Implement the developed constitutive model into ABAQUS/Explicit in the form of user subroutine (VUMAT). Perform the simulation with single element and normal tension tests to verify the VUMAT and determine the critical time step size.

(iv) Design and complete the non-isothermal uniaxial tensile testing which is a new testing approach to study the material deformation during the hot stamping. Perform the finite element simulations and validate using experimental results.

Although being addressed separately in four chapters, those four parts are actually coherent and mutually supportive in order to deliver the final package.

CHAPTER 2: ADVANCED MATERIAL PROPERTIES CHARACTERIZATION

As the fundamental of sheet metal forming study, it is crucial to understand the material behavior. One of the contributions of this study is to characterize material behavior, at elevated temperatures, with digital image correlation to closely examine the material deformation. Besides, the inherent anisotropy in as-received material is characterized by evaluating the r-value and bulge test.

2.1 Microstructure Examinations of AA5182-O

The material selected for this study is AA5182-O which is one of the most popular aluminum alloy sheets in the automotive sector. A 2.0mm thick 5182 aluminum alloy sheet, received in the annealed condition, was used. The material's chemical composition is provided in Table 1. The initial microstructure of the as-received material was examined using a Zeiss AxioVert A1 inverted microscope. Specimens were polished and then electrochemically etched using Baker's Etch. An example of the grain structure in the RD-ND plane, revealed under polarization at 200x, is shown in Figure 2-1. The average grain size was measured to be 18.38±5μm by averaging the results from over 30 measurements (vertical, horizontal and diagonal lines) in different regions. Figure 2-2 presents the pole figure of the as-received material.

Table 1: Chemical composition (wt%) of the AA5182-O sheet used in this work.

Element	Al	Mg	Mn	Fe	Si

wt%	Balance	4.53	0.24	0.07	0.05

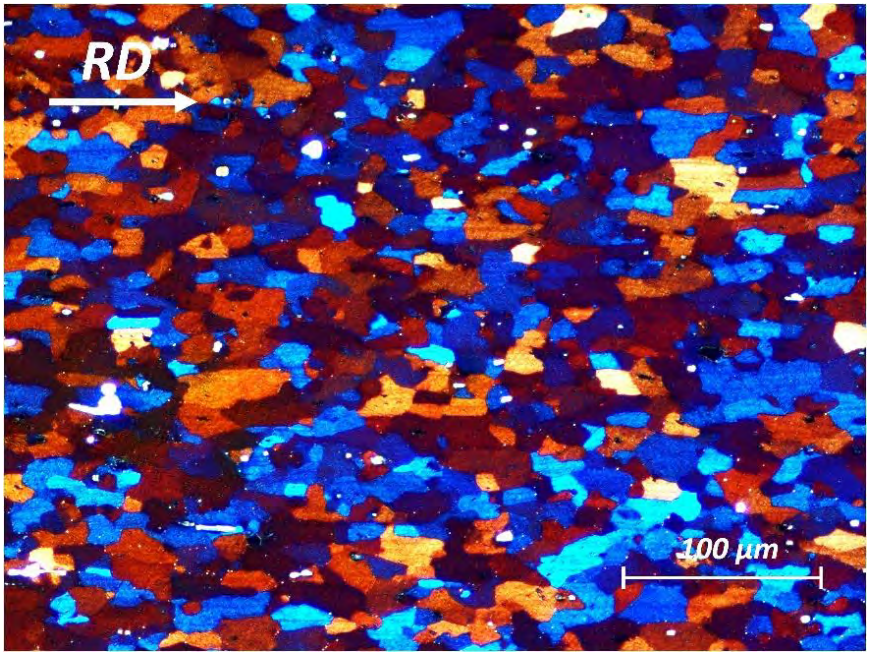

Figure 2-1: Polarized optical micrograph showing the microstructure of the as-received material.

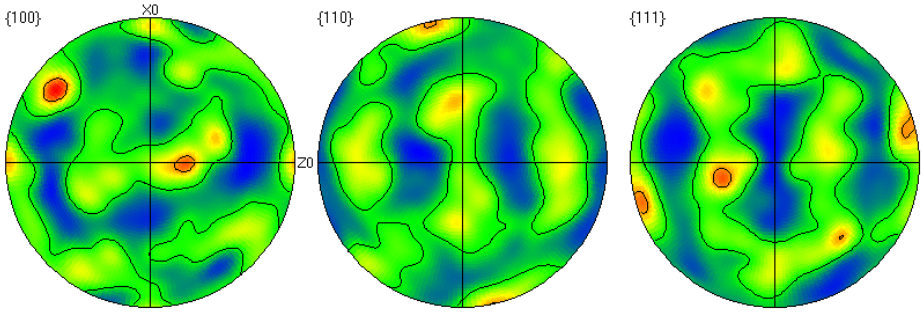

Figure 2-2: Pole figures of as-received AA5182-O.

2.2 Using Digital Image Correlation (DIC) at Elevated Temperatures

Digital Image Correlation (DIC) is a state-of-the-art optical and material independent measuring system which is designed for providing accurate: surface coordinates, displacement and velocities, surface strain values, and strain rates. The images from one or more camera track the deformation of the material during testing; changes in the grey value pattern of an array of small groups of pixels (called subsets or facets) are tracked and correlated to a reference image (global or incremental) to obtain the displacements and strains across the surface of the deformed material [30]. In 1980s, two-dimensional (2D) DIC technique using single camera was first developed to measure the in-plane displacement and strain [31, 32]. A schematic showing the typical set-up for 2D camera is presented in Figure 2-3a. After that, 2D DIC was widely used in the plane strain experiments. However, it has been noticed that small out-of-plane displacement in 2D measurement can affect the accuracy especially for the measurements on a small area. In 1993, Luo et al. improved the DIC technique by capturing the object using two cameras from different angles as it is seen in Figure 2-3b [33]. With appropriate calibration, the images independently obtained from two cameras can be correlated and thus construct the 3D coordinates. That being said, all the movement within the measuring space can be precisely detected; the negative effects of small out-of-plane motion on 2D measurement can be eliminated as well. Error analysis of 3D DIC measurement has been conducted in multiple works. Tung et al. used a simplified 3D DIC to measure a plate specimen with in-plane and our-of-plane deformation which shows strain measured with 3D DIC is feasible

and accurate [34]. Hu et al. theoretically evaluated the system error influenced by calibration and correlation [35].

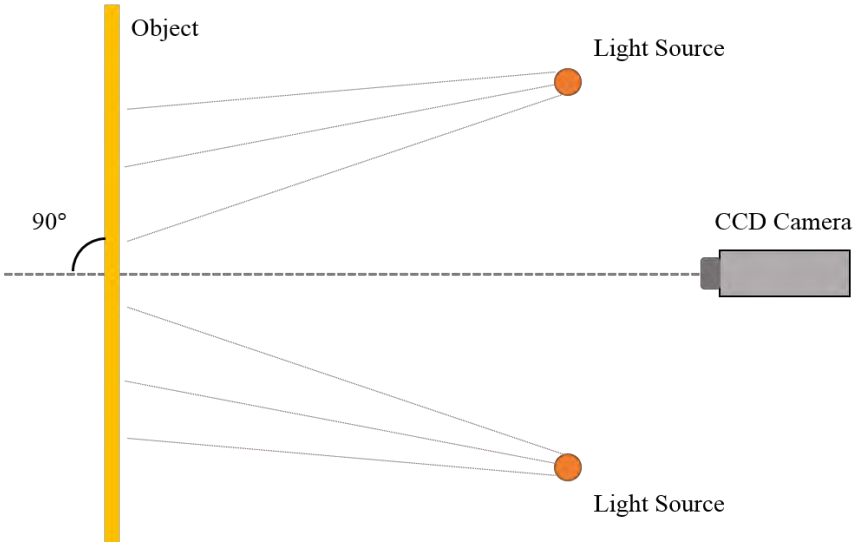

(a)

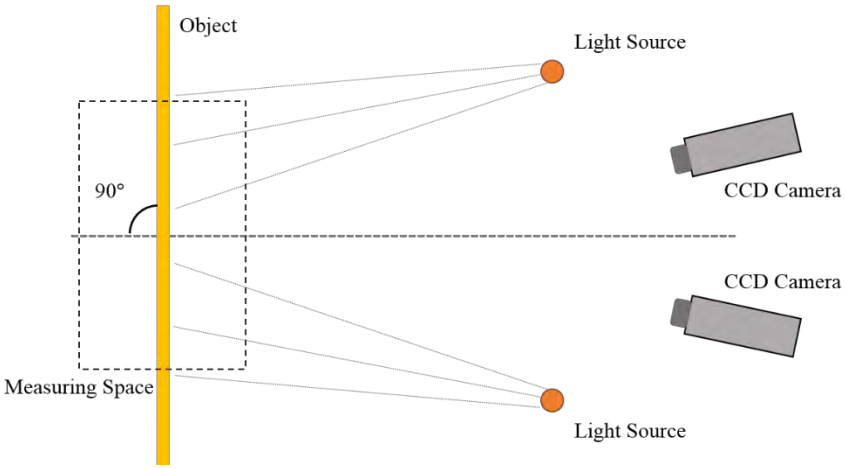

(b)

Figure 2-3: Schematic of the (a) 2D and (b) 3D DIC systems.

Due to its excellent versatility and accuracy, over the past two decades, DIC system has found numerous applications in deformation measurement [36-41] However, the application of DIC in above-the-ambient temperature conditions are still limited [42-46]. Actually the strain measurements are critically important for obtaining accurate stress-strain curves, especially for higher-than-ambient temperature testing. Conventionally, the vast majority of efforts in the literature rely on the displacement of the tensile tester for strain measurements, despite the significant compliance issues that escalate as the testing temperature increases. Extensometer resolves such issues, yet it is limited to nominal strains between two points, and thus does not enable detailed investigation of strain accumulation and localization in the material. Moreover, the use of traditional extensometer presents a set of complications to the execution of highly repetitive experiments at high temperatures.

In this study, one of the tasks is to deeply explore the capacity of using DIC system in mechanical testing, including tensile and bulge tests, for material properties determination over a wide ranges of experimental conditions. All the experiments involved in this work are being performed with assists of a 3D DIC system (GOM ARAMIS 5M). The details of experimental set-up and results extraction will be discussed in each section, respectively.

2.3 Isothermal Uniaxial Tensile Tests at Elevated Temperatures

Uniaxial tensile testing is probably the most fundamental but imperative testing method to characterize the mechanical behavior of material. The testing is commonly

performed on uniaxial load frame, and the procedures, including the specimen geometry, are standardized by ASTM E8 or EN ISO 6892-1/2. The results seeking in tensile testing include stress-strain curves, yield stresses, and anisotropy parameters (r-value). Besides, DIC enables the examination of deformation mechanism, such as PLC band, with evolving full-field strain and strain-rate maps with time.

2.3.1 Experimental set-up

An INSTRON 5985 uniaxial tensile testing machine fitted with a convection environmental chamber, was used here, as shown in Figure 2-4a. The tensile tester has a 250kN load capacity; but a 10kN load cell was used in the experiments to improve the accuracy of load measurements. The environmental chamber can reach steady state testing temperatures as high as 500 ºC, within at the maximum temperature. Since a wide range of temperatures is covered in this work, consistency of heating and testing approach is very critical; therefore, quick-mount grips, following a previous effort on uniaxial tensile testing at extreme temperatures including superplastic materials, was adopted here [47]. The grips enable fast loading of test specimens into a pre-heated setup, thus minimizing temperature drop during the process, and ensuring consistent heating time of test specimen (within 5 minutes). The grips pull on the shoulder of the specimen to eliminate the possibility of slip, without any pressure on the grip area to minimize material flow, especially at higher temperatures. The as-received AA5182-O sheets were waterjet-cut into specimens according to the particular geometry shown in Figure 2-4b. The gauge region is 8mm wide and 30mm shoulder-shoulder long, with a 3mm-radius fillets at the ends. All specimens were prepared along the rolling direction of the as-received sheet. The DIC

configuration with respect to the tensile testing setup is shown in detail in Figure 2-4a. As noted, the DIC cameras were rotated in a vertical orientation to enable viewing the test specimen through the rectangular window (150mm×225mm) in the environmental chamber. The cameras/lenses were set to a calibration volume of ~100mm, thus the pixel resolution of captured images was ~40μm/pixel. Calibration of the DIC setup was performed before testing with the chamber door open (so calibration was not done through the glass).

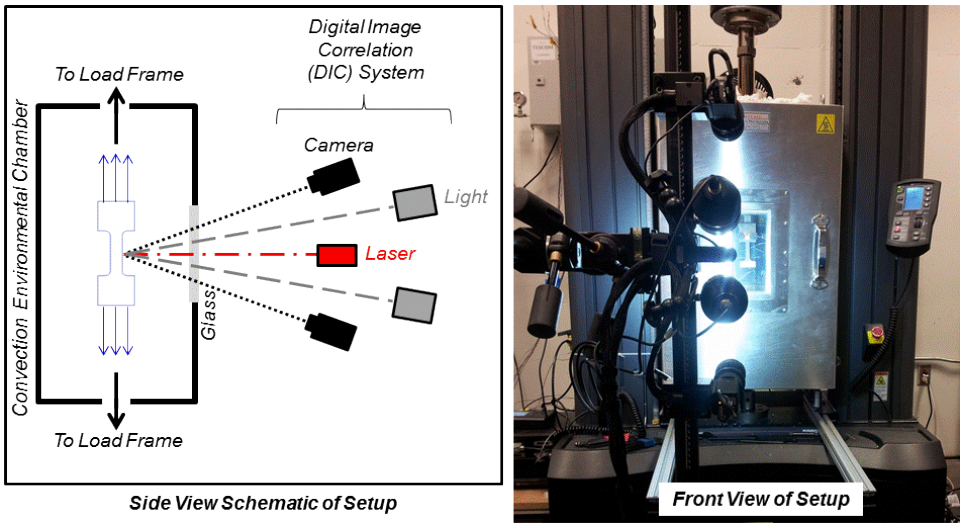

(a)

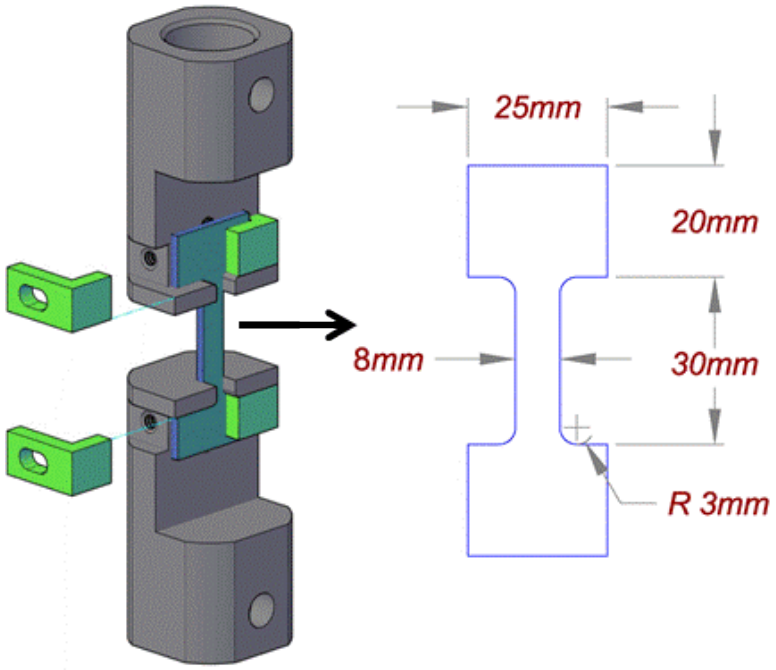

(b)

Figure 2-4: (a) Front view and schematic side view of the experimental setup used for isothermal tensile testing at different temperatures, featuring a universal tensile tester, a convection environmental chamber and a DIC system. (b) Test specimen geometry and fit within the quick-mount grips.

2.3.2 Stress-strain curves

All the stress-strain curves presented in this paper were extracted from the DIC analysis results. The true stress-strain curves for the lower temperatures, 25 and 100℃ are shown in Figure 2-5a and b. Serration yielding is clearly observed in both cases. The critical strain for serration yielding is not of a prime focus in this work; nonetheless, it is noted that the onset of serration yielding is postponed by increasing the temperature. The stress-strain curves for both temperatures are almost identical, showing no effect of temperature on the

overall hardening behavior. Also, though not significant, higher strain rates produce relatively lower flow stresses, implying negative strain rate sensitivity (SRS). This unique stress-strain behavior, including serration yielding, is associated with dynamic strain aging (DSA) in the material [48, 49], and has been explained as a macroscopic result of interactions between solute substitutional atoms (such as magnesium in this case) and dislocations [4, 50].

With the increase in temperature, PLC effect and serration yielding completely disappear at and above 150 ºC (Figure 2-5c), while SRS gradually moves out of the negative region. At 200℃, the true stress-strain curves are shown in Figure 2-5d; lower strain rates globally lead to lower flow stress levels, which means the corresponding SRS has turned positive [48, 49]. The response of total elongation to drop in strain rate is apparent, with material tensile ductility exceeding 60%. Strain hardening is still evident in all the stress-strain curves at this temperature. However, the softening effect becomes stronger with further temperature increase, as demonstrated by the stress-strain curves at 300 ºC, shown in Figure 2-5f. Near perfectly-plastic behavior is noted at low strain rates; hardening is only observed at the initial stages of deformation at higher strain rates.

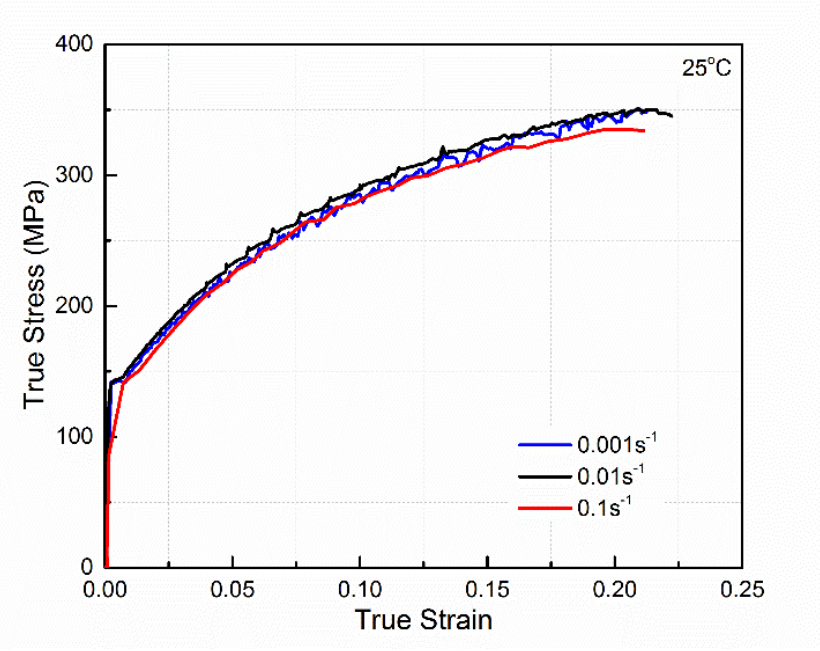
25°C
True Stress (MPa)
True Strain
0.001s-1
0.01s-1
0.1s-1
0
100
200
300
400
0.00
0.05
0.10
0.15
0.20
0.25

(a)

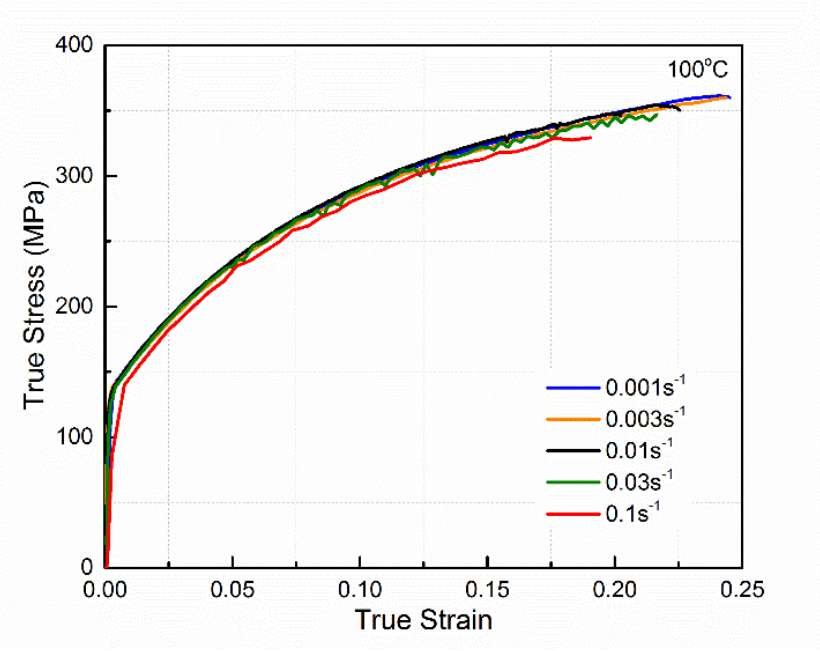
100°C
True Stress (MPa)
True Strain
0.001s-1
0.003s-1
0.01s-1
0.03s-1
0.1s-1
0
100
200
300
400
0.00
0.05
0.10
0.15
0.20
0.25

(b)

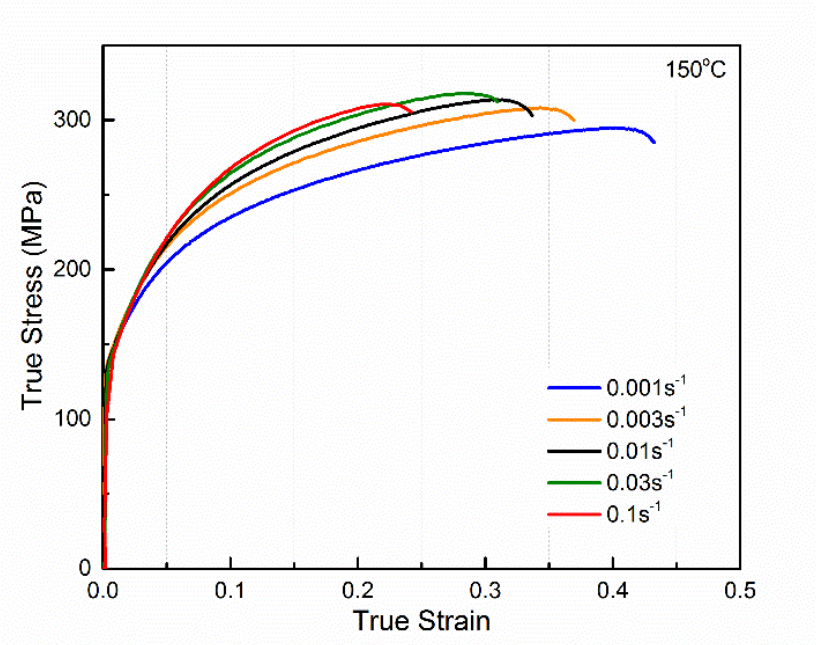
150°C
True Stress (MPa)
True Strain
0.001s-1
0.003s-1
0.01s-1
0.03s-1
0.1s-1

(c)

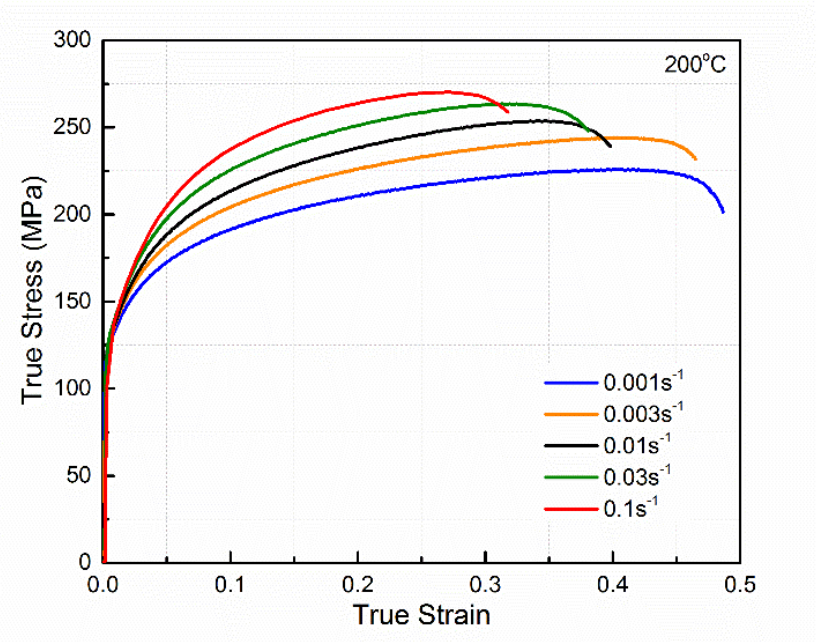
200°C
True Stress (MPa)
True Strain
0.001s-1
0.003s-1
0.01s-1
0.03s-1
0.1s-1

(d)

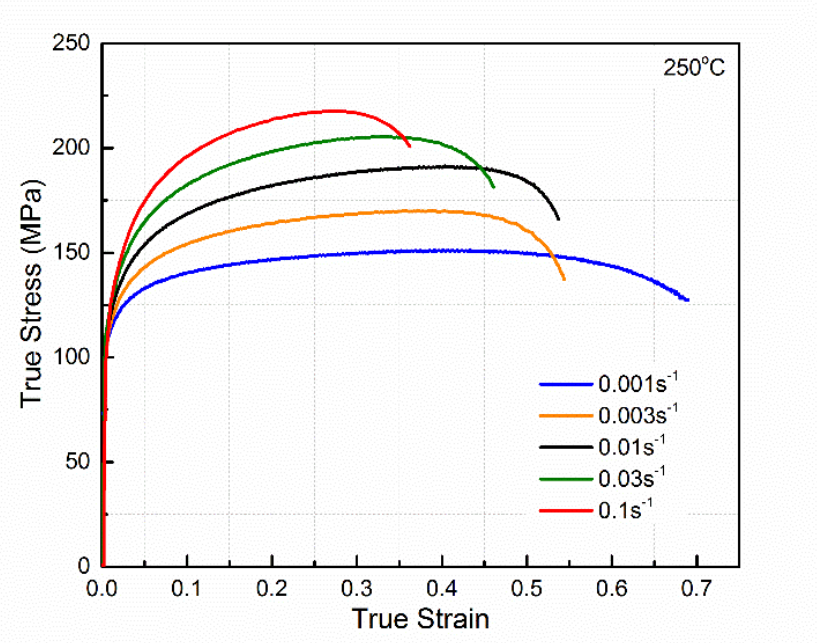
250°C
True Stress (MPa)
True Strain
0.001s-1
0.003s-1
0.01s-1
0.03s-1
0.1s-1

(e)

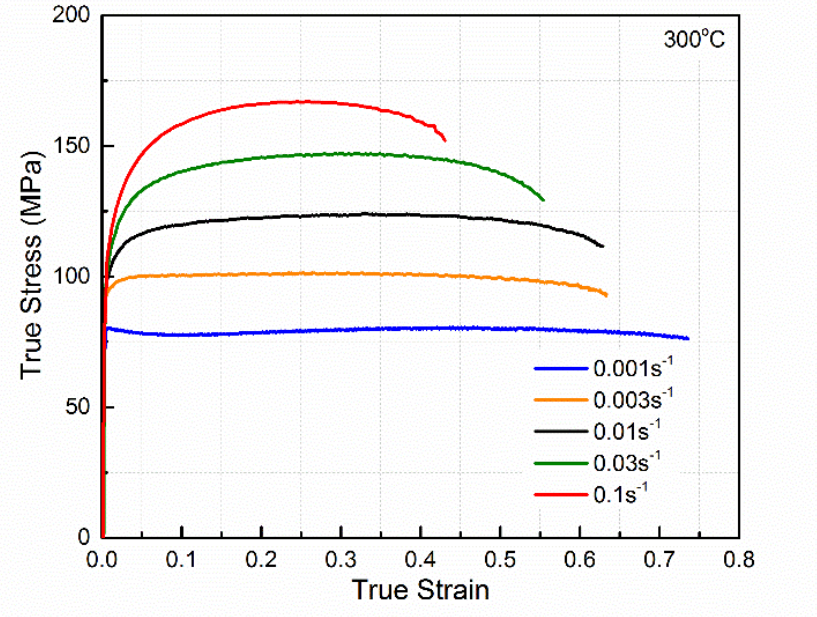
300°C
True Stress (MPa)
True Strain
0.001s-1
0.003s-1
0.01s-1
0.03s-1
0.1s-1

(f)

Figure 2-5: True stress-strain curves for AA5182-O at different strain rates, for a selected temperature of (a) 25℃, (b) 100℃, (c) 150℃, (d) 200℃, (e) 250℃ and (f) 300℃.

2.4 Anisotropy

Most cold rolled sheets exhibit anisotropic characteristics. Anisotropy in aluminum alloy sheets at room temperature is commonly agreed and has been extensively studied. Hill extended von Mises criterion to an anisotropic function which describes the yielding of orthotropic materials [51]. Banabic proposed a yield criterion (BBC2003) for orthotropic sheet metal under place stress conditions and evaluate the anisotropic behavior of AA5182-O with cruciform specimen under biaxial loading condition [52]. Barlat has done exhaustive work on yield function for aluminum alloys [53-57]. The series of Yld yield function, such as Yld96 and Yld2000-2d, succeed in describing anisotropic behavior for aluminum alloys [12, 58]. More literature review will be presented in part II. Considering temperature plays the most significant role in material behavior of aluminum alloy sheets at elevated temperatures. It is indispensable to investigate material anisotropy at high temperatures. However, very few of studies take this issue into consideration. In most cases, either the material is presumed to reduce to isotropic or the yield surface at high temperature is consistent with that at room temperature [59]. Naka et al. determined the yield locus for AA5083 at elevated temperatures and concluded the yield locus shifts as function of temperature [60]. According to the work of Abedrabbo et al. [12], it is obviously seen AA5182-O shows anisotropic characters as long as temperature climbs to 260℃. Thus,

to accurately predict material behavior in non-isothermal forming, anisotropy at elevated temperature is a crucial topic and has to be taken into account for FE simulation.

The purpose of this section is to experimentally evaluate anisotropic behavior of AA5182 at different temperatures by comparing yield stress and anisotropic parameter (r-value). On the other hand, the obtained yield stress and r-value will be used as input to determine the coefficients for Yld2000-2d in the part II. Specimens cut along 45 and 90 degree to the rolling direction are also tested in the same temperature range with the ones in 0 degree at strain rate of 0.01 s^{-1} . True stress-strain curves of specimens in 0, 45 and 90 degree at different temperatures are shown in Figure 2-6. It clearly shows that the flow stress level of 0 degree is slightly higher than the others' below 300℃ while 45 and 90 degree exhibits very similar flow behavior. At 300℃ in Figure 2-6d, flow stress at 90 degree becomes higher than that of 0 and 45 degree.

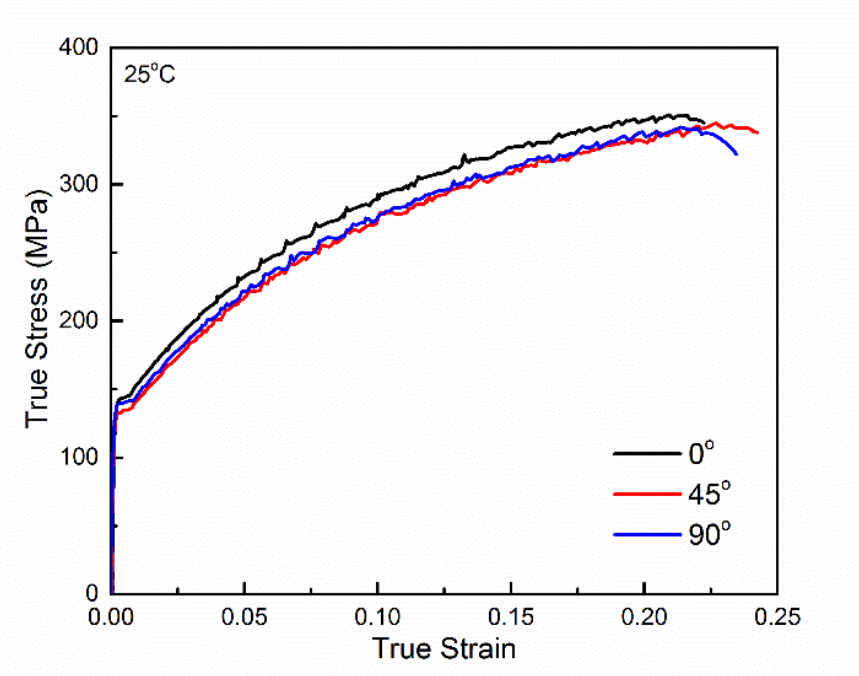
25°C
True Stress (MPa)
True Strain
0°
45°
90°
0
100
200
300
400
0.00
0.05
0.10
0.15
0.20
0.25

(a)

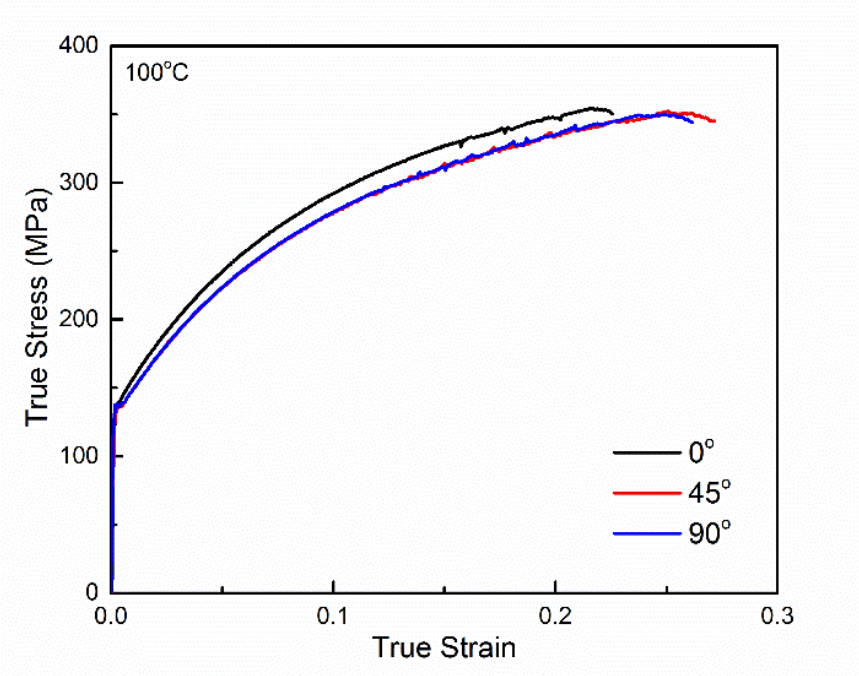
100°C
True Stress (MPa)
True Strain
0°
45°
90°
0
100
200
300
400
0.0
0.1
0.2
0.3

(b)

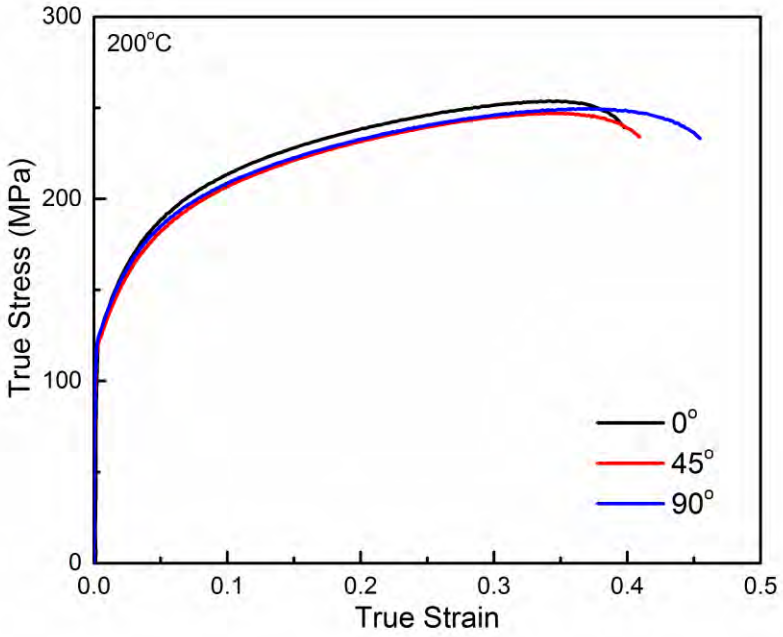
200°C
True Stress (MPa)
True Strain
0°
45°
90°
0
100
200
300
0.0
0.1
0.2
0.3
0.4
0.5

(c)

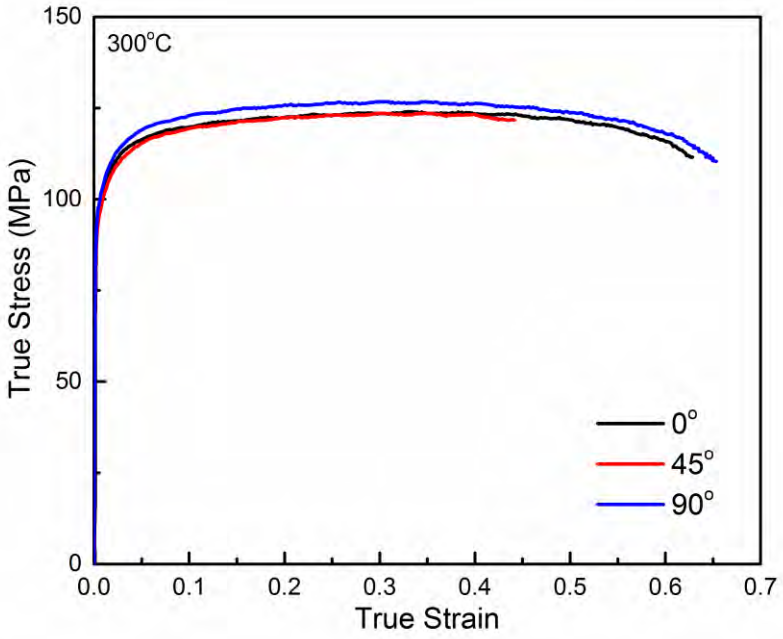
300°C
True Stress (MPa)
True Strain
0°
45°
90°
0
50
100
150
0.0
0.1
0.2
0.3
0.4
0.5
0.6
0.7

Figure 2-6: True stress-strain curves of 0, 45 and 90 degrees to the rolling direction tested at temperature of (a) 25℃, (b) 100℃, (c) 200℃ and (d) 300℃. The strain rate is $0.01s^{-1}$

For aluminum alloys, yielding in tensile testing is rarely a discrete point on stress-strain curves. It is thus difficult to precisely measure the yield stress for aluminum alloys, especially at high temperature, by traditional 0.2% offset method. For current study, the flow stresses at plastic work of 30MPa per volume are extracted as yield stresses. This approach has been used in a pioneer research work by Abedrabbo [12]. In Figure 2-7a, extracted yield stress for different temperature conditions are plotted. Globally, the yield stresses do not decrease in terms of dynamic strain aging until the temperature is heated above 100℃. Above 100℃, yield stresses drop dramatically with increasing temperature. In lower temperature range (<200℃), yield stresses at 0 degree are slightly higher than those of 45 and 90 degree. However, this difference diminished at higher temperature. At 250℃ and 300℃, the yield stresses at 0, 45 and 90 degree are almost identical. Figure 2-7 (b) illustrates the plot of normalized yield stresses σ_0/σ_0 , σ_{45}/σ_0 and σ_{90}/σ_0 at selected temperatures to clearly present the evolution of yield stresses in different directions with temperature increasing.

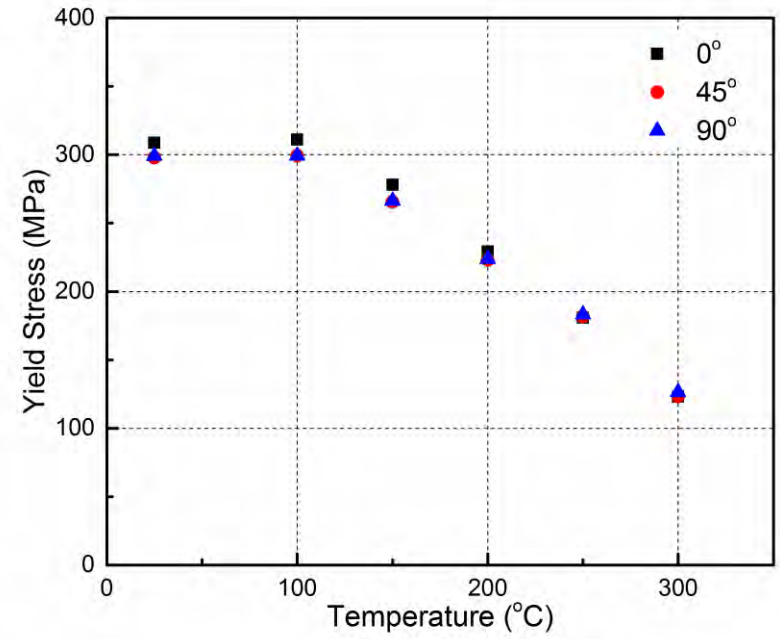
400
300
200
100
0
Yield Stress (MPa)
0
100
200
300
Temperature (°C)
0°
45°
90°

(a)

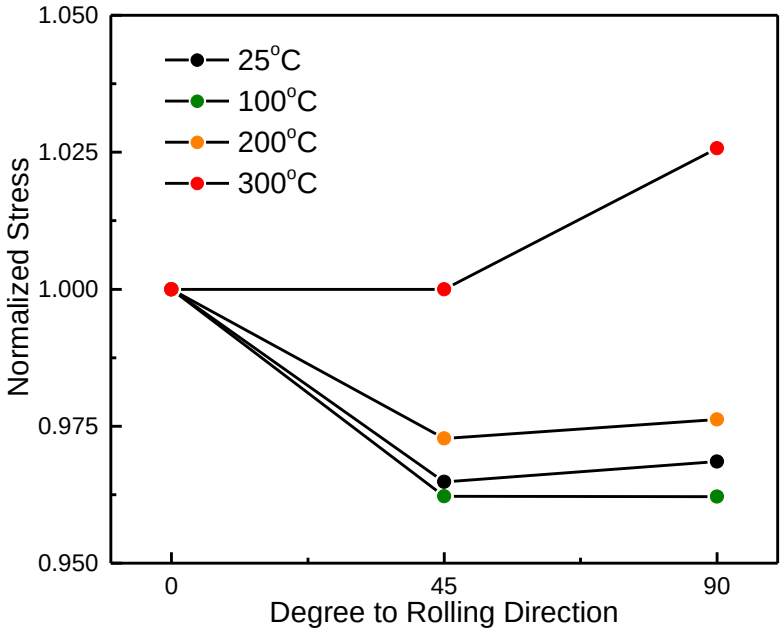
1.050
1.025
1.000
0.975
0.950
Normalized Stress
0
45
90
Degree to Rolling Direction
25°C
100°C
200°C
300°C

(b)

Figure 2-7: (a) Yield stress in different angles (σ_0 , σ_{45} and σ_{90}) at the equal plastic work (30MPa) of AA5182-O at different temperatures with strain rate of $0.01s^{-1}$. (b) Normalized yield stress with σ_0 as basis at temperatures of 25, 100, 200 and 300℃.

Based on the definition, anisotropy parameter (r-value) is calculated by ratio of width strain and thickness strain (ASTM E517).

$$r = \frac{\varepsilon_w}{\varepsilon_t} \tag{2.1}$$

Conventionally, determination of ε_w and ε_t requires utilization of axial and transvers extensometer plus the assumption of volume constancy. As it is discussed in previous section, using extensometer has its limits and is not competitive with DIC measurement in terms of accuracy. Like the evaluation of tensile strain in axial direction, ε_w and ε_t were directly extracted from DIC analysis results over entire selected gauge area. Then the r-value was calculated, as it is shown in Eq.(2.1), based on volume constancy assumption. Considering post-uniform contributes to the large deformation at high temperatures, it remains a doubt whether this approach to r-value is reasonable and valid at high temperature with heterogeneous deformation. Therefore, Figure 2-8 (a) and (b) present the complete plot of r_0 versus plastic strain and plastic work per volume over entire deformation process at temperature of 25℃, 200℃ and 300℃ and strain rate of $0.01\ s^{-1}$. In both cases, r_0 increases at the initial stage of deformation ($\varepsilon < 0.05$ or plastic work $<10MPa$) which might because of the invalidation of volume constancy assumption in

elastic regime. After that, although globally increasing, the fluctuation of r_0 lies within a considerable small range. To be consistent with the selection of yield stress, r-value is also chosen at the point where plastic work equals 30MPa per volume. As it is seen in Figure 2-8b, r-value selected at 30MPa is close to the steady-state value; thus this approach is rational and reasonable for both low and high temperatures.

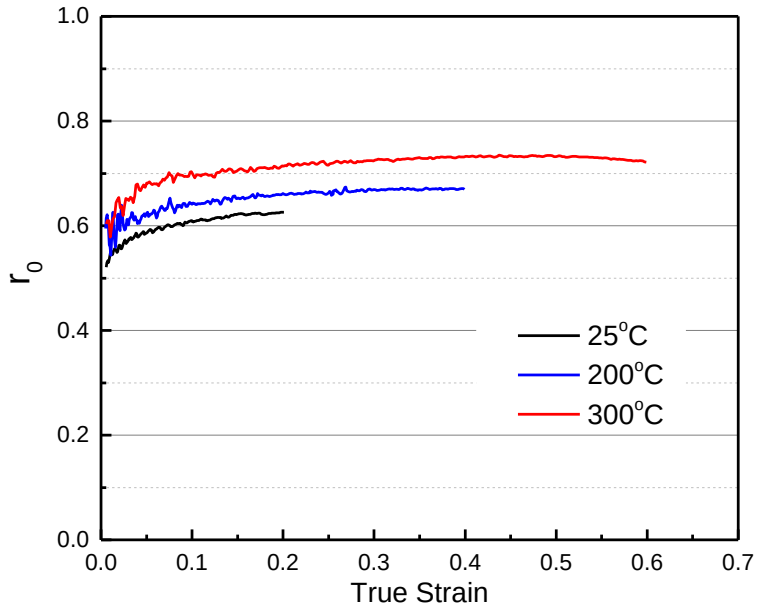
1.0
0.8
0.6
0.4
0.2
0.0
r_0
0.0
0.1
0.2
0.3
0.4
0.5
0.6
0.7
True Strain
25°C
200°C
300°C

(a)

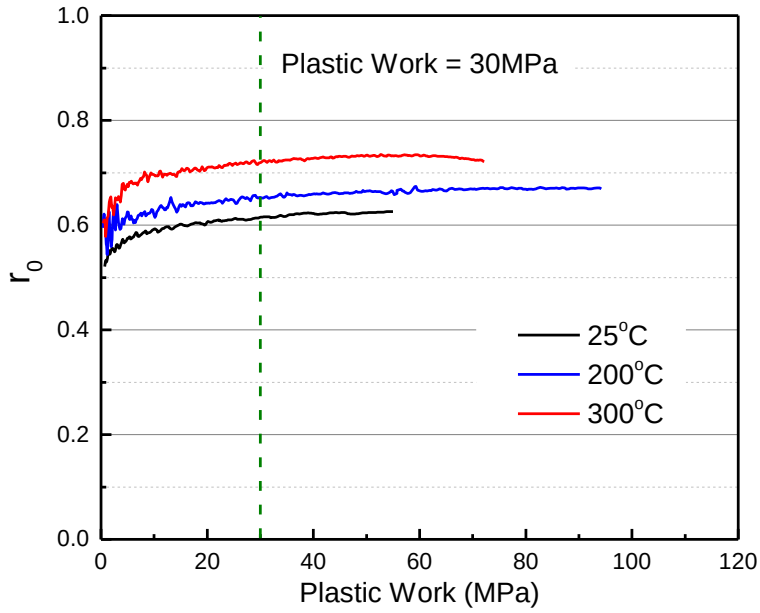
1.0
0.8
0.6
0.4
0.2
0.0
r_0
Plastic Work = 30MPa
0
20
40
60
80
100
120
Plastic Work (MPa)
25°C
200°C
300°C

(b)

Figure 2-8: Calculation of r_0 versus (a) true strain and (b) plastic work per volume using DIC measurement results at temperature of 25℃, 200℃ and 300℃, calculated at strain rate of $0.01s^{-1}$

Figure 2-9 shows the evolution in anisotropy parameters (r_0, r_{45} and r_{90}) at strain rate of $0.01\ s^{-1}$ over the experimental temperature range. Despite being difficult to fit in a simple function of temperature, it is still obvious that the global trend of r-value is growing with temperature increasing. This affirms that the material formability is enhanced at high temperature. However, r-value does not actually approach to 1 which indicates the assumption of isotropy at high temperature is invalid for AA5182-O. Therefore, a temperature-dependent yield function, which will be discussed in Section 0, is essential in order to accurately prescribe material behavior in multi-axial loading condition.

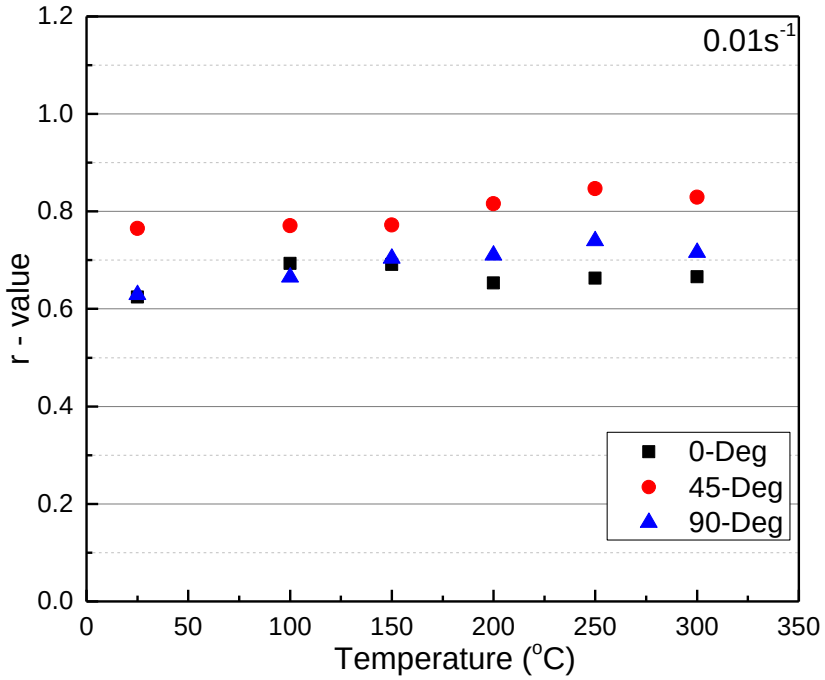

Figure 2-9: Anisotropy parameter (r-value) in 0, 45 and 90 degrees to the rolling direction at temperatures from 25℃ to 300℃, calculated at $0.01s^{-1}$ strain rate

2.5 Deformation Mechanisms

At elevated temperatures, the deformation of aluminum alloys generally involves creep flow and grain boundary sliding. To identify the deformation mechanisms in the different regimes of experimental conditions, the phenomenological governing equation developed by Sherby and Burke 1968 [61], and used later in multiple efforts, such as Taleff et al. [5, 62], is used here:

$$\dot{\varepsilon} = AD\left(\frac{\mathbf{b}}{d}\right)^{p}\left(\frac{\sigma}{E}\right)^{n} \tag{2.2}$$

where D is the appropriate diffusivity for the controlling creep mechanism, **b** is the magnitude of Burgers vector, d is grain size, p is the grain size exponent, n is the stress exponent which approximately equals the inverse of SRS, and σ is the flow stress. The Dynamic Young's modulus is dependent on temperature according to the expression [7]:

$$E = 77630 + 12.98T - 0.03084T^{2} \tag{2.3}$$

The stress exponent in Equation 1, indicated as n, has been utilized to indicate the distinguished deformation mechanism at various experimental conditions [5, 6, 62]. To

take the effects of the various temperatures into consideration, the normalization of strain rate chosen here is the in the form of the Zener-Hollomon parameter:

$$Z = \dot{\varepsilon} \exp(\frac{Q}{RT}) \tag{2.4}$$

where R is the gas constant ($R = 8.31\,\text{J/mol}\cdot\text{K}$) and T is the temperature in Kelvin. The activation energy Q was set to $142\,\text{kJ/mol}\cdot\text{K}$ since self-diffusion of magnesium and aluminum are similar [63]. Based on the above equations, a z-plot for the material is generated, as presented in Figure 2-10 below.

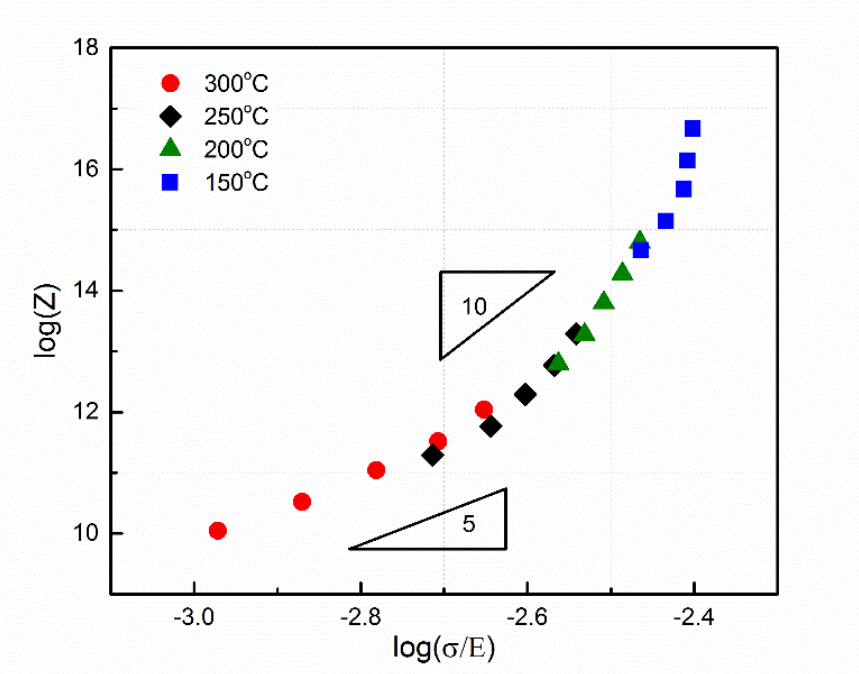

Figure 2-10: A Z-plot for AA5182-O at different temperatures with strain rate of 0.01s^{-1}.

In this plot, the n value is measured as the slope within a certain segment of the curve. In the lower temperatures region (<200°C), power-law breakdown is found to be the

dominant deformation mechanism, since ($n \gg 5$). Note the sharp increase in n at 150℃, even when compared to 200℃. The spike in n continues at lower temperatures (though not shown in the plot), with significant DSA at temperatures below 100℃ (as detailed earlier). On the other hand, as the forming temperature increases, the n value gradually decreases until it reaches approximately 5 at 300℃, which is a strong indicative of dislocation climb. The Z-plot clearly shows this shift in deformation mechanisms around ~250℃.

Utilization of DIC system allows to distinguish the primary deformation mechanism with both strain and strain rate maps at different temperatures. The phenomenon and mechanism of Portevin-Le Chartelier (PLC) effect was first reported by Le Chartelier in mild steel at elevated temperature [64] and has been very well-studied and documented in the literature for aluminum alloy sheets [65-69]. For the current investigation, PLC effect has been observed in the low temperature range where DSA plays the dominant role to control the material deformation. For instance, typical type-A PLC band was observed in the AA5182-O at room temperature and strain rate of $0.01\ s^{-1}$. Considering PLC band is periodically initiated and propagated within the gauge area, we focus here on one cycle of a band movement. The propagation of a PLC band in a test specimen deforming at 25℃ and $0.01\ s^{-1}$, is shown in Figure 2-11. From a strain rate perspective, part (a), the PLC band is initiated at one end of the gage region at ~40° relative to the tensile direction. The strain rate within the band width is much higher than the rest of the specimen. From the subsequent images after band initiation, it is seen that the band propagates to the other end of gage area at a constant speed; after that the band weakens and ultimately disappears until the next propagation. According to the strain field evolution,

shown in part (b) of the figure, the deformation before and after the band is considerably uniform. As soon as the band is formed, strain grows by a small amount in the field where PLC band sweeps over.

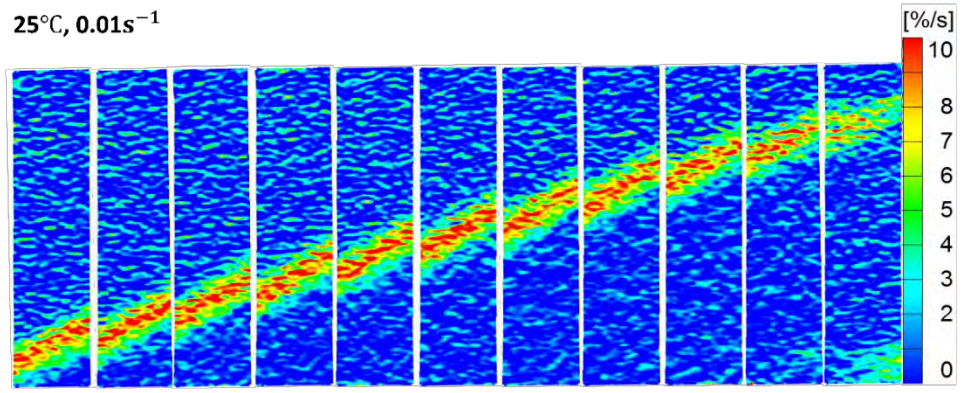

(a)

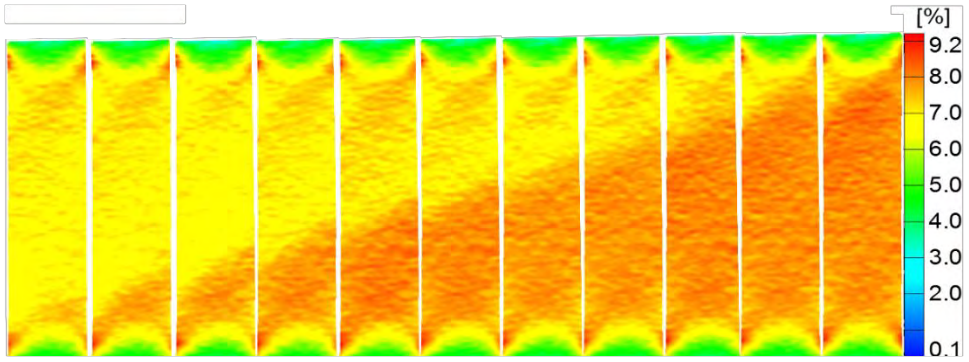

(b)

Figure 2-11: The (a) strain rate and (b) strain maps present one cycle of the movement of PLC band in AA5182-O deformed at room temperature with a strain rate of $0.01s^{-1}$.

Furthermore, the PLC band movement can be correlated to the serration in stress-strain curve. Figure 2-12 includes a segment of stress-strain curve that corresponds to the

propagation of PLC band. Flow stress climbs between two propagations of band movement where the mobile dislocation is locked by obstacles. As soon as band starts travelling, stress-curve is seen to be suppressed.

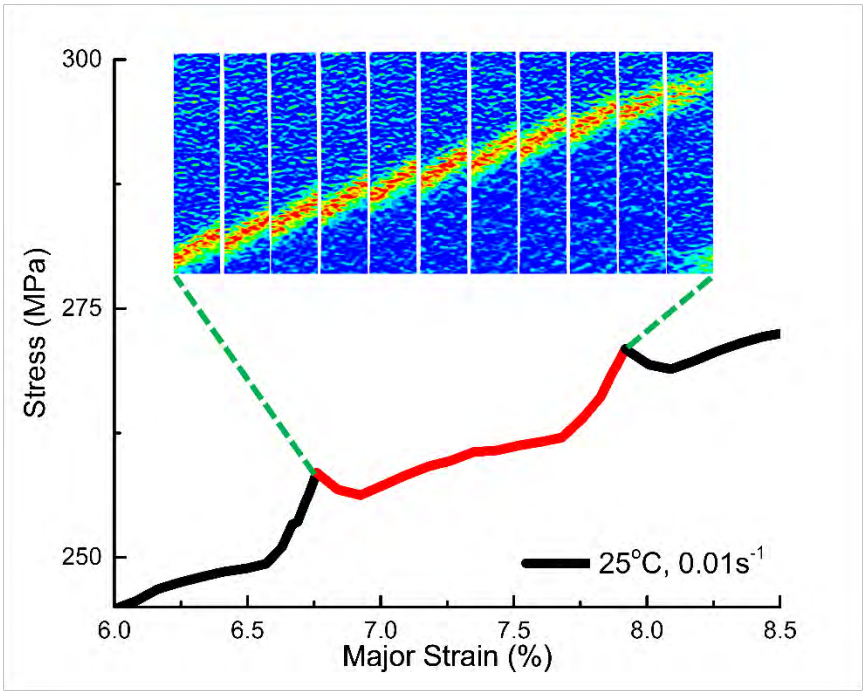

Figure 2-12: Propagation cycle of PLC band shown as strain rate and corresponding section of true stress-strain curves.

Aside PLC effect, the deformation processes at different temperatures are primary interests. Figure 2-13 reveals the deformation processes with incremental strain maps at different temperatures and 0.01 s^{-1} strain rate. Events occurring sequences during tensile deformation in both Figure 2-13a and b are very similar which indicates the same deformation mechanism controls material behavior at 25℃ and 100℃. PLC banding, if exists, appeared at the early stage of deformation. Shear band formation occurred and started collecting dislocation movement which reinforced strain localization quickly within

necking area and finally led to shearing type fracture. It is noticed that PLC effect was only observed at 100℃ with strain rate above 0.03 s^{-1}, and the critical strain triggering the serration flow was delayed compare to that in 25℃. Below strain rate of 0.03 s^{-1}, deformation is relatively uniform before onset of shear band at 100℃. This implies PLC effect is alleviated by higher temperature. The interplay between PLC effect and experimental condition is not a major concern in this paper.

With temperature rises, maximum major strain exceeded 50% at 200℃ and 300℃. In Figure 2-13c and d, strain distribution is relative uniform at the early stage where major strain is less than 25%. After that, strain gradually localizes but still contributes to larger elongation. Inhomogeneous deformation creates strain distribution which leads to higher strain rate within the non-uniform area. Since strain rate hardening effect gradually takes the place of strain hardening with temperature increasing, necking area becomes more and more resistant to elongation due to high strain rate sensitivity. At severe deformation condition where major strain exceeds 70% at 300℃ (last frame in Figure 2-13d), the material used to be covered by painting is exposed to camera observation. DIC is no longer able to evaluate the grey scale value which leaves caves in strain field. At very final stage of deformation, voids in necking area were linked and growing by diffusion which led to cup-and-cone fracture at 300℃ while the fracture at 200℃ is a mixture between shearing type and cup-and-cone type.

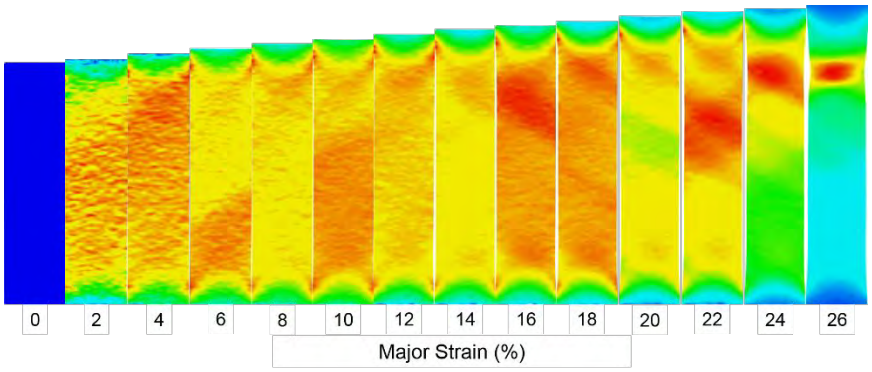
0
2
4
6
8
10
12
14
16
18
20
22
24
26
Major Strain (%)

(a)

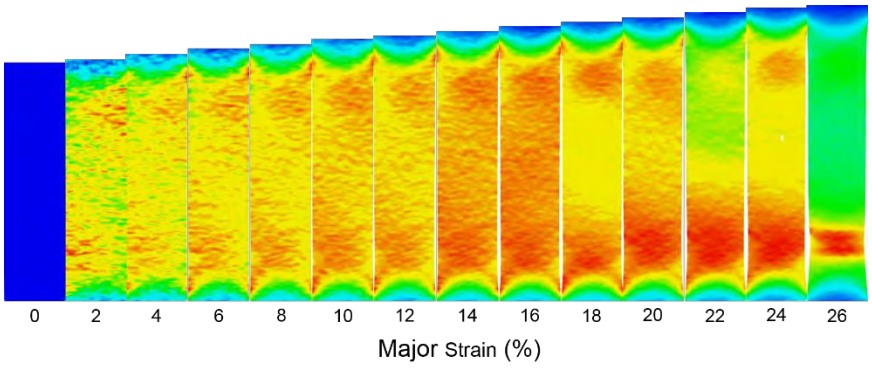
0
2
4
6
8
10
12
14
16
18
20
22
24
26
Major Strain (%)

(b)

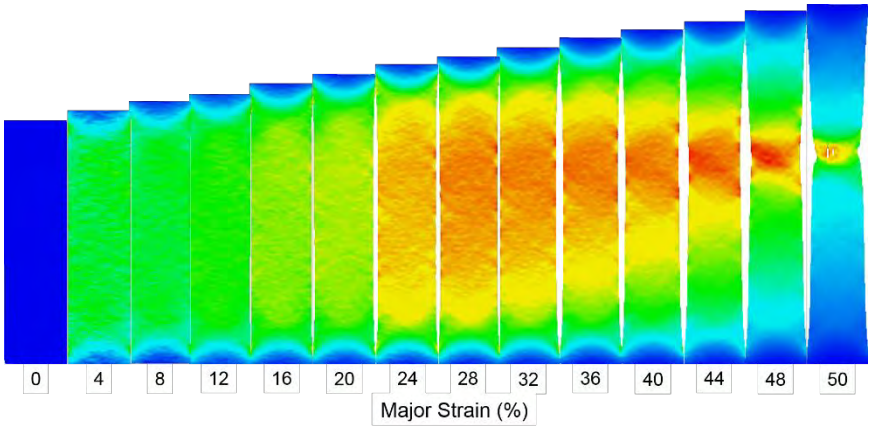
0
4
8
12
16
20
24
28
32
36
40
44
48
50
Major Strain (%)

(c)

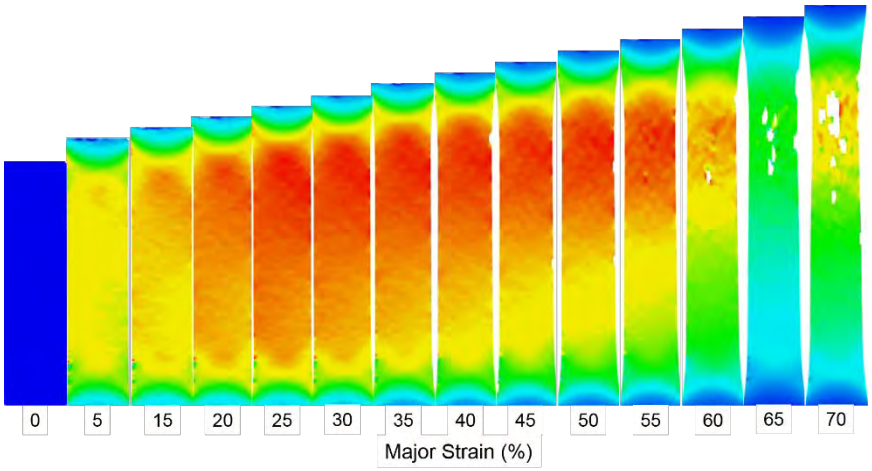

(d)

Figure 2-13: Full-filed strain maps showing major strain distribution over complete gauge area for the uniaxial tensile tests of AA5182-O at temperautre (a) 25℃, (b) 100℃, (c) 200℃, and (d) 300℃ with strain rate of 0.01 s^{-1}.

2.6 Hydraulic Bulge Tests

Besides the ordinary uniaxial tensile testing, hydraulic bulge test is another method to obtain hardening curves of material. During the test, the flat circular specimen is firmly clamped between holders so as to lock the material flow. The hydraulic pressure is then created in the chamber by piston and applied on the specimen to deform the material through the die having a circular aperture until the burst. In this way, the pressure over the specimen is ensured to be uniform and no friction will interfere the strain path. Ideally, the bulge test with isotropic material can generate the perfect balance biaxial loading condition and strain path ($\dot{\varepsilon}_x = \dot{\varepsilon}_y$). Comparing to tensile tests, the most important advantage of hydraulic bulge test is the higher level of attainable plastic strain, up to the localized

necking, which is close to the real condition of most sheet metal forming processes. Although the bulge test has yet been completely standardized like tension test, many improvements have been made and numerous investigations aim at perfecting the approach [70-77]. Other than circular die, elliptical dies with various ratios between minor and major axes are now used to induce the specific strain path on the apex in order to construct the forming limit curves [78].

For this work, the major concern with bulge test is to obtain stress-strain curve at room temperature and extract the yield stress to feed into the yield function (*Yld2000-2d*) for the parameters determination. Conventionally, the determination of true stress-strain curve of bulge test could be done with hydraulic press (p), dome height (h), specimen thickness (t) and the curvature (ρ) which are labeled in the scheme of Figure 2-14b. However, measuring those evolving constants with test progressing could be very complicated and require some assumptions which likely lead to uncertainties and errors. Therefore, utilization of DIC system becomes even more imperative in this situation. With aids of DIC, all the constants can be precisely achieved and no contact measurement tool is needed. Although the idea and technology are mature, the current investigation on bulge test still stays in the preliminary stage. Ideally, the future research will address some problems used to be neglected in literature.

2.6.1 Experimental procedures

Figure 2-14a briefly shows the apparatus for bulge tests integrated with DIC system. The experiment starts with filling the chamber in lower clamp with hydraulic fluid. The material is prepared in circular specimens ($r = 180mm$), decorated with speckle pattern

using black/white paint and placed in the center of die with an opening diameter of 100mm. The upper and lower dies are then closed to achieve a clamp force of 60kN which seals the chamber and locks the material. The pressure within the chamber under specimen ramps up at a rate of 0.5MPa/s controlled by PID controller. Two CCD cameras sitting on top of the hydraulic press (INTERLAKEN SP225) capture the deformation at a decent frame rate. Considering the potential powerful fluid splash after burst, a protection glass, which could also be made of plastic, is placed between the DIC cameras and specimens. The thickness of protection glass is around 0.25" in order to minimize the deflection while still providing adequate strength.

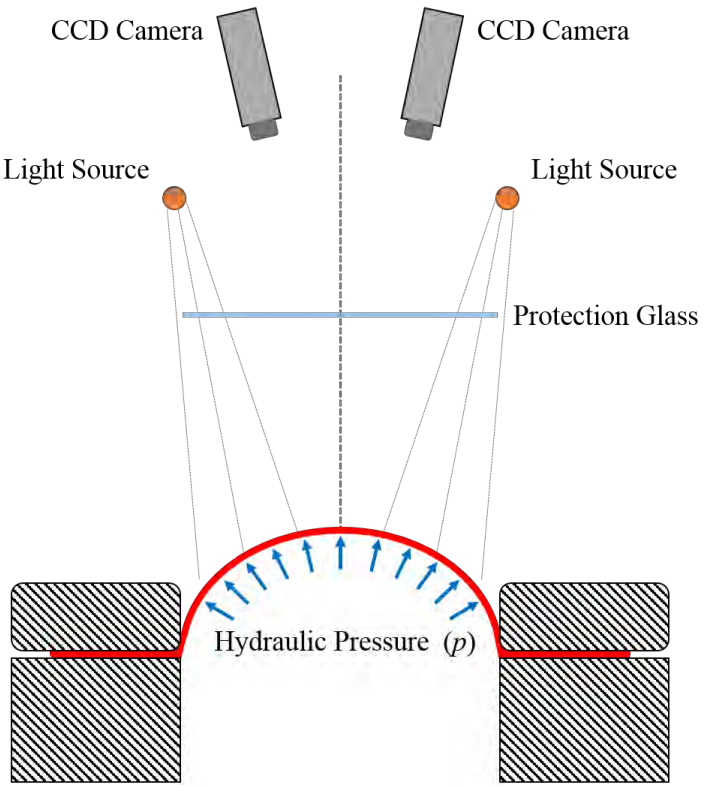

(a)

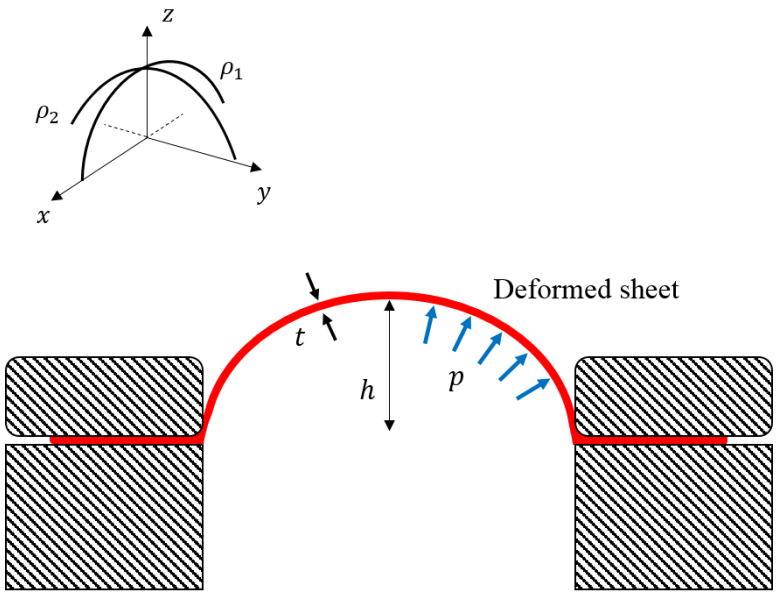

(b)

Figure 2-14: The scheme of (a) hydraulic bulge test set-up with aid of DIC system with (b) all the parameters need to be measured.

2.6.2 Results Analysis

The hydraulic bulge test can be very informative based on the interpretation from different perspectives. For instance, the theoretical analysis of the plastic flow in the elliptical bulge test has been conducted [78]. Recently, a couple of works have been done on the determination of the Forming Limit Curves (FLC) using hydraulic bulge test [79, 80]. In this research, the primary expectation for bulge test is to evaluate the ratio of the yield stresses from bulge test and uniaxial tensile test in 0° which in turns will be needed for the determination of yield function. Thus, the rest of this section will concentrate on extracting the effective stress-strain curve from bulge test with aids of DIC.

Theoretically, the specimen is assumed to carry the isotropic properties and thus the deformation of a small region around the apex can be accepted as uniform during the bulging. The effective stress is then derived in a simple form of

$$\sigma = \frac{p\rho}{2t} \tag{2.5}$$

Thus, the radius of curvature, thickness, and internal pressure must be measured and recorded for the determination of stress-strain curve. Besides Eq. (2.5), a couple of other mathematical equations have also been proposed in literature which aim at compensating the effects of die radius and initial thickness of material [77]. In this study, the curvature radius and effective strain can be directly evaluated by DIC which provides predominant level of accuracy than the conventional spherometer and indicator extensometer device.

The obtained DIC images were processed and correlated to generate the full-field strain maps over the deformed blank. Figure 2-15 presents an example of the processed DIC image. In that image, the dome height is simply achieved by measuring the z-displacement of apex and the apex strain is evaluated based on the pole strain evaluation area which is defined according to ISO standard. Deformed blank specimen needs to be fitted into a primitive sphere in which the radius can be approximately used as curvature.

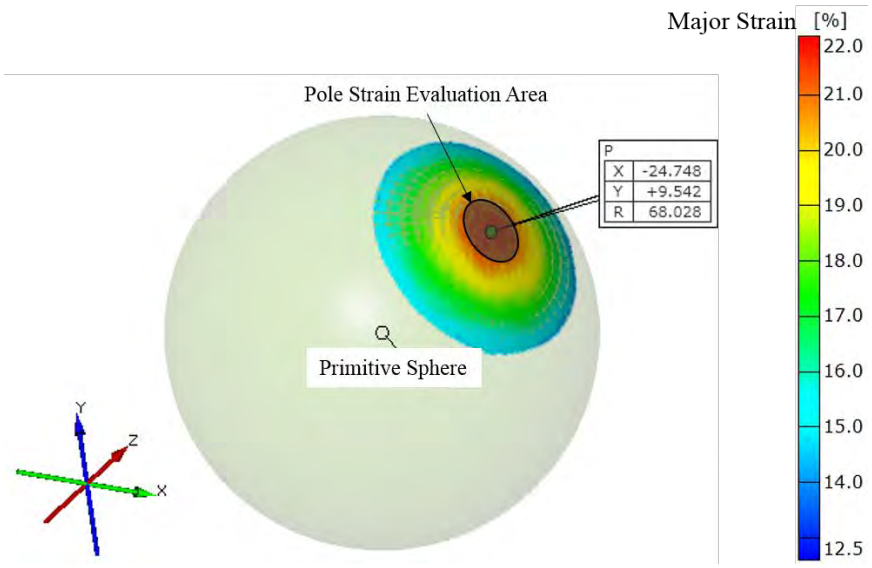

Figure 2-15: An example of the processed DIC image for hydraulic bulge test.

After processing, the obtained effective stress-strain curve is presented in Figure 2-16 along with the one set of curve generated from normal uniaxial tensile test ($\dot{\varepsilon} = 0.01\text{s}^{-1}$) using the specimen in 0°. Obviously, two sets of curves perfectly match to each other up to the maximum attainable plastic strain of the uniaxial tensile test.

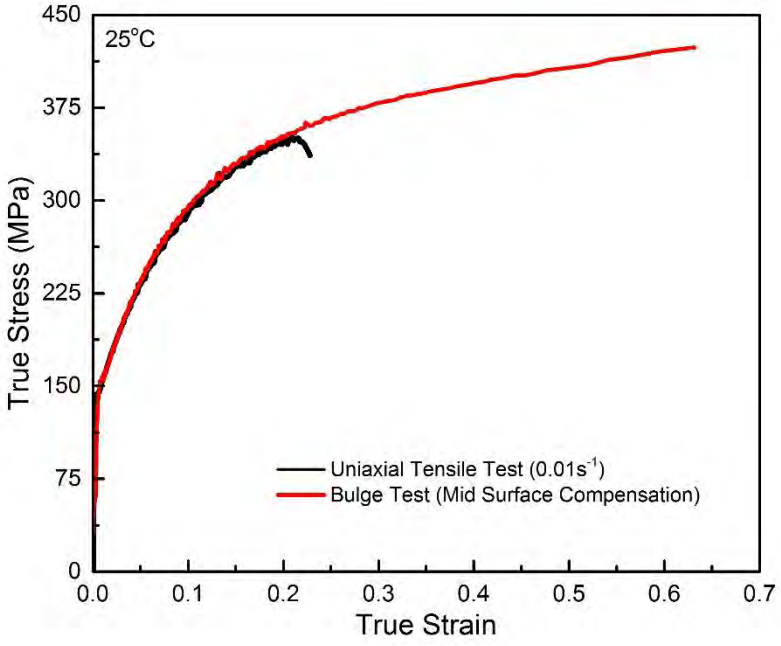

Figure 2-16: Comparison between the stress-stress curves from hydraulic bulge test and uniaxial tensile test.

Alternatively, the conclusion can be drawn that the effective yield stress in balanced biaxial bulge test equals to the yield stress in uniaxial tensile test of the 0° specimen.

$$\sigma_{\text{bulge}} = \sigma_0 \tag{2.6}$$

This conclusion (Eq. (2.6)) will be used as one of the most important input factors in anisotropic yield function (Yld2000-2d) which will be present in detail in Chapter 0.

CHAPTER 3: MATERIAL MODELING

Chapter 2 has covered all the mechanical testing, from fundamental tensile testing to balanced biaxial bulge tests, required to characterize the material properties at different conditions. In the sheet metal forming study, the experimental results, to be really useful and instructive, has to be generalized and modeled in mathematical expression so as to predict the material behavior. This chapter will demonstrate the construction and development of a new phenomenological constitutive model for AA5182-O and determination of the parameters for a well-developed anisotropic yield function (Yld2000-2d) within the experimental condition (25~300℃, 0.001~0.1s^{-1}).

3.1 Constitutive Modeling

Literature review of phenomenological constitutive model

A constitutive model providing the indispensable relation between true strain and true stress is basically essential for any numerical analysis, especially in the cases with complex non-linear finite element simulation. Lin et al. published a paper which presents an extensive review on some experimental results and constitutive models reported in recent years [81]. Most of the constitutive models existed in literature can be generally categorized into three groups: phenomenological, physical-based, and artificial neural network. The phenomenological constitutive model has been widely used due to its simplicity in fitting and convenience in FEA implementation. Plenty efforts have been put in prior literature on developing phenomenological models for hot working of aluminum

alloy sheets. Power-law based models are widely used due to its simplicity in FEA implementation and great capacity of predicting strain hardening behavior. Ayres and Wenner experimentally determined a power law model to satisfy the tensile data of AA5182-O obtained in quasi-static testing between the temperature ranges from 25 to 200℃ [13]. With spanning in strain-rate range, material flow stress becomes more and more dependent on strain rate. It is essential to couple the strain-rate hardening effect into power-law model. For instance, Wagoner model and Nadai model, two extensions of power-law models, are similar in expression and found to be both used in researches of warm deep drawing process of AA5182-O and AA5754-O [12, 59]. Maximum testing temperatures for both works are found to be around 200℃. Aluminum alloys, especially 5182, exhibits great amount of strain hardening in the low temperature range, and this behavior can be well captured by power-law based models with no excessive complication in equation. Modifications of power-law based models were also carried out for the testing above 200℃ where softening behavior begins to interfere material deformation (post-uniform) and flatten the stress-strain curves. In some cases, researchers piece-wise the temperature-dependent functions of material constants (strength coefficients, strain hardening and strain-rate sensitivity) such that the extended models are able to capture material behavior in different temperature ranges. Toros and Ozturk improved Nadai model by introducing more parameters and section the temperature range at 100℃ to describe the flow behavior of 5083-H111 and 5754-O up to 300℃ [82]. With a similar approach in the research on aluminum alloys in direct chill (DC) casting procedure by Alankar and Wells [83], each parameter in Ludwick model was expressed as combination of multiple trendline equations

corresponding to high and low temperature ranges. Due to the challenging experimental conditions (continuous cooling and high testing temperature up to 500℃), the predicted curves does not fit the experimental results with adequate satisfaction. Actually strain hardening exponent (n) was set to equal zero in the high temperature cases where hardening effects became rarely observable. Besides breaking down temperature range, power-law based models can also collaborate with specific governing function in regarding to the relative deformation mechanism. Extended Ludwick model combined with Sellar-Tegart equation was adopted to describe the material behavior of as-cast aluminum alloys at wide temperatures in continuous cooling condition [84]. The comparison between the predicted and experimental results shows very fair agreement. Cheng et al. 2008 [85] applied an exponential term in his work to extend the power-law model to fit AZ31 (which exhibits strong softening behavior) in the temperature range from 150 to 300℃. Xing et al. 2009 [86] also introduced an exponential softening term to a hardening model for Boron steel (22MnB5). However, the effects of such softening terms are critical, because the softening degree varies not only with temperature, but also with strain rate and strain history. The deformation of AA5182-O at higher temperatures can be regarded as a competitive process between hardening and softening. For instance, based on the flow curves at 300℃, hardening behavior can still be observed at higher strain rates ($> 0.03\,s^{-1}$), while the curves at lower strain rates ($<0.003\,s^{-1}$) are dominated by a softening behavior. Besides the family of power-law based models, other phenomenological models were also well investigated. Johnson-Cook model [87] used to be widely used for a variety of materials and has been integrated in a good number of commercial FE software already.

Vural and Caro characterized the flow stress data of 2139-T8 aluminum alloy with modified Johnson-Cook model in a wide range of temperature from -60 to 300℃ and strain-rate from 10^{-4} to $10^{4}s^{-1}$ [88]. However, the fitting curves exhibited only showed coincidence with experimental results below a limited true strain (<0.14). Khan and Huang proposed a constitutive visco-plastic model (KH model) to investigate behavior of 1100 aluminum alloy [89]. In the following research, they modified and extended this model for a variety of aluminum alloys including 5182, 6061and 2024 in quasi-static warm forming [89-92]. Although showing good agreement with experimental stress-strain results, KH model and its extension are thought to be excessively complicated for FE implementation.

In this thesis, one of the major contributions is to model the material behavior under a wide range of forming condition with a decent accuracy.

Model construction

A new phenomenological model is proposed in this work for capturing the behavior of AA5182-O over the entire range of HB-CD, using a piece-wise function as follows:

$$\sigma = \begin{cases} K\varepsilon^{n}\left(\dfrac{\dot{\varepsilon}}{\dot{\varepsilon}_{r}}\right)^{m} & 298K \le T \le 373K \\ \sigma_{peak} - \sqrt{a\exp(b\cdot\varepsilon)} & 373K < T \le 573K \end{cases} \tag{3.1}$$

At low temperatures (cold forming at 25-100 ºC), the power-law model is used to describe the simple hardening behavior of the material. The parameters were extracted by fitting the experimental data in Figure 2-5(a) and Figure 2-5(b), yielding K=560MPa and

$n = 0.28$. The negative strain rate sensitivity, associated with dynamic strain aging (DSA), is accounted for with a constant $m = -0.007$ value. On the other hand, the second function in Equation 4 describes material behavior at higher temperatures (warm to high forming at 150-300 ºC). σ_{peak} is the peak or steady-state stress value, which is predicted by a polynomial function of the Zener-Hollomon parameter:

$$\sigma_{peak} = -0.5285 \cdot [\ln(Z)]^2 + 47.808 \cdot \ln(Z) - 744.47 \tag{3.2}$$

where a and b are two parameters, which by fitting to the experimental data were found to be dependent on temperature, strain rate and Z values according to the following expressions:

$$\begin{aligned} a &= 141.18 \cdot (\ln(Z))^2 - 6301.6 \cdot \ln(Z) + 69623 \\ b &= (-0.0099T + 1.5796) \cdot (\ln(\dot{\varepsilon}))^2 \\ &\quad + (-0.0977T + 14.844) \cdot \ln(\dot{\varepsilon}) + (\sigma - 0.1966T - 2.0188) \end{aligned} \tag{3.3}$$

Figure 3-1 includes the direct comparison between model-predicted and experimentally-obtained stress-strain curves for four selected temperature with each covering fiver strain rates. Considering 100℃ has similar stress-strain curves with 25℃ and 200℃ is more representative than 150℃ with higher strain-rate sensitivity, the fitting curves for 100℃ and 150℃ are not shown. In general, the proposed model is capable of prediction the material behavior with acceptable accuracy. Negative strain-rate sensitivity captures the inverse relationship between flow stress and strain rate at 25℃. Softening

behavior at high temperatures with large strain is also predictable. However, more deviation between prediction and experimental results is noted in the low strain-rate range for 200℃ and high strain-rate range for 300℃.

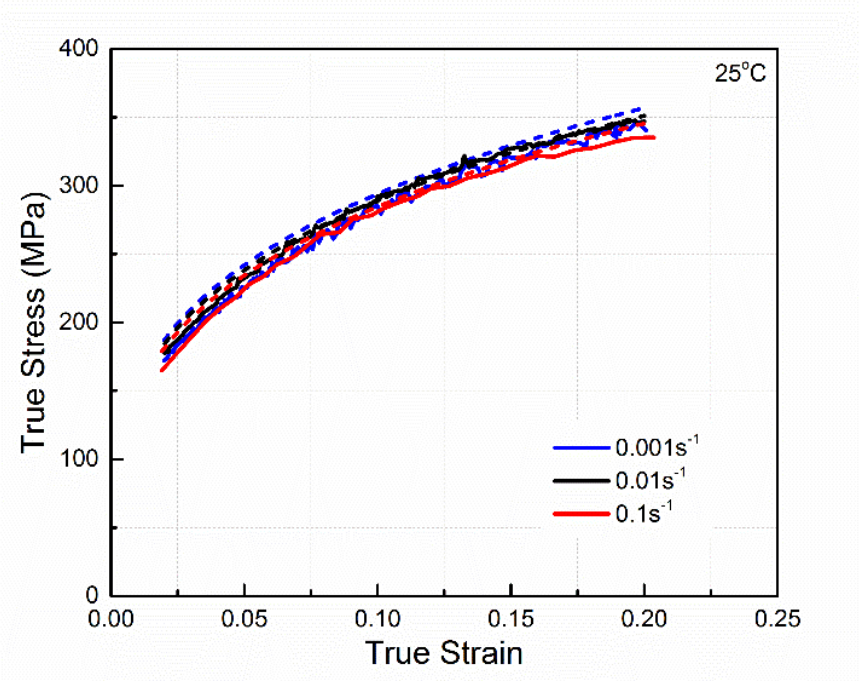

(a)

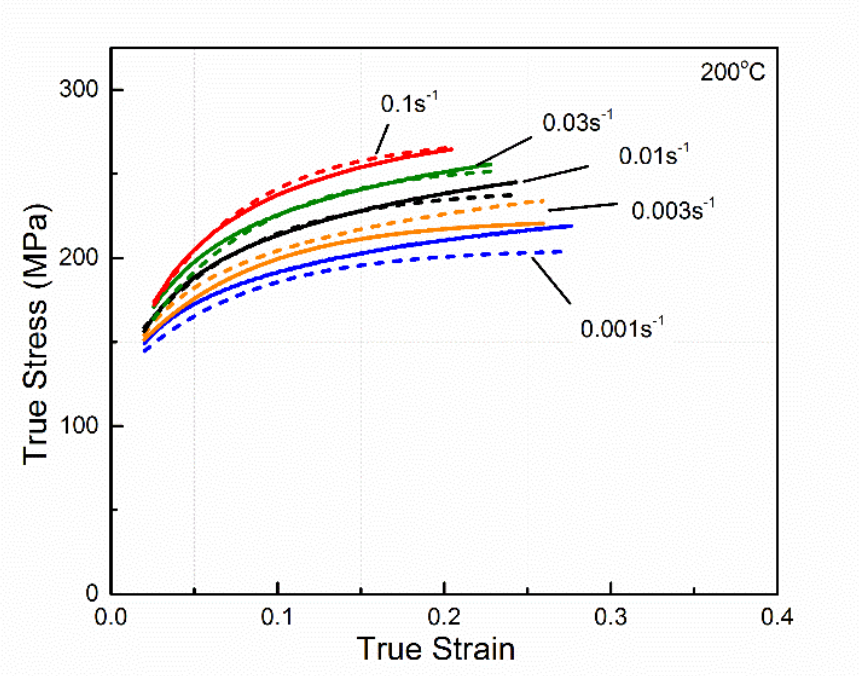
200°C
0.1s-1
0.03s-1
0.01s-1
0.003s-1
0.001s-1
True Stress (MPa)
True Strain
0
100
200
300
0.0
0.1
0.2
0.3
0.4

(b)

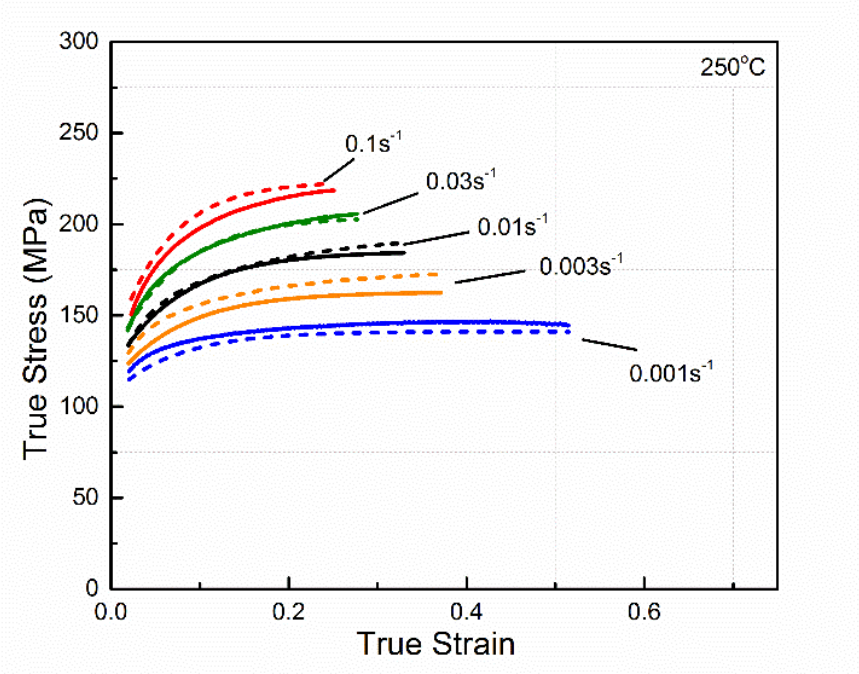
250°C
0.1s-1
0.03s-1
0.01s-1
0.003s-1
0.001s-1
True Stress (MPa)
True Strain
0
50
100
150
200
250
300
0.0
0.2
0.4
0.6

(c)

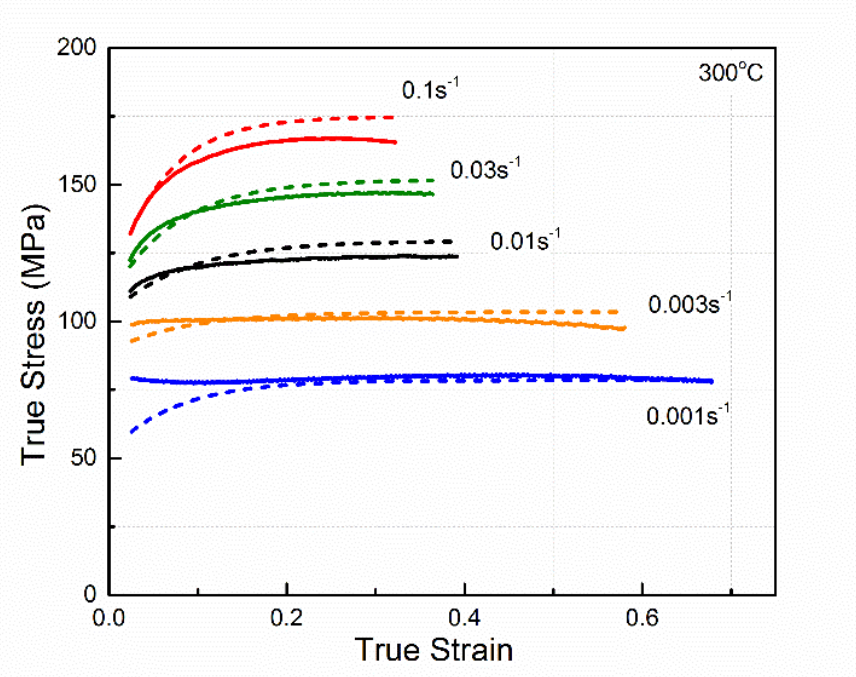

(d)

Figure 3-1: Experimental (solid) versus model-predicted (dot) true stress-strain curves for the entire strain rate range of this work, at a selected temperature of (a) 25℃, (b) 200℃, (c) 250℃ and (d) 300℃.

Figure 3-2 presents another comparison for all the temperatures, at a selected strain rate of $0.01s^{-1}$. It is seen that the deviation between the two is reasonably small, which illustrates the suitability and validity of the proposed model for this particular wide range of conditions in HB-CD. Elimination of *n* and *m* values at elevated temperatures avoids the degradation in modeling accuracy at large plastic strain accumulations. The model does particularly well at large strains ($\varepsilon > 0.5$) where a near steady state in the flow behavior is achieved. For 300℃ in particular, the model shows the ability to capture the apparent

hardening behavior associated with the higher strain rates, and the shift towards more of a softening behavior at lower strain rates.

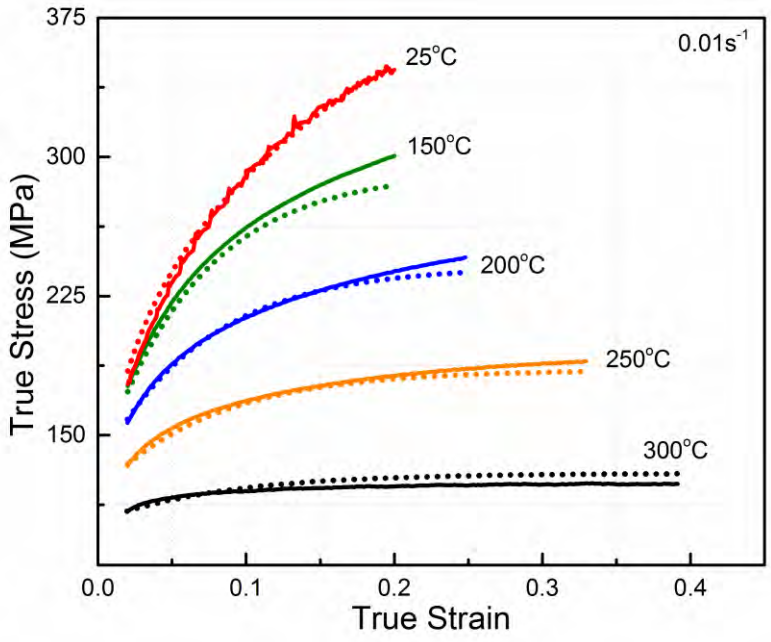

Figure 3-2: Experimental (solid) versus model-predicted (dot) true stress-strain curves for the entire temperature range of this work, at a selected strain rate of $0.01s^{-1}$ (Note that the curves for 100 ºC coincide with 25 ºC, and thus were not shown here).

Viscoplasticity model

The previous section has already presented a relatively mature rate-dependent constitutive model that satisfies the requirement of predicting the stress-strain behavior of AA5182-O in a wide range of temperature and strain-rate. However, the previous model is proved to be unsuitable in the VUMAT explicit stress integration algorithm, which will be discussed with more details in next Chapter. As a consequence, another viscoplasticity model is prompted to be developed on the basis of the previous model. The viscoplasticity

describes the rate-dependent properties of material during the inelastic deformation. Chaboche has reviewed some plasticity and viscoplasticity constitutive theories in literature [93]. To escape from too much distractions, this thesis will not dive deep into the viscoplasticity theories and literature review of the viscoplasticity models.

The principle of this modification is simple: modify the model for high temperature range (200~300°C) to make it possible to be reorganized into the form of $\dot{\varepsilon} = f(\sigma, \phi)$ after linearization where the ϕ represents the internal variables. Recall the Eq. (3.1) and Eq. (3.3), all the parameters (a and b) in the second part of Model-1 for high temperatures are dependent on strain rate. Moreover, it will become extremely intricate to reorganize the model as needed. Therefore, a new viscoplasticity model has been developed and proposed as:

$$\sigma = \begin{cases} K\varepsilon^{n}\left(\dfrac{\dot{\varepsilon}}{\dot{\varepsilon}_r}\right)^{m} & 25 \le \mathrm{T} \le 150^{\circ}\mathrm{C} \\ K_0\varepsilon^{n_0} \cdot (K_1\varepsilon^{n_1}) & 150 < \mathrm{T} \le 300^{\circ}\mathrm{C} \end{cases} \tag{3.4}$$

In the low temperature range (25~150°C), the model remains the same with Eq. (3.1). In the high temperature range, the model has been modified into the multiplication of two power-law models both of which consist of the parameters of K and n. Those four parameters are expressed as:

$$\begin{aligned} K_0 &= -1.9435 \cdot T + 653.7 \\ n_0 &= -0.0013 \cdot T + 0.3928 \end{aligned} \tag{3.5}$$

and

$$K_1 = (p_1 \cdot T^3 + p_2 \cdot T^2 + p_3 \cdot T + p_4)\dot{\varepsilon}^{p_5}$$
$$n_1 = ((8.5\times10^{-7}) \cdot T^2 - 2.9\times10^{-4} \cdot T + 0.035) \cdot \log(\dot{\varepsilon}) + 4.58\times10^{-4} \cdot T - 0.019 \quad (3.6)$$

where $p_1 = 1.972 \times 10^{-6}$, $p_2 = -1.133 \times 10^{-3}$, $p_3 = 0.2181$, $p_4 = -12.46$, and $p_5 = 0.008089 \cdot exp(0.01038 \cdot T)$. The first power-law equation can be seen as the calculation of viscous stress while the second equation aims at coupling the strain rate effect into the model.

Figure 3-3 presents two plots that compare the experimental results and model predicted results using the proposed viscoplasticity model at 200ºC and 300ºC. The model still exhibits the good capacity of predicting the material properties in wide range of strain rate. Obviously, modifying the model does not significantly compromise the accuracy of predicted results.

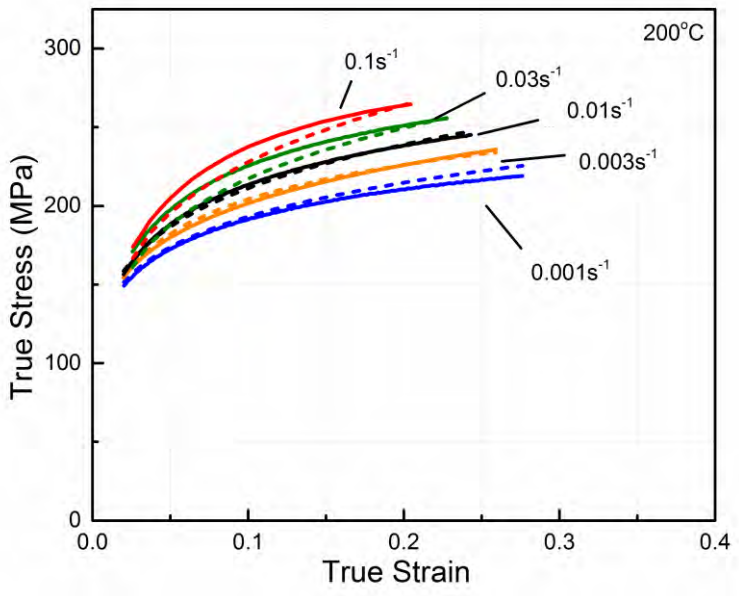

(a)

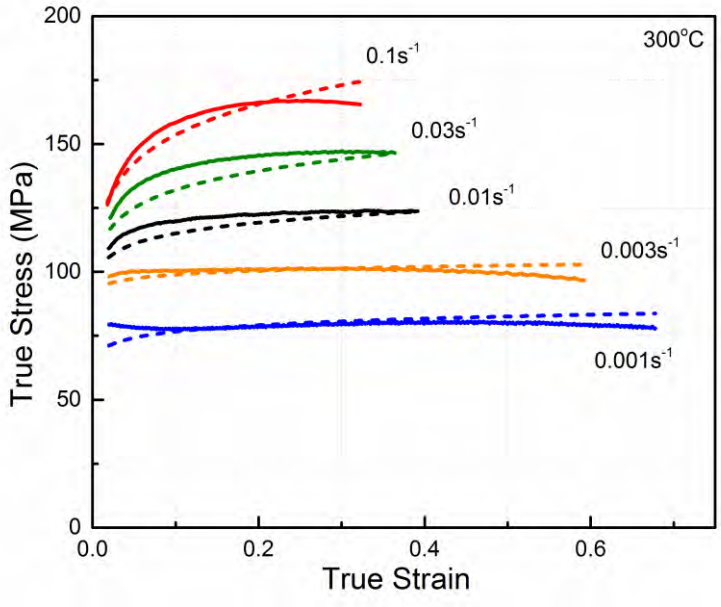

(b)

Figure 3-3: Experimental (solid) versus model-predicted (dot) using viscoplasticity model at a selected temperature of (a) 200℃ and (b) 300℃.

Figure 3-4 shows a comparison of the stress-strain curves at all the selected temperatures with strain rate of $0.01s^{-1}$. It is clearly seen that the proposed model is still capable of describing the hardening and softening behavior of material at both low and high temperature ranges. Although the predicted curves at 250ºC slightly deviates from the experimental results comparing to the prediction result from Model-1, this new model still presents decent prediction accuracy over the entire temperature range and large strain conditions as well.

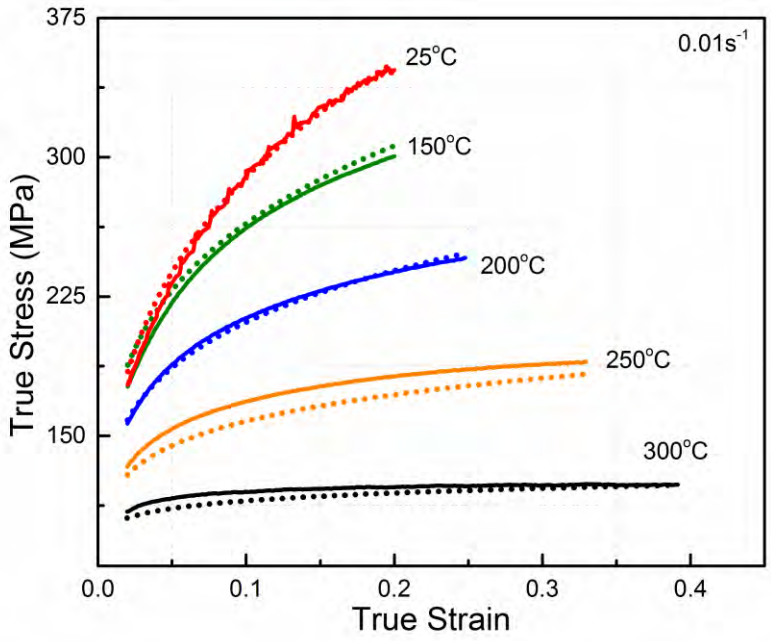

Figure 3-4: Experimental (solid) versus model-predicted (dot) true stress-strain curves using the viscoplasticity model at a selected strain rate of $0.01s^{-1}$ (Note that the curves for 100 ºC coincide with 25 ºC, and thus were not shown here).

Overall, this proposed viscoplasticity constitutive model consists of a reduced number of parameters which minimize the work of curve fitting. The predicted stress-strain curves exhibit good correlation with experimental results. In the Chapter 4.1 , this model will be recalled and used in an explicit stress integration algorithms that will be implemented into the user subroutine (VUMAT) for the coupled thermal-mechanical finite element simulations.

3.2 Anisotropic Yield Function

Stamping generally involves with arbitrary deformation paths which depends on particular die design. Thus material anisotropy behavior is imperative as well as difficulty in FE simulation. The Yld2000-2d anisotropic yield function presented by Barlat [55] has been proved to be one of the most accurate model to predict the anisotropic behavior of commercial aluminum alloys. According to the previous study, the simulation results of both Yld96 and Yld2000-2d models are similar [94, 95]. However, YLD2000-2d overcomes three problems with respect to the FEA implementation and simulation:

(i) There is no proof of convexity which important to ensure the uniqueness of a solution.

(ii) The derivatives are difficult to obtain analytically which complicate the implementation.

(iii) Some of the numerical problems with full stress states might be difficult to solve because of the relative complexity of the YLD96 formulation.

The Yld2000-2d function for plane stress plasticity ($\sigma_z = \sigma_{yz} = \sigma_{zx} = 0$) is generally expressed by [55]

$$\phi = \phi' + \phi'' = 2\bar{\sigma}^a \tag{3.7}$$

where $\bar{\sigma}$ is the flow stress, exponent "a" is a material coefficient, and ϕ' and ϕ'' are given by

$$\begin{aligned}\phi' &= \left|X_1' - X_2'\right|^a \\ \phi'' &= \left|2X_1'' + X_2''\right|^a + \left|X_1'' + 2X_2''\right|^a\end{aligned} \tag{3.8}$$

The exponent " a " in Eq. (3.7) is associated with the crystal structure. Recommended values of "a" are $a = 8$ for FCC materials and $a = 6$ for BCC materials. However, it was also reported in Dion-Martin et al. [96] that $a = 5$ works better for AA5754. In Eq. (3.8), $X_{1,2}'$ and $X_{1,2}''$ are the principal values of $\boldsymbol{X}'$ and $\boldsymbol{X}''$ which are derived from linear transformations on the stress deviator defined as

$$\begin{aligned}\begin{bmatrix} X_{xx}' \\ X_{yy}' \\ X_{xy}' \end{bmatrix} &= \begin{bmatrix} C_{11}' & C_{12}' & 0 \\ C_{21}' & C_{22}' & 0 \\ 0 & 0 & C_{33}' \end{bmatrix} \begin{bmatrix} s_{xx} \\ s_{yy} \\ s_{xy} \end{bmatrix} \\ \begin{bmatrix} X_{xx}'' \\ X_{yy}'' \\ X_{xy}'' \end{bmatrix} &= \begin{bmatrix} C_{11}'' & C_{12}'' & 0 \\ C_{21}'' & C_{22}'' & 0 \\ 0 & 0 & C_{33}'' \end{bmatrix} \begin{bmatrix} s_{xx} \\ s_{yy} \\ s_{xy} \end{bmatrix}\end{aligned} \tag{3.9}$$

where subscripts x and y represent the rolling and transverse directions of the sheet, respectively. The transformation can also apply to the Cauchy stress tensor as

$$\begin{aligned}\boldsymbol{X}' &= \boldsymbol{C}' \cdot \boldsymbol{s} = \boldsymbol{C}' \cdot \boldsymbol{T} \cdot \sigma = \boldsymbol{L}' \cdot \sigma \\ \boldsymbol{X}'' &= \boldsymbol{C}'' \cdot \boldsymbol{s} = \boldsymbol{C}'' \cdot \boldsymbol{T} \cdot \sigma = \boldsymbol{L}'' \cdot \sigma\end{aligned} \tag{3.10}$$

where the transformation matrix, $\boldsymbol{T}$, is

$$\boldsymbol{T}=\begin{bmatrix} 2/3 & -1/3 & 0 \\ -1/3 & 2/3 & 0 \\ 0 & 0 & 1 \end{bmatrix} \tag{3.11}$$

The tensor $\boldsymbol{L}'$ and $\boldsymbol{L}''$ can be represented with eight independent coefficients α_k ($k=1\sim 8$) as

$$\begin{bmatrix} L'_{11} \\ L'_{12} \\ L'_{21} \\ L'_{22} \\ L'_{66} \end{bmatrix}=\begin{bmatrix} 2/3 & 0 & 0 \\ -1/3 & 0 & 0 \\ 0 & -1/3 & 0 \\ 0 & 2/3 & 0 \\ 0 & 0 & 1 \end{bmatrix}\begin{bmatrix} \alpha_1 \\ \alpha_2 \\ \alpha_7 \end{bmatrix} \tag{3.12}$$

And

$$\begin{bmatrix} L''_{11} \\ L''_{12} \\ L''_{21} \\ L''_{22} \\ L''_{66} \end{bmatrix}=\frac{1}{9}\begin{bmatrix} -2 & 2 & 8 & -2 & 0 \\ 1 & -4 & -4 & 4 & 0 \\ 4 & -4 & -4 & 1 & 0 \\ -2 & 8 & 2 & -2 & 0 \\ 0 & 0 & 0 & 0 & 9 \end{bmatrix}\begin{bmatrix} \alpha_3 \\ \alpha_4 \\ \alpha_5 \\ \alpha_6 \\ \alpha_8 \end{bmatrix} \tag{3.13}$$

Thus, eight coefficients are needed to be determined to describe the material anisotropy. Ideally, eight input data extracted from the tensile tests at 0, 45 and 90 degree to rolling direction and balanced biaxial tests, namely σ_0, σ_{45}, σ_{90}, σ_b, r_0, r_{45}, r_{90}, and

r_b, are needed to resolve the eight independent coefficients. Figure 3-5 summarizes the derived yield stresses from uniaxial tensile testing at plastic work of 30MPa.

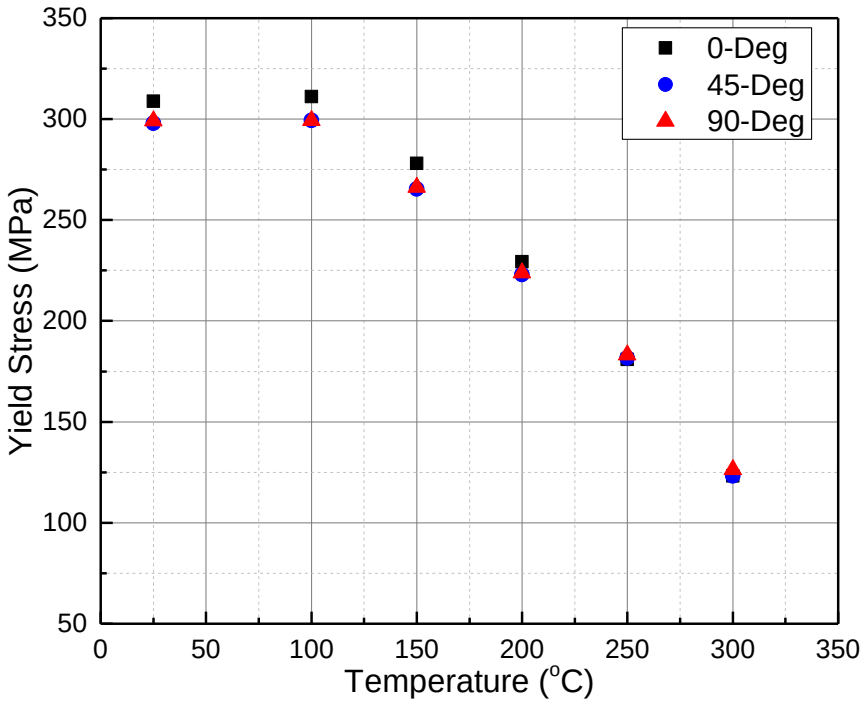

Figure 3-5: Yield stress at $0.01s^{-1}$ different temperatures with 30MPa of plastic work

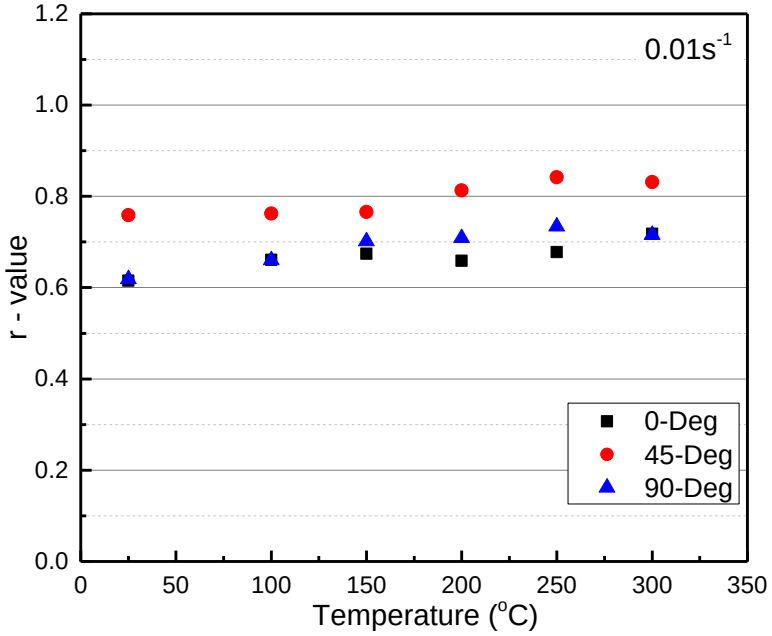

Figure 3-6: Plastic anisotropy parameters (R-value) for AA5182-O at temperatures range from 25℃ to 300℃, calculated at $0.01s^{-1}$ true strain rate.

In the Chapter 2, the balanced biaxial bulge test has been carried out and revealed the result of $\sigma_b / \sigma_0 = 1$. r_b, which characterizes the slope of the yield surface in balanced biaxial tension, is replaced by assuming $L''_{12} = L''_{21}$. Hence, the eight yield function coefficients can be calculated a set of non-linear equations with Newton-Raphson non-linear solver for which the details can be found in the original paper for Yld2000-2d [55]. Moreover, the capability of Yld2000-2d has been extended to the warm temperature range by fitting the parameters using the experimental data at elevated temperatures. Table 2 summarizes the obtained α_k values at various temperatures. For the sake of conscience in FEA implementation, those parameters have been modeled as the 3rd order temperature dependent functions which is presented in Table 3. As an example, the values of α_1 at

different temperatures are plotted with the fitting curve using the achieved function in the Figure 3-7. It has been seen that the obtained model is reliable in calculating the parameters for the proposed yield function. As a consequence, Yld2000-2d can be easily fed into the FEA software to couple the anisotropic behavior of the material.

Table 2: Coefficients for Yld2000-2d at different temperatures

Temperature (°C)	α_1	α_2	α_3	α_4	α_5	α_6	α_7	α_8
25	0.9139	1.0306	0.9498	1.0357	1.0140	0.9498	1.0068	1.1222
100	0.9114	1.0512	0.9496	1.0379	1.0117	0.9496	1.0093	1.1283
150	0.9003	1.0739	0.9495	1.0381	1.0116	0.9495	1.0160	1.1467
200	0.9223	1.0359	0.9610	1.0253	1.0136	0.9610	1.0066	1.0932
250	0.9775	0.9578	0.9841	1.0015	1.0141	0.9841	0.9837	1.0140
300	1.0103	0.9183	0.9925	0.9957	1.0115	0.9925	0.9860	1.0254

Table 3: Anisotropic coefficients for the Yld2000-2d material model as functions of temperatures and R-squared values

Anisotropy Coefficient	3rd Order Fit Function	R-squared
α_1	$3.17\times10^{-10}T^3+2.63\times10^{-6}T^2-5.27\times10^{-4}T+0.92763$	0.8962
α_2	$6.37\times10^{-9}T^3-7.50\times10^{-6}T^2+1.39\times10^{-3}T+0.99683$	0.8649
α_3	$-3.11\times10^{-9}T^3+2.44\times10^{-6}T^2-3.28\times10^{-4}T+0.95731$	0.9134
α_4	$4.83\times10^{-9}T^3-3.28\times10^{-6}T^2+4.44\times10^{-4}T+1.02568$	0.8980
α_5	$-2.03\times10^{-9}T^3+1.01\times10^{-6}T^2-1.37\times10^{-4}T+1.01689$	0.8125
α_6	$-3.11\times10^{-9}T^3+2.44\times10^{-6}T^2-3.28\times10^{-4}T+0.95731$	0.9134
α_7	$4.67\times10^{-9}T^3-3.04\times10^{-6}T^2+4.51\times10^{-4}T+0.99606$	0.5631

α_8	$2.50\times10^{-8}T^3-1.47\times10^{-5}T^2+1.96\times10^{-3}T+1.07704$	0.7019

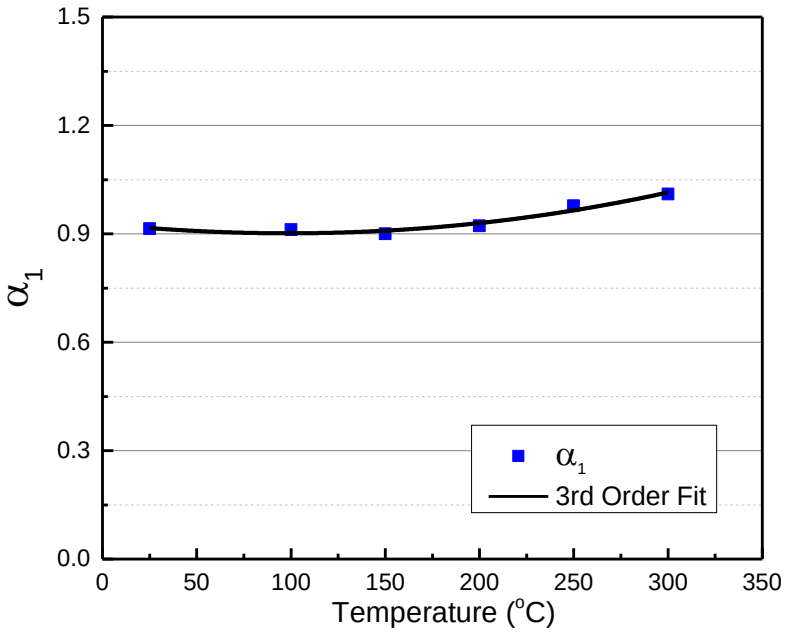

Figure 3-7: The values of α_1 at different temperatures and it 3rd order fitting curve.

In Figure 3-8, the contour plot illustrates the evolving surfaces with increasing of the shear stress (σ_{xy}) at 25℃. The shrinkage of the surfaces presents a gradual and smooth changing process of the yield surface under the effect of shear stress.

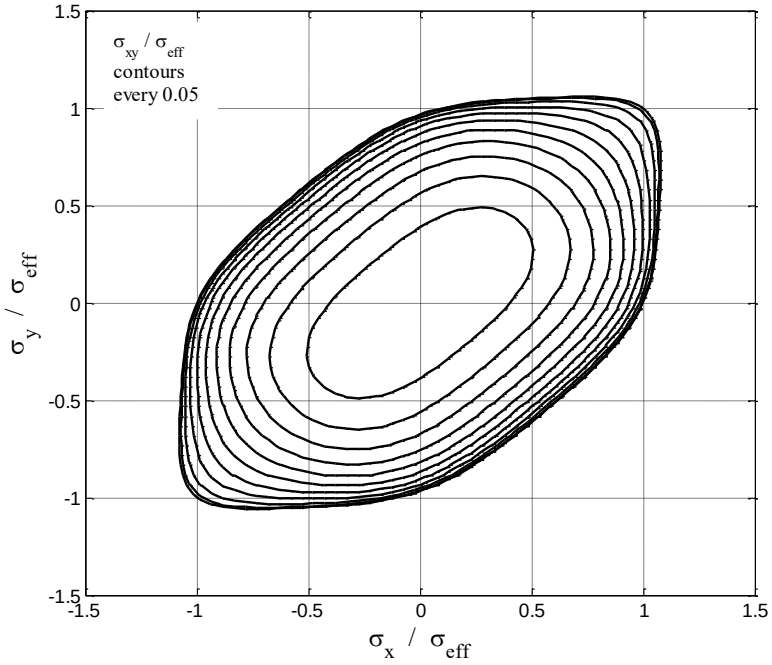

Figure 3-8: Yield surfaces for AA5182-O at 25℃ with 0.05 increment in $\sigma_{xy} / \sigma_{eff}$

With the presence of the parameters for Yld2000-2d at elevated temperatures, the yield surfaces can be contoured using yield function and compared with the von Mises yield surface which depicts the typical isotropic material behavior. Figure 3-9 contours the yield surfaces of AA5182-O at three selected temperatures: 25℃, 200℃, and 300℃. The material is approaching the isotropic behavior as the temperature increasing. Nonetheless, the material is still carrying anisotropic character at 300℃.

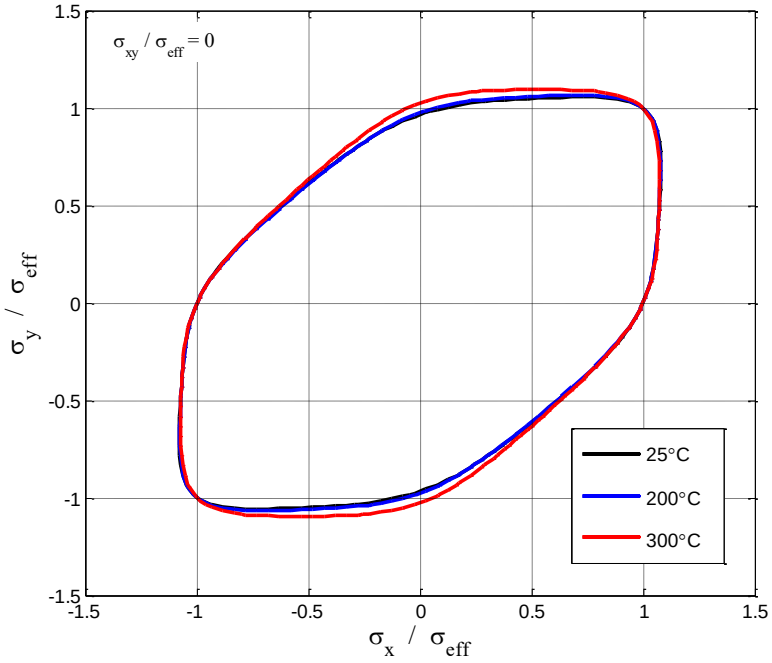

Figure 3-9: Yield surfaces for AA5182-O at 25℃, 200℃ and 300℃ with $\sigma_{xy} = 0$

3.3 M-K Model

For the better control of deforming a part out of stamping die without failure or rupture, it is imperative to explore the forming limit of material. One of the most popular tools to assess the sheet metal formability is the forming limit diagram (FLD) introduced by Keeler and Backofen in the 1960s [97]. In the FLD, forming limit curves (FLC), which predict the critical strain, are constructed in the space bounded by major and minor strain. Each set of FLC normally covers the loading conditions range from uniaxial to balanced biaxial. Figure 3-10 shows a set of exemplary FLC with presence of the linear strain paths of different loading conditions.

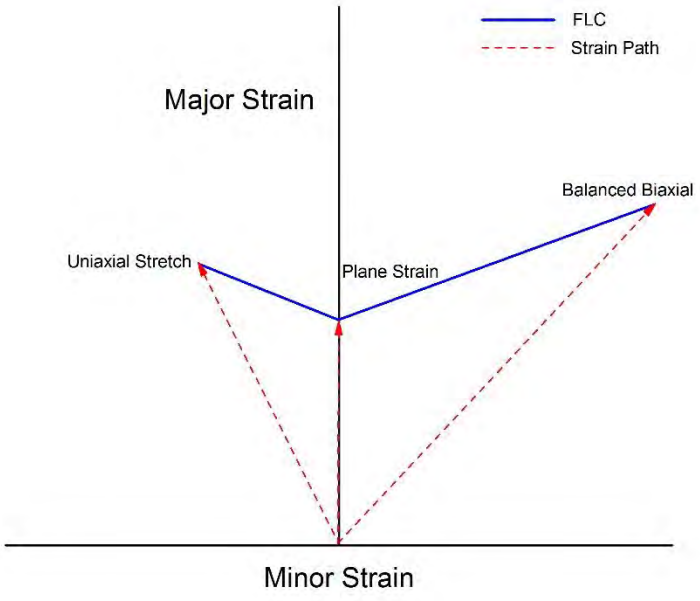

Figure 3-10: A demonstration presents the FLC with linear strain path.

In lab, the in-plane (Nakajima) or out-of-plane (Marciniak) testing is essential to experimentally construct the FLC of material. In both tests, the material is firstly prepared as specimens with various width which will produce different ratios of major to minor strain under the stretch. During the tests, the specimens are punched using a dome head or flat punch until the localized necking is observed. Then the total strain accumulated before the onset of necking is determined as the critical strain. the scatter of these critical strains construct the FLC. Ideally, this strain-based FLC (ε-FLD) is able to predict the necking of material as long as the strain is linearly growing. However, the problem with the ε-FLD is that it is only valid when the loading process is linear. Many works, such as Graf and Hosford [98], have already illustrated that the experimentally obtained critical strain is significantly influenced by strain path. Alternatively speaking, the ε-FLC is unsuitable for some forming process, such as stamping, which involves nonlinear loading condition. On the other side, Kleemola and Pelkkikangas proposed a concept of stress-based FLD (σ-FLD) in 1977 [99] as an alternative of ε-FLD to eliminate the strain-path effects. The σ-FLD did not receive enough recognition until recent decade during which several publications refocus and rediscover the necessity of developing a σ-FLD [100-105].

Evaluating the feasibility of strain-based and stress-based is not the focus of the present work. This section only presents a preliminary study of FLD, including both strain-based and stress-based, for AA5182-O at wide range of temperature. Conducting the formability test at elevated temperature condition requires to universally heat up the set-up and maintain the temperature level during the test which unfortunately beyond the current capability of the lab. Alternatively, a mathematical calculation of Marciniak-Kuczynski

model is selected here to determine the FLC. Marciniak and Kuczynski [106] proposed a calculation model based on the hypothesis of the existence of an geometrical imperfection (groove) in the sheet metal as illustrated in Figure 3-11. During the stretching process, this imperfection progressively evolves and accumulates more plastic strain than the homogeneous area.

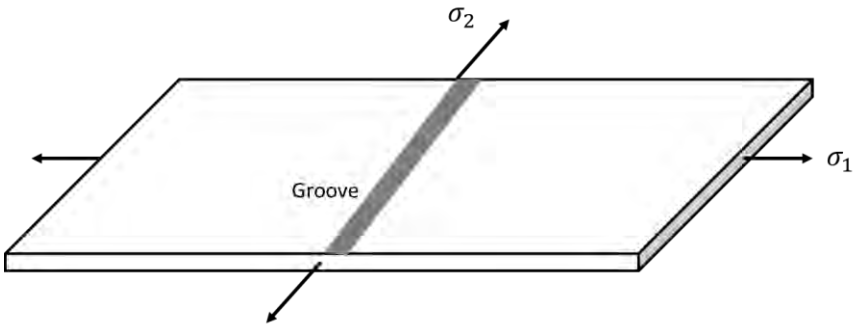

Figure 3-11: Schematic of the hypothesis of M-K calculation model.

The localized necking occurs when the ratio of the increment of plastic strain in imperfection and homogeneous region equals or higher than 10 ($\frac{d\varepsilon^b}{d\varepsilon^a} \geq 10$). The total plastic strain in the homogeneous region is then determined as the critical strain. To construct the full scale of a FLC, the critical strains must be calculated for all the ratio of $\frac{\sigma_1}{\sigma_2}$ ranges from 0 to 1 which covers the loading conditions from the uniaxial to the balanced biaxial. Moreover, the major and minor stresses at the critical condition can be extracted as the same time which are the components to construct the σ-FLD.

A number of publications aim at developing the algorithms to calculate FLD can be found in literature [107-109]. This work follows the steps demonstrated by Ganjiani [108] which has been proved to be a robust and stable algorithm. Figure 3-12 presents a flowchart which briefly demonstrates the process of calculating the critical strains and stresses with M-K model.

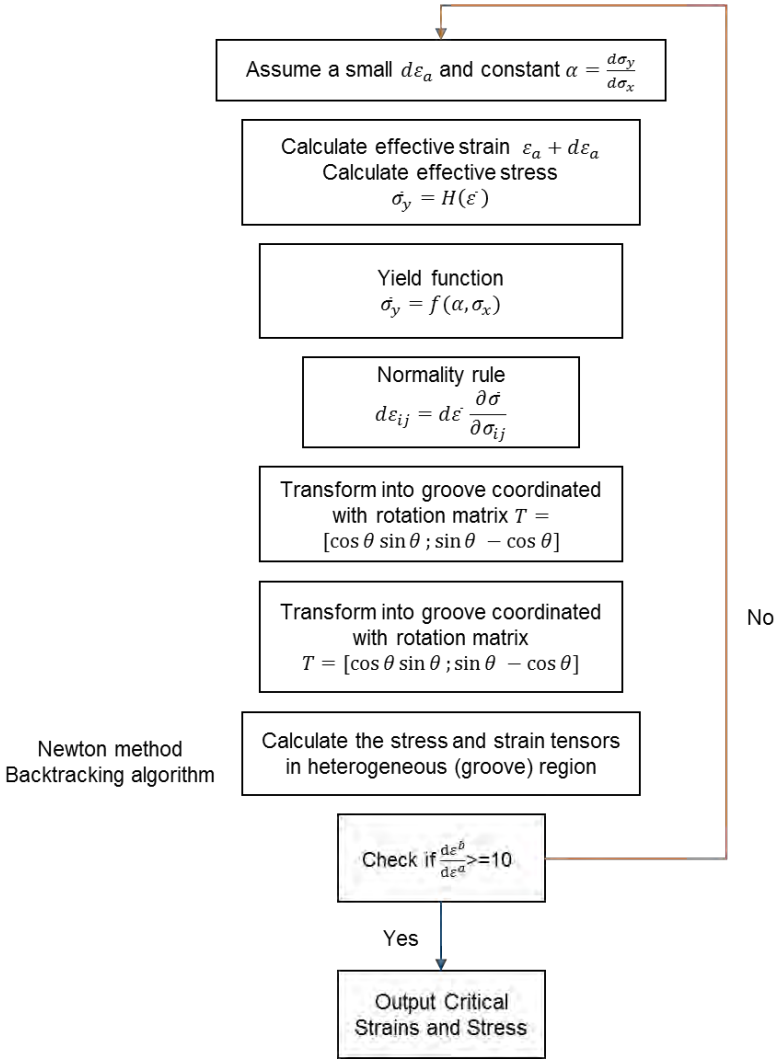

Figure 3-12: The flow chart demonstrates the process of calculating the critical strains and stresses with M-K model to construct the ε-FLD and σ-FLD.

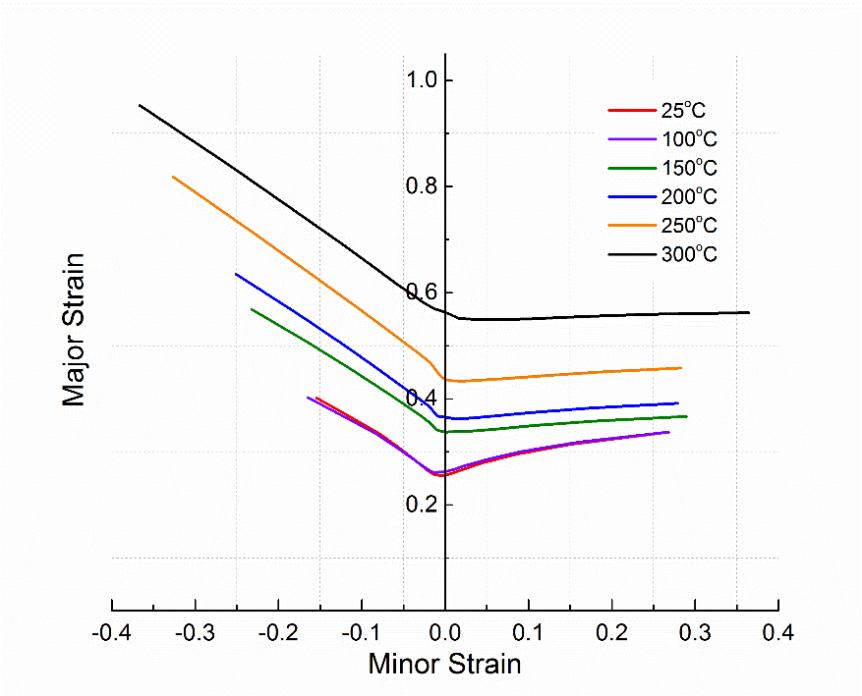

Figure 3-13: Calculated ε-FLD covering the temperature ranges from 25℃ to 300℃ at strain rate of $0.01s^{-1}$.

The constitutive model developed in Chapter 3 with von Mises yielding function were implemented. With Newton's method and backtracking algorithms, the ε-FLD and σ-FLD of AA5182-O at various temperatures are obtained and presented in Figure 3-13 and Figure 3-14. As it is shown in figures, elevating the temperature will globally increase the critical strain for all the loading conditions and dramatically decrease the flow stress level at the same time.

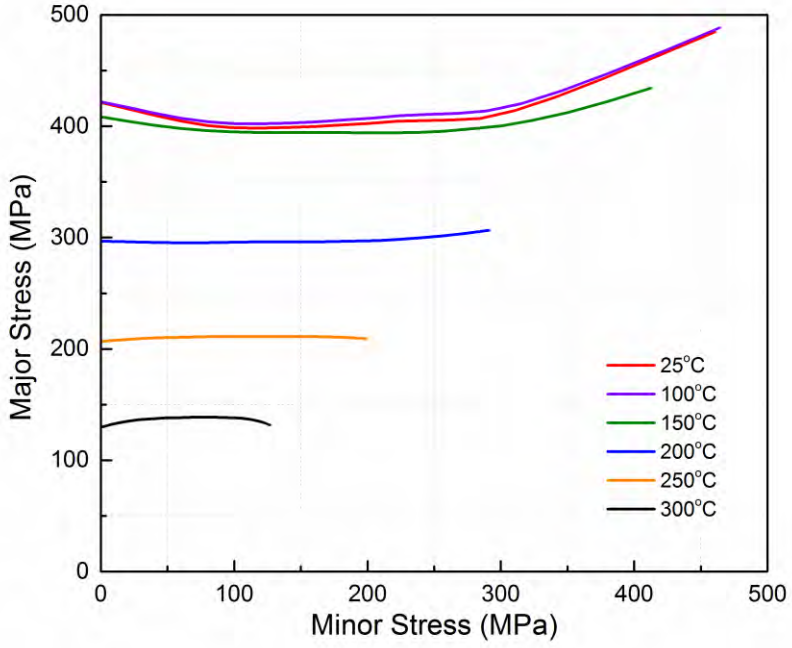

Figure 3-14: Calculated σ-FLD covering the temperature ranges from 25℃ to 300℃ at strain rate of $0.01s^{-1}$.

CHAPTER 4: STRESS INTEGRATION IN FINITE ELEMENT SIMULATIONS

In industry, finite element simulation is becoming an imperative tool for structural analysis providing the instructive and intuitive results. A number of research works have proved that the application of FEA can help to have a better understanding of the metal forming process by predicting many process parameters, including forming defects, punch load, strain and stress distribution [12, 15, 95, 110-115]. Meanwhile, a lot of commercial codes with user-friendly GUI have been developed to push forward the application of FEA in industry. The existing FEA solvers for quasi-static problems are implicit and explicit. The implicit method is unconditionally stable with respect to the size of the time increment and has been applied in 2D metal forming simulation. On the contrary, explicit solver is widely adopted in the 3D non-linear cases with complex contact that could lead to convergence problem in implicit method. The problem this research is addressing is to ultimately simulate a 3D full scale hot stamping process which is highly non-linear and probably involves in multiple shell-to-solid contact pairs. Therefore, ABAQUS/Explicit solver is used in this research to perform the finite element simulations.

Fundamentally, a reliable analysis simulation significantly depends on the implemented material models which basically determine material behavior on element level. Although carrying a lot of build-in material models, many commercial FEA software, such as ABAQUS and LS-Dyna, still allow the users to define subroutines for some specific problems. The forming condition in this research works covers a wide range of temperature and strain rate where multiple deformation mechanisms are involved. It will

be extremely time consuming and fallible to directly import all the experiment data sets. Thus, writing a user subroutine becomes very essential.

In the previous Chapter, a piece-wised rate-dependent constitutive model has been developed and proved to be capable of predicting the material stress-strain response with acceptable accuracy. The purpose of this section is to come up with a robust and numerically effective user subroutine (VUMAT) to be implemented in the ABAQUS. Besides, considering the material does not carry significant anisotropy, especially at elevated temperatures, the von Mises yield criterion is selected as the yield function in order to reduce the code complexity without much compromise in accuracy.

4.1 Stress Integration Algorithms

In ABAQUS solver, the displacement formulation is applied and the simulation is strain driven in nature. That being said, the increment of strain is the known factor at the beginning of each time step and the stress tensor is calculated based on the material properties. In explicit solver, the strain increment ($\Delta\bar{\varepsilon}_{n+1}$) and saved history variable, such as stress state ($\Delta\sigma_n$) and plastic strain (ε_p), are provided in code at the beginning of time step while the element stress tensor needs to be updated at the end of each time step using the implemented constitutive model and yield function. Thus, the stress integration algorithm is the most crucial part of the VUMAT that has direct impact on model accuracy. Considering the model needs to be dealt with in this work is a piece-wised function, two stress integration algorithms will be selected for each part respectively.

It has been seen that the strain rate sensitivity of the material in the low temperature range, even slightly negative, actually approximates zero. That being said, the material can be reasonably assumed to be rate-independent for the temperature below the 150℃. For the classic elastoplastic material model, the return-mapping algorithms have been proved to the most numerically effective methods to integrate the stress tensor [116-120]. Most of the return-mapping algorithms can be classified into two categories: (1) the tangent cutting plane algorithm which adopts Euler forward scheme, and (2) the closet-point-projection algorithm which normally leads to non-linear equations and drags down the computational efficiency [121]. To save the computational cost, the cutting plane method is selected in this case. Figure 4-1 presents an geometrical interpretation of the cutting plane algorithm. Initially, the trial stress tensor ($\underset{\sim}{\sigma}_{n+1}^{trial}$) at the step n+1 is calculated based on the strain increment and historical stress. The obtained trial stress will be fed into yield function to check the yielding criterion. Once the trial stress is located outside of yield surface, the cutting plane algorithm using Newton method is activated to cut the stress back onto the yield surface.

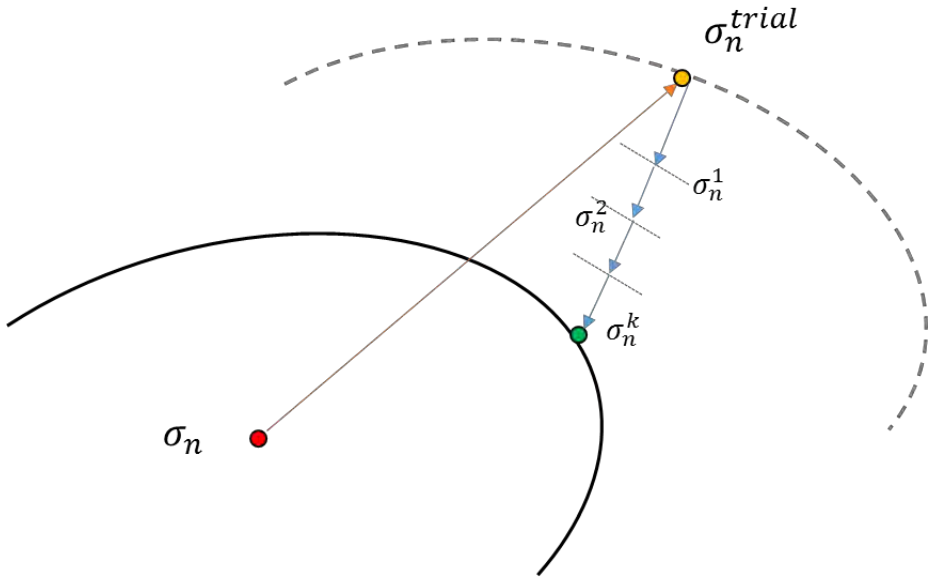

Figure 4-1: Geometrical schematic of the cutting plane algorithm.

Numerically, the procedure to calculate the stress using cutting plane algorithm can be expressed as following:

(i) Calculate trial stress:

$$\dot{\underset{\sim}{\varepsilon}}^{e}_{n+1} = \dot{\underset{\sim}{\varepsilon}}_{n+1} \tag{3.14}$$

$$\dot{\underset{\sim}{\sigma}} = \underset{\approx}{C} : \dot{\underset{\sim}{\varepsilon}}^{e}_{n+1} \tag{3.15}$$

$$\underset{\sim}{\sigma}^{trial}_{n+1} = \underset{\sim}{\sigma}_{n} + \underset{\approx}{C} : \dot{\underset{\sim}{\varepsilon}}_{n+1} \tag{3.16}$$

(ii) Check for yielding

$$\Phi = \bar{\sigma}_{n+1} - H(\bar{\varepsilon}^{p}_{n}, T) \tag{3.17}$$

$$\Phi \geq 0 \tag{3.18}$$

(iii) If NO, update the stress with trial stress:

$$\underset{\sim}{\sigma}_{n+1} = \underset{\sim}{\sigma}^{trial}_{n+1} \tag{3.19}$$

If YES, apply Newton method to cut back onto the yield surface

Set $i = 0$

Plastic Corrector
$$\dot{\lambda} = \frac{\Phi^{(i)}}{\frac{\partial \bar{\sigma}^{(i)}(\underset{\sim}{\sigma})}{\partial \underset{\sim}{\sigma}} : \underset{\approx}{C} : \frac{\partial \bar{\sigma}^{(i)}(\underset{\sim}{\sigma})}{\partial \underset{\sim}{\sigma}} - \frac{\partial H^{(i)}}{\partial \bar{\varepsilon}^{p}}} \tag{3.20}$$

Cutting Plane
$$\underset{\sim}{\sigma}_{n+1}^{(i+1)} = \underset{\sim}{\sigma}_{n+1}^{(i)} - \dot{\lambda}\left[\underset{\approx}{C} : \frac{\partial \bar{\sigma}^{(i)}(\underset{\sim}{\sigma})}{\partial \underset{\sim}{\sigma}}\right] \tag{3.21}$$

Plastic Strain Increment
$$\dot{\underset{\sim}{\varepsilon}}^{p(i+1)} = \dot{\lambda}\frac{\partial \Phi^{(i+1)}}{\partial \underset{\sim}{\sigma}} \tag{3.22}$$

Convergence Check
$$\bar{\sigma}_{n+1}^{(i+1)} - H(\bar{\varepsilon}_{n+1}^{p(i+1)}, T) \le \delta \tag{3.23}$$

where $\delta = 10^{-5}$

(iv) Diverge: Go to (iii)

Converge: Update the stress tensor and total plastic strain

$$\begin{aligned} \underset{\sim}{\sigma}_{n+1} &= \underset{\sim}{\sigma}_{n+1}^{(i+1)} \\ \bar{\varepsilon}_{n+1}^{p} &= \bar{\varepsilon}_{n+1}^{p(i+1)} \end{aligned} \tag{3.24}$$

The details of this calculation procedure and mathematical derivation can be referred to multiple publications [12, 95, 122].

As the temperature passes the 150℃, the effect of strain rate can no longer be ignored and the viscoplastic model steps in to describe the material behavior. As for the stress integration with rate-dependent model, the situation is completely different with classic elasto-plastic model. A number of different algorithms have been developed in literature [93, 123-126]. However, most of those algorithms are seen to be designed for the purpose of large time increment condition which complicates the implementation. In essence, the key factor in the case of rate-dependent model integration is to appropriately determine the time-dependent strain rate. Unlike the J_2-Plasticity, the radial return method

with backward Euler scheme is invalid due to the ignorance of the strain-rate effect. For rate-dependent stress integration, the strain rate should be calculated based on the stress state. In this study, the stress integration of rate-dependent model at high temperature range is accomplished using the simple explicit scheme. In the beginning of the time step, the trial stress (σ_n^{trial}) is determined the same with radial return map method. Once the yielding condition is determined, the strain rate, which can be taken as the increment of the plastic strain over the time step, will be directly calculated using the trail stress. Recall the Eq. (3.4), the relationship between the strain rate and stress can be obtained by linearizing the equation:

$$\dot{\varepsilon}^p_{n+1} = f(\bar{\sigma}_{n+1}, \omega) \tag{3.25}$$

where ω represents the internal variables of the equation. Moreover, it clearly explains the necessity of using Eq. (3.4) instead of Eq. (3.1): it is impractical to achieve the linearization form of Eq. (3.1). With the strain rate $\dot{\varepsilon}_p$, the increment of plastic strain over this time step can be obtained by

$$\Delta\varepsilon^p{}_{n+1} = \dot{\varepsilon}^p_{n+1} \cdot \Delta t \tag{3.26}$$

Knowing the plastic strain, strain rate and temperature, the effective stress can be updated with hardening rule. After that, the stress tensor can be updates in the same way with that for elasto-plasticity model:

$$\underset{\sim}{\sigma}^{(i+1)}_{n+1} = \underset{\sim}{\sigma}^{(i)}_{n+1} - \dot{\varepsilon}^p_{n+1}\left[\underset{\approx}{C} : \frac{\partial \bar{\sigma}^{(i)}(\underset{\sim}{\sigma})}{\partial \underset{\sim}{\sigma}}\right] \tag{3.27}$$

This proposed stress integration scheme has been coded in FORTRAN and successfully implemented in ABAQUS\Explicit. The cutting plane method for rate-

independent model is very stable and accurate. The only drawback with the explicit method for rate-dependent model is the limit on the size of time increment. Based on the single element simulation, the optimum acceptable time increment is under 10^{-4}s without losing much model accuracy.

CHAPTER 5: NON-ISOTHERMAL TENSILE TESTING AND EXPERIMENTAL VALIDATION

To complete this research delivery, a real non-isothermal forming process has to be carried out in lab. The purpose of this testing is to verify the feasibility of HB-CD as well as validate FEA simulations with experimental results. Obviously, a real hot stamping process is preferred in this case. However, building up a reliable stamping set-up in lab is unaffordable at this time. Meanwhile, the hot stamping processing is sensitive to a lot of parameters such as temperature, friction and cooling rate. Considering the focus for the current stage is to study the material deformation under the non-isothermal condition, it is suggested to simplify the testing approach and eliminate the irrelevant factors. Hence, a new tensile testing method, referred as non-isothermal tensile testing, is proposed here. The obtained the experimental results, which is displacement-load curve, will be compared to the FEA simulations to validate the developed material model and user subroutine (VUMAT).

5.1 Non-Isothermal Tensile Testing

5.1.1 Experimental set-up

The general purpose of non-isothermal tensile testing is to examine the material deformation under the continuous cooling condition. Therefore, the experiment set-up needs to be able to effectively control the cooling rate. Meanwhile, the temperature and strain measurements are critically important as well for the post analysis. Conventionally,

the true strain during tensile testing could be extracted from strain gauge or extensometer. However, those measurement techniques are only able to provide either point-to-point (extensometer) or local (strain gauge) information. Considering the potential post uniform deformation, it is particularly essential to take the entire gauge area into account for the testing at elevated temperatures. As the state-of-the-art non-contact strain measurement technique, digital image correlation (DIC) reveals high-level of details about material deformation with full-filed and multi-axis measurements that cannot be matched by any of the predecessor conventional techniques. Using DIC system enables to generate accurate stress-strain curves as well as the informative strain maps reflecting much local deformation condition. On the other hand, the similar situation has been come across for the temperature measurement. In order to fully couple the mechanical deformation with temperature evolution, the temperature map, equivalent to the strain map, is needed instead of a point measurement done by thermocouple. Therefore, an infrared thermal camera that can capture the temperature distribution over the specimen is applied in this case.

In this study, the convection furnace is not applicable as the heating source because the closed chamber is impractical to apply a cooling system and observe the specimen with thermal/DIC camera. On the other hand, induction heater has relatively lower efficiency with aluminum and the inappropriate coil design can block the view of cameras as well. In consideration of the convenience of rapid heating and cooling control, a joule heating system is applied on a hydraulic INSTRON 1332 machine. More importantly, this setup is suitable for the observation with optical techniques since the specimen is completely exposed to the air during the testing. A digital image correlation (DIC) system, ARAMIS

5M, and FLIR infrared thermal camera, A40 with resolution of 320×240, are utilized to capture the evolution of temperature and strain distribution simultaneously.

As-received material, AA5182-O, is machined into the specimens according to ASTM E8 standard geometry with 12.7mm gauge width but wider gripping area, as it is seen in Figure 5-1 (b), which is designed for quick-mount and better contact with grips. As it is shown in Figure 5-1 (a), a 600 to 700A direct current, depends on target temperature, is generated by a DC power supply and applied to flow through the specimen. With DIC and thermal camera sitting in the front and back, material deformation can be captured as well as temperature distribution. To enable the DIC measurements, the front surface of the gauge area is slightly polished, cleaned, and then speckle-patterned with high temperature black/white paints as it is demonstrated in ssssss(b). The back surface is painted in plain black, also with high temperature paint, so as to eliminate the noises during the recording of thermal camera. The experiment starts with heating the specimen while monitoring the temperature over gauge area with thermal camera. Once the target temperature is achieved and temperature distribution is seen to be uniform in the image from thermal camera, current will be cut off and immediately start INSTRON machine pulling the specimen. Meanwhile, the DIC and thermal camera are triggered simultaneously to record images at decent frame rates. Hence, the hot specimen will be deformed in the ambient air which exerts convection heat transfer to cool down the specimen. If necessary, an external air diffusor is optional to increase the cooling rate with forced air blowing. Overall, the strain map and temperature distribution could be extracted from DIC and thermal camera to reflect the material deformation subject to the non-isothermal tensile testing.

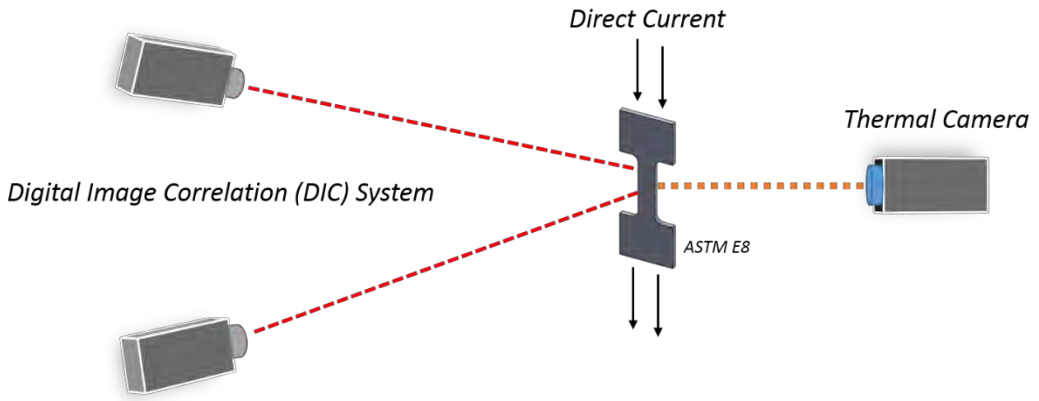

(a)

(b)

Figure 5-1: (a) Schematic of the experiment set-up of the electrically assisted non-isothermal tensile testing. (b) The photo of the specimens with speckle-patterned front surface and back surface in plain black.

5.1.2 Analysis: coupled thermal-mechanical measurement

The non-isothermal tensile testing could be operated at various starting temperatures and test speeds. As an example of results analysis, an experiment is performed with initial temperature of 250℃ and constant crosshead speed of 1mm/s. In the first place, the raw data exported from thermal camera is processed with Matlab so that the field of view is tailored and only the gauge area is shown. In Figure 5-2 (a), eight selected frames with equal time interval are presented, in 3D view with temperature as the z-axis, to illustrate the evolution of temperature distribution, from the beginning of experiment until the failure is firstly detected. Evidently, the temperature distribution is non-uniform on the gauge area during the whole process, especially at the initial stage. By the time the experiment starts, the current is cut off so the heat generation stops. Since the two grips that clamp the specimen are at lower temperature, they keep sucking the heat from two ends of gauge and cause the center area of the specimen has relatively higher temperature.

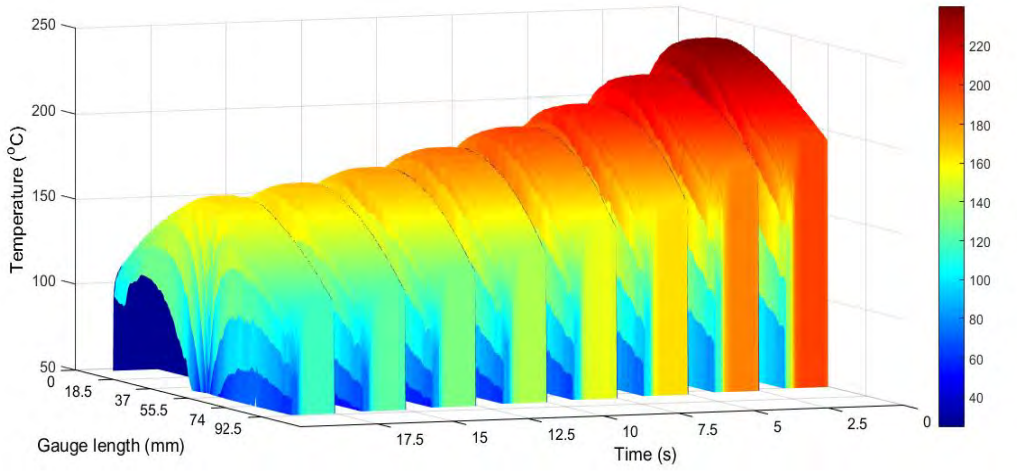

Figure 5-2: The selected temperature profiles recorded by thermal camera of the specimen gauge area during the non-isothermal tensile testing with equal time interval.

Having seen the non-uniform temperature distribution, it is irrational to take the entire gauge area into consideration, especially for the stress-strain curve evaluation. However, after close examine the thermal images, it is found that, the center area of the specimen is showing relatively higher but also more uniform temperature because this area is less sensitive to the heat dissipation from the specimen to grips. Figure 5-3 presents the same selected frames as Figure 5-2 but in a different perspective view, and each frame has a small area highlighted with white dot square. Obviously, this area of interest should move as well as expand with the deformation of material. Therefore, it is necessary to trace this moving boundary and take both strain and temperature measurements during the process. To accomplish this task, following steps are taken:

1. Examine the last thermal image before the specimen fails, and manually identify an area around the center, as large as possible, that has less deviation in temperature.
2. Select the same small area in corresponding DIC strain map. With aid of DIC, the boundary of this small area can be traced back to the first image, then the expansion speed of upper/lower limit of the boundary is extracted.
3. Import the speed of upper/lower limit of boundary into a Matlab code which automatically extract the temperature information of the moving boundary.

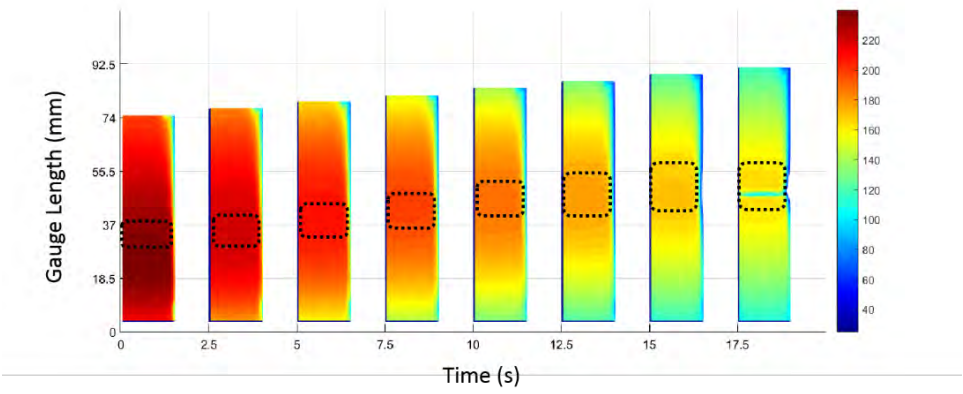

(a)

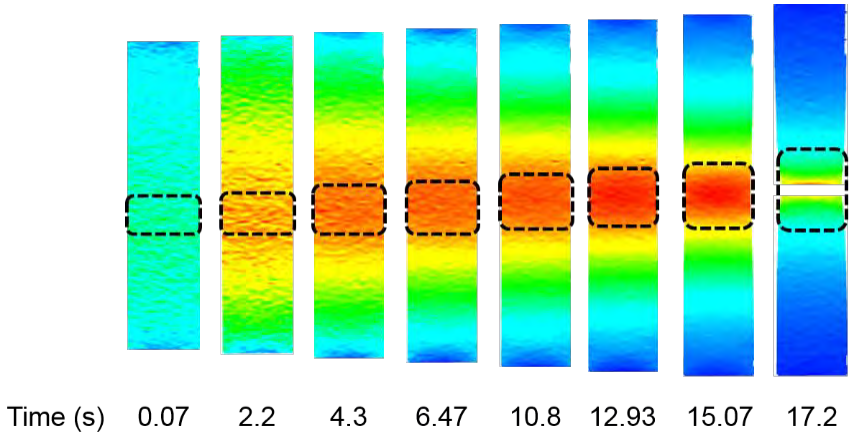

(b)

Figure 5-3: The area highlighted with whited dot rectangle in (a) is showing the relatively uniform temperature distribution.

Hence, thermal images are reprocessed so as to zoom in and present the temperature profile of the moving boundary as it is seen in Figure 5-4. Compared to the entire gauge area, the identified small area apparently has more uniform temperature distribution during the cooling. To quantify the temperature measurement, standard deviation is derived based

on the total data points inside of the boundary. According to the plot in Figure 5-5, the maximum standard deviation of the temperature is below 5℃ until the excessive diffuse necking and failure take place at the end of testing.

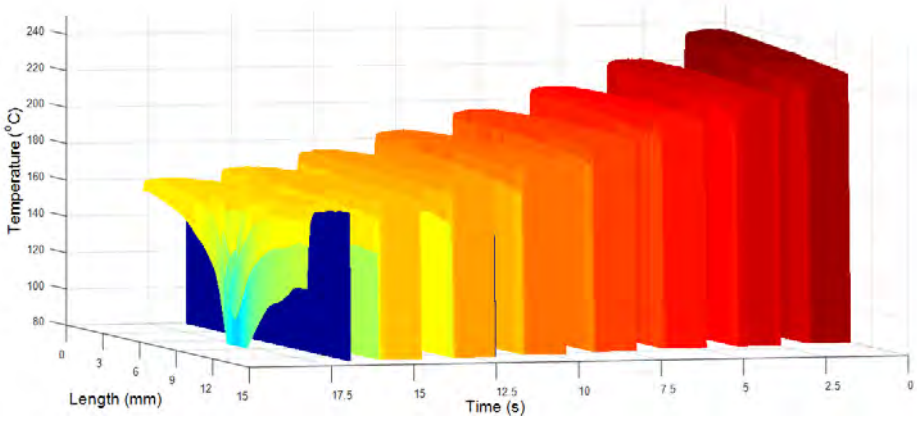

Figure 5-4: Temperature profile of the moving boundary during the non-isothermal tensile testing.

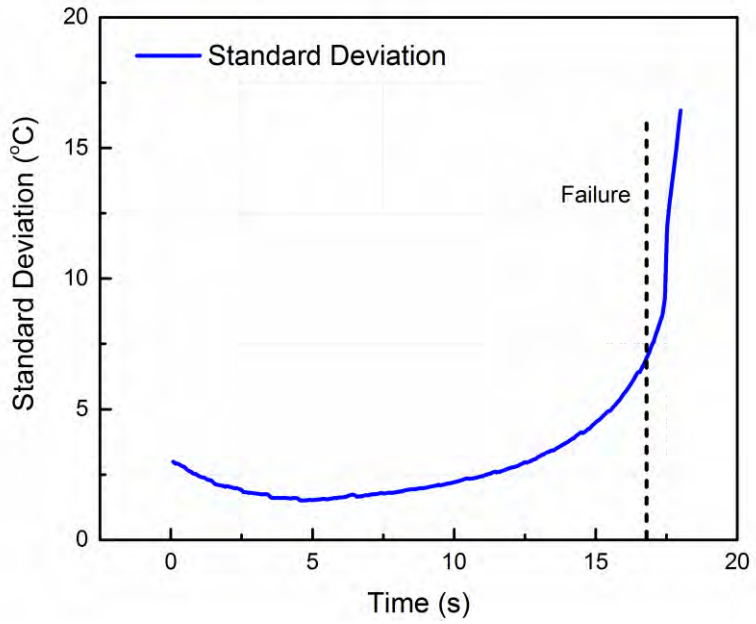

Figure 5-5: Standard deviation of temperature over the selected small area during non-isothermal tensile testing.

Figure 5-6 includes the plots of the average temperatures of the small and gauge area during the non-isothermal testing. Temperatures measured from small area is seen to be globally higher than that from the entire gauge area. Additionally, the average temperature derived here will be used as the temperature input to the constitutive model.

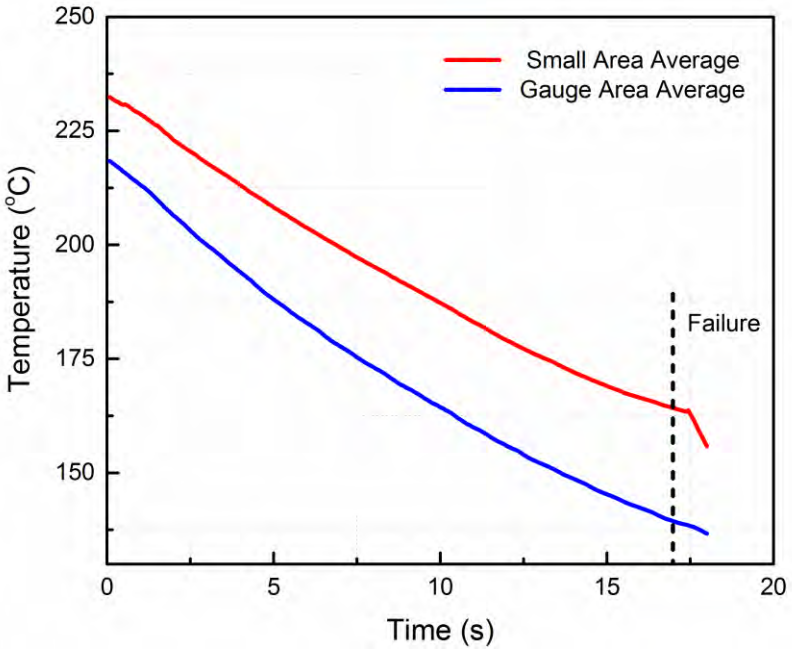

Figure 5-6: The average temperature of the small and gauge during the non-isothermal testing process.

The strain measurement in DIC is actually an average strain over a pre-selected area. In this case, two sets of true stress-strain curves which are separately evaluated over different area selection: the gauge area which is consistent with the normal evaluation of

tensile testing, and small area as defined above (See Figure 5-7). Obtained true stress-strain curves are presented in Figure 5-8(a).

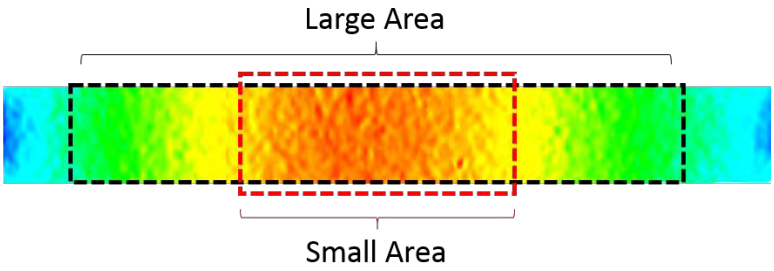

Figure 5-7: Area selection in DIC analysis in ARAMIS.

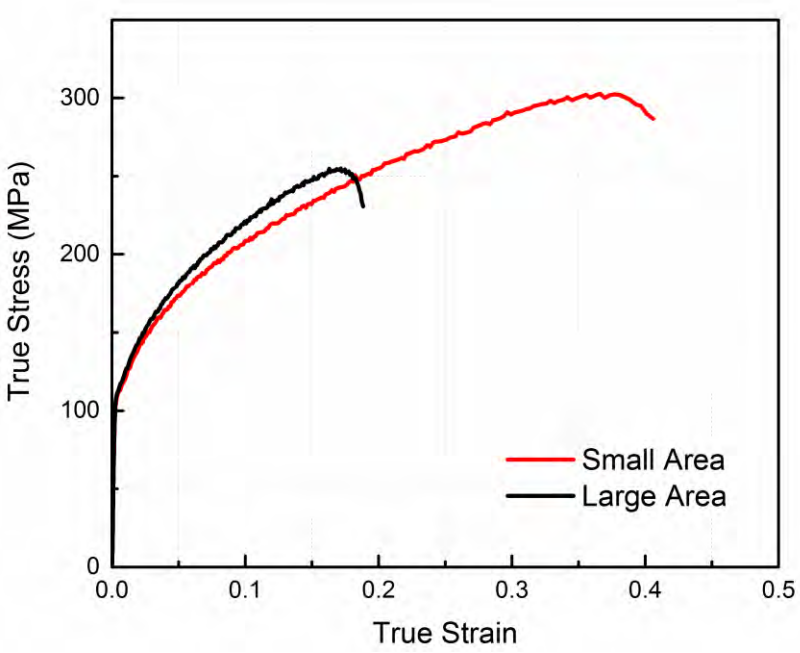

(a)

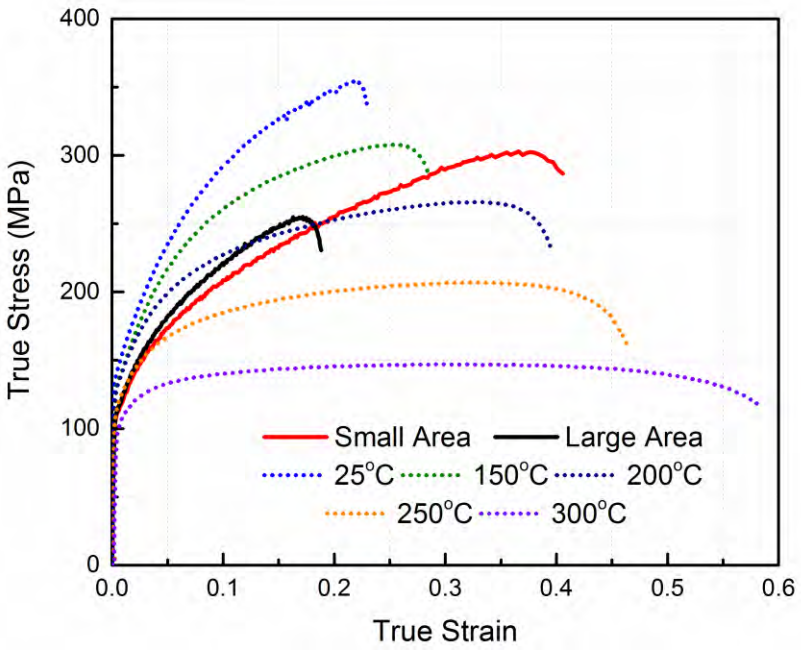

(b)

Figure 5-8: (a) The stress-strain curves evaluated based on large and small area selection in non-isothermal tensile testing. (b) The comparison of the stress-strain curves between the isothermal (solid) and non-isothermal (dot) tensile testing.

With non-uniform temperature distribution in large area, the stain averaged over the entire gauge area (large area) is very limited. However, the selected small area with relatively more uniform temperature distribution generates a stress-strain curve showing larger plastic strain.

Figure 5-8 plot the stress-strain curves for both non-isothermal and isothermal tensile testing which covers from ambient temperature to 300℃. As it is seen in the figure, the material under non-isothermal forming condition produces more ductility than the isothermal testing at 25℃, 100℃, and 100℃, and approximated the ultimate plastic strain

in 200℃ testing. Comparing to the stress-curve at 250℃ which is the starting temperature of the non-isothermal testing, the result from non-isothermal testing still shows a considerable amount of ductility. More importantly, the non-isothermal curve presents strong "hardening" behavior which is favored in most cases for sheet metal forming.

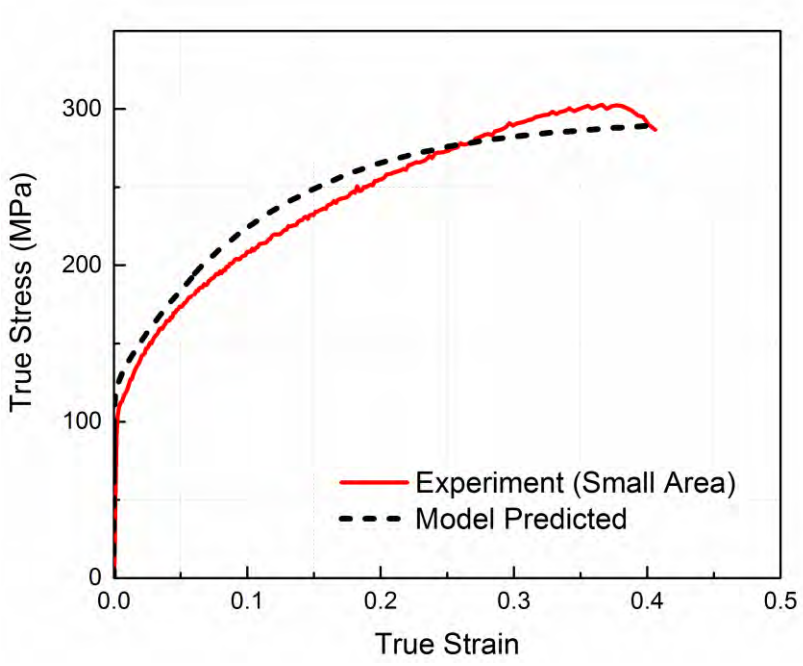

Figure 5-9: The comparison of the stress-strain curves from the experiment and model prediction for non-isothermal tensile testing.

5.2.2 Coupled Thermal-Mechanical FE Simulations

A FEA model has been set-up in ABAQUS\Explicit to simulate the non-isothermal forming process described in Section 5.1.1. The pre-processing requires appropriate heat transfer coefficients as the input parameters. Obviously, a considerable amount of heat dissipates via the heat conduction between the grips and specimen. Meanwhile, the heat convection also takes the heat directly from the gauge area into the environment. Therefore, it is necessary to calibrate the coefficients for conductance and convection in order to obtain the correct temperature distribution over the entire process. To simplify the model, a rectangular in the size of 72×12mm, which is the same with actual gauge area, has been created with 3D mesh element in ABAQUS\Explicit. The element size has been set to 1 and the number of thickness integration points has been set to 10. In this model, a heat transfer analysis is performed in the first place without mechanical deformation just to validate the parameters. The input mechanical and thermal properties of the material have been listed in Table 4. After calibration with obtained thermal camera images, the heat conduction is represented by applying a surface heat flux of -550 at top and bottom edges of specimen. A surface film condition interaction has been applied to the entire specimen to simulate the heat convection effect. The film coefficient is set to be 0.2, and the sink temperature equals 10℃. An initial temperature of 250℃ has been assigned to the entire specimen. Figure 5-10 demonstrates the model set-up for the heat transfer analysis.

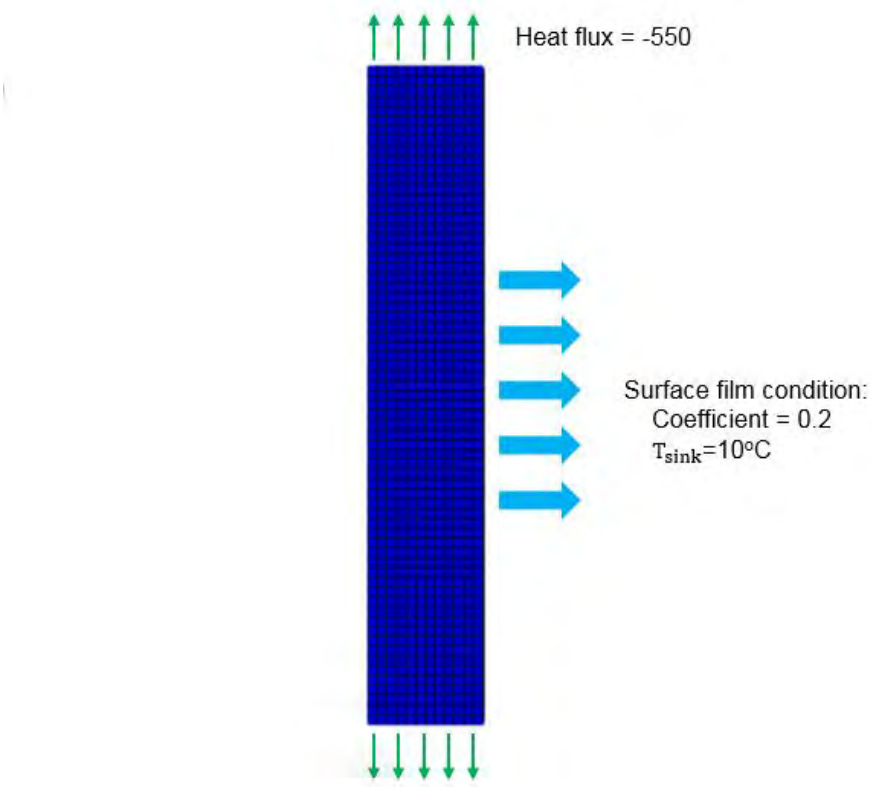

Figure 5-10: Model set-up for heat transfer analysis to simulate the temperature distribution of non-isothermal tensile testing.

Table 4: Mechanical and thermal properties of AA5182-O in ABAQUS/Explicit

Material	Density (g/cm^3)	Poisson Ratio	Young's modulus (GPa)	Specific Heat (J/g·°C)	Thermal Conductivity (W/m·K)
Blank (AA5182-O)	2.65	0.33	69.6	0.904	150

The result of heat transfer analysis has been compared with the thermal camera measurement by extracting the nodal temperatures on the line in the center of the specimen. Since it is technically impossible to present a video clip here, a plot of the temperature

distribution at time step of 5 second has been shown in Figure 5-11. As it is seen in figure, the FE simulation result shows an acceptable correlation with the experimental results. Overall, the heat transfer analysis in ABAQUS is capable of capturing the evolving temperature distribution over the entire process. Thus, this set of thermal properties will be used for a fully coupled thermal-mechanical simulation.

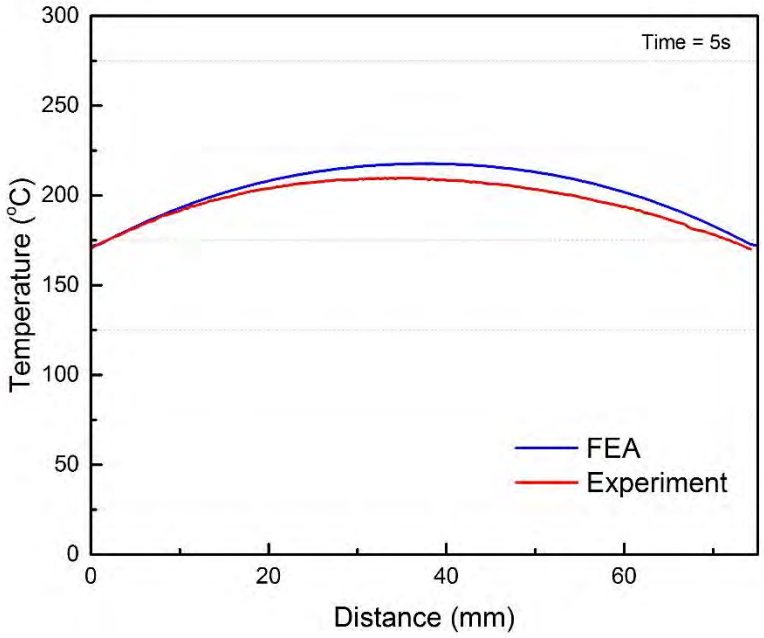

Figure 5-11: The temperature distributions in the center line of the specimen in FEA simulation and thermal camera measurement.

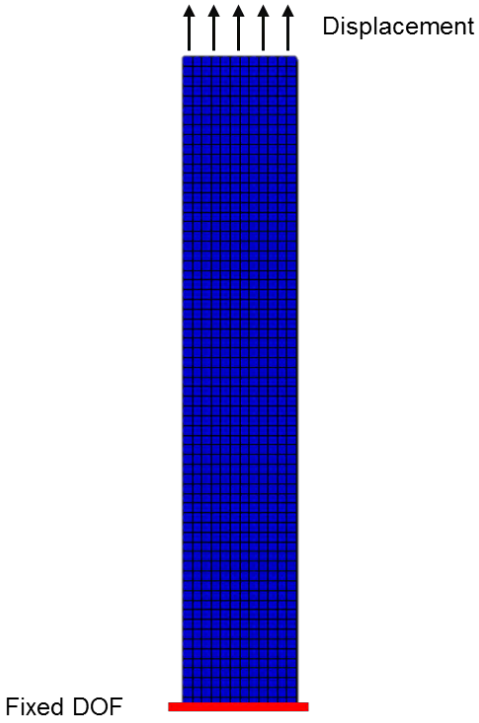

Figure 5-12: The boundary condition for mechanical analysis of non-isothermal tensile testing.

The coupled thermal-mechanical simulation is set-up as it is presented in Figure 5-12. The lower edge of the specimen has been fixed in all degrees of freedom while the upper edge is assigned with a total displacement of 14mm controlled by a tabular of time-amplitude which correlates with the actual movement of the upper grip in experiment. the total step time is 18 second. A scaling factor of 15 has been selected to reduce the computational time without much exaggeration in simulation results.

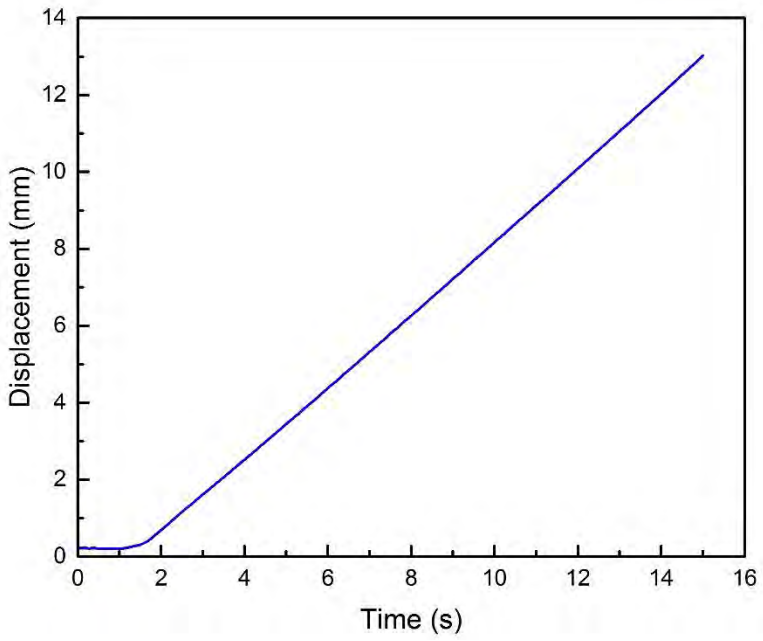

Figure 5-13: The boundary condition of the upper edge of specimen in FEA model.

The simulation successfully completes for 16s until the excessive distortion of element detected. Figure 5-14 briefly presents the simulated non-isothermal deformation process by showing the snapshots of the temperature (left) and strain (right) fields at 1s, 5s, 10s, and 15s. The simulation is capable of capturing the material deformation until the excessive strain localization.

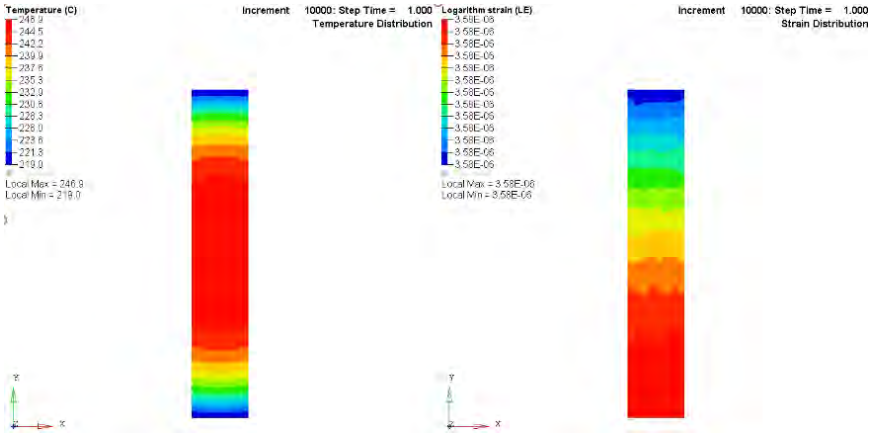
Temperature (C)
248.9
244.5
242.2
239.9
237.6
235.3
232.9
230.6
228.3
226.0
223.6
221.3
219.0
Local Max = 246.9
Local Min = 219.0
Increment 10000: Step Time = 1.000
Temperature Distribution
Logarithm strain (LE)
3.58E-06
3.58E-06
3.58E-06
3.58E-06
3.58E-06
3.58E-06
3.58E-06
3.58E-06
3.58E-06
3.58E-06
3.58E-06
3.58E-06
3.58E-06
Local Max = 3.58E-06
Local Min = 3.58E-06
Increment 10000: Step Time = 1.000
Strain Distribution

(a)

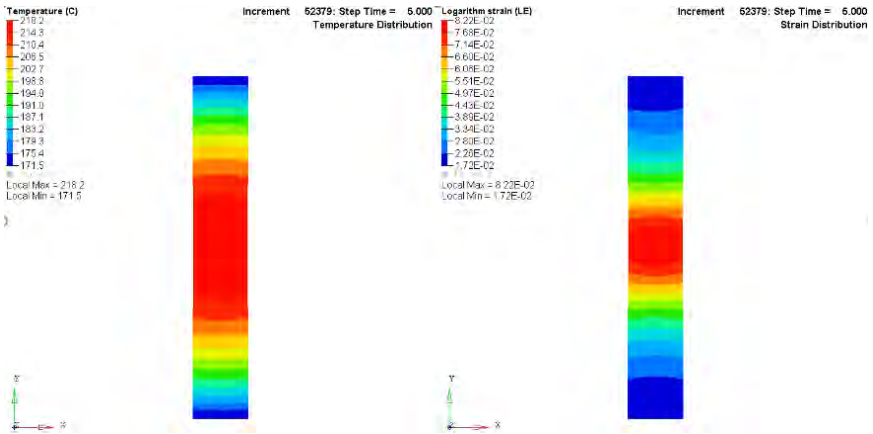
Temperature (C)
218.2
214.3
210.4
206.5
202.7
198.8
194.9
191.0
187.1
183.2
179.3
175.4
171.5
Local Max = 218.2
Local Min = 171.5
Increment 52379: Step Time = 5.000
Temperature Distribution
Logarithm strain (LE)
8.22E-02
7.68E-02
7.14E-02
6.60E-02
6.06E-02
5.51E-02
4.97E-02
4.43E-02
3.89E-02
3.34E-02
2.80E-02
2.26E-02
1.72E-02
Local Max = 8.22E-02
Local Min = 1.72E-02
Increment 52379: Step Time = 5.000
Strain Distribution

(b)

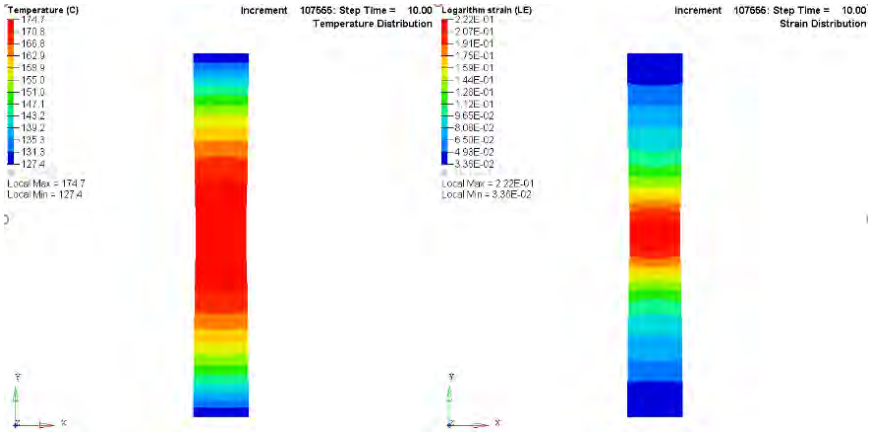
Temperature (C)
174.7
170.8
166.8
162.9
158.9
155.0
151.0
147.1
143.2
139.2
135.3
131.3
127.4
Local Max = 174.7
Local Min = 127.4
Increment 107655: Step Time = 10.00
Temperature Distribution
Logarithm strain (LE)
2.22E-01
2.07E-01
1.91E-01
1.75E-01
1.59E-01
1.44E-01
1.28E-01
1.12E-01
9.65E-02
8.08E-02
6.50E-02
4.93E-02
3.36E-02
Local Max = 2.22E-01
Local Min = 3.36E-02
Increment 107655: Step Time = 10.00
Strain Distribution

(c)

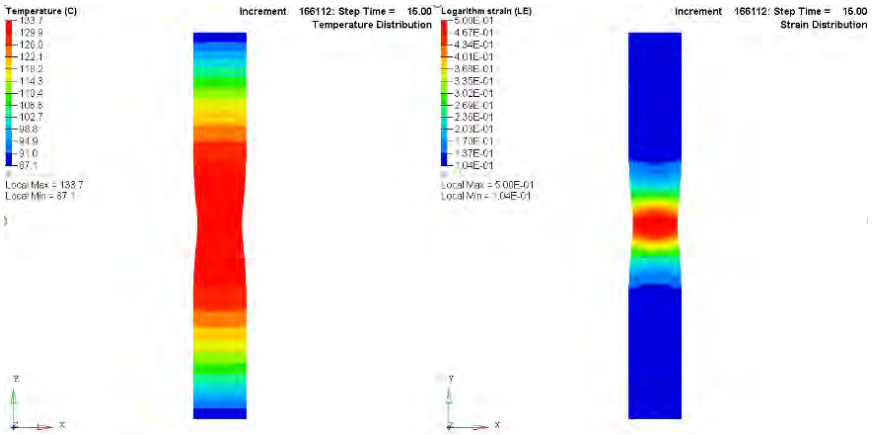

(d)

Figure 5-14: The simulated deformation process of AA5182-O during non-isothermal tensile testing at (a) 1s, (b) 5s, (c) 10s, and (d) 15s.

The grip load, which is the sum of the reaction force on all the nodes at the upper edge, has been extracted along with the displacement of the edge to generate the FEA displacement-load curve. Figure 5-15 compares the displacement-load curves from FEA simulation and the experimental result. A good correlation is seen, especially in the plastic deformation region, between the FEA and experiment.

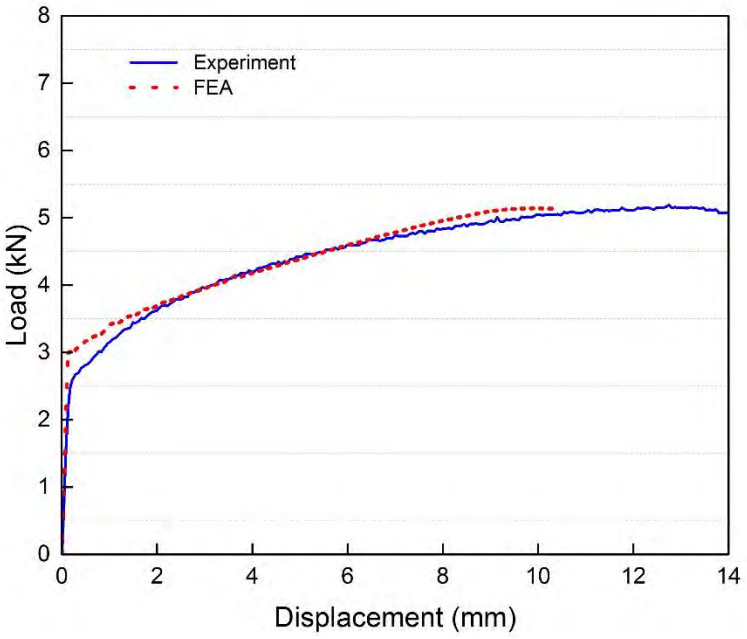

Figure 5-15: Comparison of the load-displacement curves between the experimental result and FEA simulation.

CHAPTER 6: SUMMARY AND CONCLUSION

6.1 Concluding Remarks

In the Chapter 1, a critical literature review was firstly given on the current mainstream techniques for warm/hot forming with aluminum alloy sheets in automotive industry. The poor material formability at low temperatures and considerable energy cost at hot temperatures prevent the application of aluminum alloy sheets in mass production for automotive sector, especially for the manufacture of economy cars. Consequently, a new hot stamping approach, which is referred as HB-CD, has been proposed trying to merge the merits of cold and hot forming and propelling the wide application of aluminum alloy sheets in automotive industry. Ultimately, the HB-CD is expected to produce a relatively complex shape parts with aluminum alloy sheets while still maintaining an affordable energy and labor cost. The practicality and feasibility of HB-CD have been proved in several publications with presents of successful stamping part. This research focuses on conducting a comprehensive study on non-isothermal forming process with aluminum alloy sheets, from material properties characterization to modeling and finite element analysis. Moreover, a robust research approach has been established for the future investigation of HB-CD with more flexible experiment conditions, such as different material selection and wider temperature range.

In Chapter 2, the material properties of as-received AA5182-O, which is one of the most popular commercial grade aluminum alloys in automotive industry, have been characterized using isothermal tensile testing at a wide range of temperature and strain-rate

with aids of Digital Image Correlation (DIC). The true stress-strain curves extracted using DIC shows that the material ductility can be significantly enhanced with elevating the temperature above 200℃. At the warm temperatures, the flow stress is noticed to decline with increasing temperature and decreasing strain rate. Material anisotropy has been evaluated by presenting the evolving yield stresses and Lankford coefficients (r-value) with environment temperatures. The material still carries anisotropic properties, even not much, at 300℃. Moreover, thermally activated deformation mechanisms, dynamic strain ageing and dislocation climb, have been identified in different temperature ranges. The balanced biaxial testing was performed using hydraulic bulge test with DIC to capture and analyze the out-of-plane deformation. The strain path on the apex is considered to be linear which ensure the assumption of isotropic material is valid in order to calculate the effective stress. The derived effective stress-strain curve from bulge test is found to be identical with that from uniaxial tensile testing, except the extended maximum attainable plastic strain.

As the most crucial receipt for predictive FE simulation, the material modeling has been investigated in this work as presented in Chapter 3. Two new temperature- and strain-rate- dependent piece-wised constitutive models have been developed, and both are capable of describing the stress-strain behavior of material in a wide range of experimental conditions. To account for the anisotropic properties, the eight parameters of in-plane anisotropic yield function, Yld2000-2d, have been calibrated by solving eight non-linear equations with experimental results obtained in Chapter 2. The obtained parameters are found to be dependent on temperature and thus fitted into temperature-dependent functions. The plot of evolving yield surfaces at different temperatures exhibits the material

approaching to isotropy with increasing temperature. To evaluate the material formability at different temperatures, the strain-based and stress-based forming limit diagrams (FLD) are constructed by the theoretical calculation of M-K model.

In Chapter 4, the stress integration strategy for this study has been discussed. Considering the material properties is described in a piece-wise function, the stress tensor calculations are handled respectively. An implicit algorithm, referred as radial map return, has been used for the low temperature range where the rate sensitivity of material can be reasonably ignored. A simple explicit algorithm is selected for high temperature range since the material becomes critically dependent on strain rate. The developed material model with stress integration algorithm have been coded in the form of user subroutine (VUMAT) for ABAQUS/Explicit implementation.

To finalize the entire project, a non-isothermal tensile testing has been invented and performed in the lab to prove the feasibility of HB-CD and validate the FEA simulations, especially for the implemented user subroutine (VUMAT). The heat transfer coefficients are calibrated with thermal camera measurements. The experimental results from DIC and infrared thermal camera measurements can be coupled and correlated to reveal the material deformation under continuous cooling condition. After that, a thermo-mechanical coupled finite element simulation implemented with the VUMAT has been carried out. The heat transfer coefficients are calibrated with experimental thermal measurements. The comparison of the displacement-load curves between the FEA simulation and experiment illustrates a decent correlation which gives much confidence of applying the developed VUMAT in a more complicated hot stamping simulation.

6.2 Recommendations for the Future Work

The current study mainly concentrates on establishing a general research approach, from material characterization to finite element simulations, for the HB-CD process with aluminum alloy sheets. Eventually, this task has been completed by performing a non-isothermal tensile testing with FEA validation using AA5182-O. However, some of the research gaps are still existing and need to be investigated in the future so as to propel the further development and application of HB-CD.

In the first place, although challenging, it is imperative and necessary to build a hot stamping set-up to conduct a real HB-CD process in the lab. Despite having seen a promising future and good FEA correlation in non-isothermal tensile testing, the real stamping is still the only way to validate the developed yield function and forming limit diagrams under the non-isothermal forming condition. Moreover, with a real stamping set-up, it becomes possible to directly compare the deformed parts out of cold stamping, HB-CD, and conventional isothermal hot stamping. The part produced by HB-CD is expected to be more deformable than that from cold stamping, but significantly reduce the total process duration and consumed energy than hot stamping.

In this thesis, the material formability at elevated temperatures is currently evaluated by the theoretical calculation using M-K model. However, performing a formability tests at elevated temperature is actually a more reliable and straightforward method to quantify the material formability. It is suggested to build a formability test set-up that can heat up and maintain the entire tool sets at a desired temperature to carry out the formability test. Considering the advantages of using digital image correlation in

mechanical testing, it is highly recommended to integrate the DIC during the high temperature formability tests.

The user subroutine developed in this thesis select a simple explicit integration algorithm for the rate-dependent constitutive model at high temperatures. However, the mass scaling factor and maximum time increment still need to be carefully selected, especially in a large scale sheet forming study, to reduce computational time without losing prediction accuracy. It prompts to exploit a more robust and unconditionally stable stress integration algorithms which is suitable for large time step.

REFERENCES

1. Taub, A., et al., *The evolution of technology for materials processing over the last 50 years: The automotive example.* JOM, 2007. **59**(2): p. 48-57.

2. Wen, W. and J.G. Morris, *An investigation of serrated yielding in 5000 series aluminum alloys.* Materials Science and Engineering: A, 2003. **354**(1–2): p. 279-285.

3. Ozturk, F., H. Pekel, and H. Halkaci, *The Effect of Strain-Rate Sensitivity on Formability of AA 5754-O at Cold and Warm Temperatures.* Journal of Materials Engineering and Performance, 2011. **20**(1): p. 77-81.

4. Picu, R.C., *A mechanism for the negative strain-rate sensitivity of dilute solid solutions.* Acta Materialia, 2004. **52**(12): p. 3447-3458.

5. Taleff, E., P. Nevland, and P. Krajewski, *Tensile ductility of several commercial aluminum alloys at elevated temperatures.* Metallurgical and Materials Transactions A, 2001. **32**(5): p. 1119-1130.

6. Taleff, E., et al., *Warm-temperature tensile ductility in Al-Mg alloys.* Metallurgical and Materials Transactions A, 1998. **29**(3): p. 1081-1091.

7. Kulas, M.-A., et al., *Deformation mechanisms in superplastic AA5083 materials.* Metallurgical and Materials Transactions A, 2005. **36**(5): p. 1249-1261.

8. Abu-Farha, F., *The development of a forming limit surface for 5083 aluminum alloy sheet.* JOM Journal of the Minerals, Metals and Materials Society, 2011. **63**(11): p. 72-78.

9. Rashid, M.S., et al., *Quick plastic forming of aluminum alloy sheet metal*. 2001, Google Patents.

10. Krajewski, P. and J. Schroth, *Overview of Quick Plastic Forming Technilogy.* Materials Science Forum, 2007. **551-552**: p. 3-12.

11. Li, D. and A.K. Ghosh, *Biaxial warm forming behavior of aluminum sheet alloys.* Journal of Materials Processing Technology, 2004. **145**(3): p. 281-293.

12. Abedrabbo, N., F. Pourboghrat, and J. Carsley, *Forming of AA5182-O and AA5754-O at elevated temperatures using coupled thermo-mechanical finite element models.* International Journal of Plasticity, 2007. **23**(5): p. 841-875.

13. Ayres, R. and M. Wenner, *Strain and strain-rate hardening effects in punch stretching of 5182-0 aluminum at elevated temperatures.* Metallurgical Transactions A, 1979. **10**(1): p. 41-46.

14. Mahabunphachai, S. and M. Koç, *Investigations on forming of aluminum 5052 and 6061 sheet alloys at warm temperatures.* Materials & Design, 2010. **31**(5): p. 2422-2434.

15. Kim, B.J., et al., *Finite element analysis and experimental confirmation of warm hydroforming process for aluminum alloy.* Journal of Materials Processing Technology, 2007. **187–188**: p. 296-299.

16. Yuan, S., J. Qi, and Z. He, *An experimental investigation into the formability of hydroforming 5A02 Al-tubes at elevated temperature.* Journal of Materials Processing Technology, 2006. **177**(1–3): p. 680-683.

17. Jain, M., J. Allin, and M.J. Bull, *Deep drawing characteristics of automotive aluminum alloys.* Materials Science and Engineering: A, 1998. **256**(1–2): p. 69-82.

18. Bay, N., *Cold forming of aluminium—state of the art.* Journal of Materials Processing Technology, 1997. **71**(1): p. 76-90.

19. Panicker, S., et al., *Characterization of Tensile Properties, Limiting Strains, and Deep Drawing Behavior of AA5754-H22 Sheet at Elevated Temperature.* Journal of Materials Engineering and Performance, 2015: p. 1-16.

20. Cvitanić, V., D. Ivandić, and B. Lela, *Comparison of orthotropic constitutive models in predicting square cup deep drawing process of AA2090-T3 sheet.* Mechanical Technologies and Structural Materials, 2014.

21. Ghavam, K., R. Bagheriasl, and M.J. Worswick, *Analysis of Nonisothermal Deep Drawing of Aluminum Alloy Sheet With Induced Anisotropy and Rate Sensitivity at Elevated Temperatures.* Journal of Manufacturing Science and Engineering, 2013. **136**(1): p. 011006-011006.

22. Takuda, H., et al., *Finite element simulation of warm deep drawing of aluminium alloy sheet when accounting for heat conduction.* Journal of Materials Processing Technology, 2002. **120**(1–3): p. 412-418.

23. Naka, T. and F. Yoshida, *Deep drawability of type 5083 aluminium–magnesium alloy sheet under various conditions of temperature and forming speed.* Journal of Materials Processing Technology, 1999. **89–90**(0): p. 19-23.

24. Kim, H.S., M. Koç, and J. Ni, *Development of an analytical model for warm deep drawing of aluminum alloys.* Journal of Materials Processing Technology, 2008. **197**(1–3): p. 393-407.

25. Cetin, M.H., et al., *Development of Forming Temperature Curves for Warm Deep Drawing Process Under Non-isothermal Conditions.* Arabian Journal for Science and Engineering, 2015: p. 1-22.

26. El-Morsy, A.-W. and K.-I. Manabe, *Finite element analysis of magnesium AZ31 alloy sheet in warm deep-drawing process considering heat transfer effect.* Materials Letters, 2006. **60**(15): p. 1866-1870.

27. Bariani, P.F., et al., *Hot stamping of AA5083 aluminium alloy sheets.* CIRP Annals - Manufacturing Technology, 2013(0).

28. Harrison, N.R. and S.G. Luckey, *Hot Stamping of a B-Pillar Outer from High Strength Aluminum Sheet AA7075*. 2014, SAE Technical Paper.

29. Choi, J.P., et al., *Process Development for Stamping A‐Pillar Covers with Aluminum.* Light Metals 2015, 2015: p. 195-201.

30. Sutton, M.A., J.J. Orteu, and H. Schreier, *Image correlation for shape, motion and deformation measurements: basic concepts, theory and applications*. 2009: Springer Science & Business Media.

31. Sutton, M.A., et al., *Determination of displacements using an improved digital correlation method.* Image and Vision Computing, 1983. **1**(3): p. 133-139.

32. Peters, W. and W. Ranson, *Digital imaging techniques in experimental stress analysis.* Optical engineering, 1982. **21**(3): p. 213427-213427-.

33. Luo, P., et al., *Accurate measurement of three-dimensional deformations in deformable and rigid bodies using computer vision.* Experimental Mechanics, 1993. **33**(2): p. 123-132.

34. Tung, S.H., et al., *Using the Simplified 3D DIC Method to Measure the Deformation of 3D Surface.* Applied Mechanics and Materials, 2011. **121-126**: p. 3945.

35. Hu, Z., et al., *Error evaluation technique for three-dimensional digital image correlation.* Applied Optics, 2011. **50**(33): p. 6239-6247.

36. Neggers, J., et al., *A Global Digital Image Correlation Enhanced Full-Field Bulge Test Method.* Procedia IUTAM, 2012. **4**(0): p. 73-81.

37. Wattrisse, B., et al., *Analysis of strain localization during tensile tests by digital image correlation.* Experimental Mechanics, 2001. **41**(1): p. 29-39.

38. Tung, S.-H., M.-H. Shih, and J.-C. Kuo, *Application of digital image correlation for anisotropic plastic deformation during tension testing.* Optics and Lasers in Engineering, 2010. **48**(5): p. 636-641.

39. Wang, K., et al., *Measuring forming limit strains with digital image correlation analysis.* Journal of Materials Processing Technology, 2014. **214**(5): p. 1120-1130.

40. Fu, S., et al., *Study on the out-of-plane deformation of the Portevin–Le Chatelier band by using digital shearography.* Measurement, 2015. **72**(0): p. 61-67.

41. Swaminathan, B., et al., *Investigation using digital image correlation of Portevin-Le Chatelier Effect in Hastelloy X under thermo-mechanical loading.* International Journal of Plasticity, 2015. **64**(0): p. 177-192.

42. Lyons, J.S., J. Liu, and M.A. Sutton, *High-temperature deformation measurements using digital-image correlation.* Experimental Mechanics, 1996. **36**(1): p. 64-70.

43. Hammer, J.T., J.D. Seidt, and A. Gilat, *Strain Measurement at Temperatures Up to 800°C Utilizing Digital Image Correlation*, in *Advancement of Optical Methods in Experimental Mechanics, Volume 3*, H. Jin, et al., Editors. 2014, Springer International Publishing. p. 167-170.

44. Jun Hu, N.Z., Fadi Abu-Farha, *Revealing Dynamic Banding During High Temperature Deformation of Lightweight Materials Using Digital Image Correlation* in *SEM Annual Conference And Exposition On Experimental And Applied Mechanics*. 2015: Costa Mesa, CA USA.

45. Pan, B., et al., *High-temperature digital image correlation method for full-field deformation measurement at 1200 C.* Measurement science and technology, 2011. **22**(1): p. 015701.

46. Grant, B., et al., *High-temperature strain field measurement using digital image correlation.* The Journal of Strain Analysis for Engineering Design, 2009. **44**(4): p. 263-271.

47. Abu-Farha, F. and R. Curtis, *Quick-mount grips: Towards an improved standard for uniaxial tensile testing of metallic superplastic sheets.* Materialwissenschaft und Werkstofftechnik, 2009. **40**(11): p. 836.

48. Kabirian, F., A.S. Khan, and A. Pandey, *Negative to positive strain rate sensitivity in 5xxx series aluminum alloys: Experiment and constitutive modeling.* International Journal of Plasticity, 2014. **55**(0): p. 232-246.

49. Morris, J.G., *Dynamic strain aging in aluminum alloys.* Materials Science and Engineering, 1974. **13**(2): p. 101-108.

50. Curtin, W.A., D.L. Olmsted, and L.G. Hector, Jr., *A predictive mechanism for dynamic strain ageing in aluminium-magnesium alloys.* Nat Mater, 2006. **5**(11): p. 875-80.

51. Hill, R., *A Theory of the Yielding and Plastic Flow of Anisotropic Metals.* Proceedings of the Royal Society of London.Series A, Mathematical and Physical Sciences, 1948. **193**(1033): p. 281-297.

52. Banabic, D. and K. Siegert, *Anisotropy and formability of AA5182-0 aluminium alloy sheets.* CIRP Annals - Manufacturing Technology, 2004. **53**(1): p. 219-222.

53. Barlat, F., et al., *Yield function development for aluminum alloy sheets.* Journal of the Mechanics and Physics of Solids, 1997. **45**(11–12): p. 1727-1763.

54. Barlat, F., et al., *Linear transfomation-based anisotropic yield functions.* International Journal of Plasticity, 2005. **21**(5): p. 1009-1039.

55. Barlat, F., et al., *Plane stress yield function for aluminum alloy sheets—part 1: theory.* International Journal of Plasticity, 2003. **19**(9): p. 1297-1319.

56. Barlat, F., et al., *A simple model for dislocation behavior, strain and strain rate hardening evolution in deforming aluminum alloys.* International Journal of Plasticity, 2002. **18**(7): p. 919-939.

57. Barlat, F., D.J. Lege, and J.C. Brem, *A six-component yield function for anisotropic materials.* International Journal of Plasticity, 1991. **7**(7): p. 693-712.

58. Lademo, O.G., O.S. Hopperstad, and M. Langseth, *An evaluation of yield criteria and flow rules for aluminium alloys.* International Journal of Plasticity, 1999. **15**(2): p. 191-208.

59. Boogaard van den, A.H., P.J. Bolt, and R.J. Werkhoven, *Aluminium sheet forming at elevated temperatures*, in *International Conference on Numerical Methods in Industrial Forming Processes, NUMIFORM 2001*. 2001: Toyohashi, Japan.

60. Naka, T., et al., *Effects of temperature on yield locus for 5083 aluminum alloy sheet.* Journal of Materials Processing Technology, 2003. **140**(1–3): p. 494-499.

61. Sherby, O.D. and P.M. Burke, *Mechanical behavior of crystalline solids at elevated temperature.* Progress in Materials Science, 1968. **13**(0): p. 323-390.

62. Taleff, E.M. and P.J. Nevland, *The high-temperature deformation and tensile ductility of Al alloys.* JOM, 1999. **51**(1): p. 34-36.

63. McQueen, H.J. and N.D. Ryan, *Constitutive analysis in hot working.* Materials Science and Engineering: A, 2002. **322**(1–2): p. 43-63.

64. Le Chatelier, A., *Influence du temps et de la température sur les essais au choc.* Revue de métallurgie, 1909. **6**: p. 914-917.

65. Thevenet, D., M. Mliha-Touati, and A. Zeghloul, *Characteristics of the propagating deformation bands associated with the Portevin–Le Chatelier effect in an Al–Zn–Mg–Cu alloy.* Materials Science and Engineering: A, 2000. **291**(1–2): p. 110-117.

66. Bolt, P.J., R.J. Werkhoven, and v.d. Boogaard. *Effect of elevated temperatures on the drawability of aluminium sheet components*.

67. Halim, H., D.S. Wilkinson, and M. Niewczas, *The Portevin–Le Chatelier (PLC) effect and shear band formation in an AA5754 alloy.* Acta Materialia, 2007. **55**(12): p. 4151-4160.

68. Feng, X., et al., *Investigation of PLC band nucleation in AA5754.* Materials Science and Engineering: A, 2012. **539**(0): p. 205-210.

69. Kubin, L.P. and Y. Estrin, *The portevin-Le Chatelier effect in deformation with constant stress rate.* Acta Metallurgica, 1985. **33**(3): p. 397-407.

70. Atkinson, M., *Accurate determination of biaxial stress—strain relationships from hydraulic bulging tests of sheet metals.* International Journal of Mechanical Sciences, 1997. **39**(7): p. 761-769.

71. Güner, A., A. Brosius, and A.E. Tekkaya, *Analysis of the hydraulic bulge test with FEA concerning the accuracy of the determined flow curves.* Key Engineering Materials, 2009. **410**: p. 439-447.

72. Gutscher, G., et al., *Determination of flow stress for sheet metal forming using the viscous pressure bulge (VPB) test.* Containing research papers on Sheet Forming, Machining and Tube Hydroforming, 2004. **146**(1): p. 1-7.

73. Kaya, S., et al., *Determination of the flow stress of magnesium AZ31-O sheet at elevated temperatures using the hydraulic bulge test.* International Journal of Machine Tools and Manufacture, 2008. **48**(5): p. 550-557.

74. Koç, M., E. Billur, and Ö.N. Cora, *An experimental study on the comparative assessment of hydraulic bulge test analysis methods.* Materials & Design, 2011. **32**(1): p. 272-281.

75. Lăzărescu, L., D.S. Comşa, and D. Banabic, *Determination of Stress-Strain Curves of Sheet Metals by Hydraulic Bulge Test.* AIP Conference Proceedings, 2011. **1353**(1): p. 1429-1434.

76. LĂZĂRescu, L., et al., *Characterization of plastic behaviour of sheet metals by hydraulic bulge test.* Transactions of Nonferrous Metals Society of China, 2012. **22, Supplement 2**(0): p. s275-s279.

77. Sigvant, M., et al., *A viscous pressure bulge test for the determination of a plastic hardening curve and equibiaxial material data.* International Journal of Material Forming, 2009. **2**(4): p. 235-242.

78. Rees, D.W.A., *Plastic flow in the elliptical bulge test.* International Journal of Mechanical Sciences, 1995. **37**(4): p. 373-389.

79. Hwang, Y.-M., Y.-K. Lin, and H.-C. Chuang, *Forming limit diagrams of tubular materials by bulge tests.* Journal of Materials Processing Technology, 2009. **209**(11): p. 5024-5034.

80. Banabic, D., et al., *Development of a new procedure for the experimental determination of the Forming Limit Curves.* CIRP Annals - Manufacturing Technology, 2013. **62**(1): p. 255-258.

81. Lin, Y.C. and X.-M. Chen, *A critical review of experimental results and constitutive descriptions for metals and alloys in hot working.* Materials & Design, 2011. **32**(4): p. 1733-1759.

82. Toros, S. and F. Ozturk, *Modeling uniaxial, temperature and strain rate dependent behavior of Al–Mg alloys.* Computational Materials Science, 2010. **49**(2): p. 333-339.

83. Alankar, A. and M.A. Wells, *Constitutive behavior of as-cast aluminum alloys AA3104, AA5182 and AA6111 at below solidus temperatures.* Materials Science and Engineering: A, 2010. **527**(29–30): p. 7812-7820.

84. Haaften, W.M., et al., *Constitutive behavior of as-cast AA1050, AA3104, and AA5182.* Metallurgical and Materials Transactions A, 2002. **33**(7): p. 1971-1980.

85. Cheng, Y.Q., et al., *Flow stress equation of AZ31 magnesium alloy sheet during warm tensile deformation.* Journal of Materials Processing Technology, 2008. **208**(1–3): p. 29-34.

86. Xing, Z.W., J. Bao, and Y.Y. Yang, *Numerical simulation of hot stamping of quenchable boron steel.* Fifth International Conference on Physical and Numerical Simulations of Material Processing (ICPNS 2007) held at Zhengzhou, China, October 23-27, 2007, 2009. **499**(1–2): p. 28-31.

87. Johnson, G.R. and W.H. Cook. *A constitutive model and data for metals subjected to large strains, high strain rates and high temperatures*. in *Proceedings of the 7th International Symposium on Ballistics*. 1983. The Netherlands.

88. Vural, M. and J. Caro, *Experimental analysis and constitutive modeling for the newly developed 2139-T8 alloy.* Materials Science and Engineering: A, 2009. **520**(1–2): p. 56-65.

89. Khan, A.S. and S. Huang, *Experimental and theoretical study of mechanical behavior of 1100 aluminum in the strain rate range 10−5−104s−1.* International Journal of Plasticity, 1992. **8**(4): p. 397-424.

90. Khan, A.S. and M. Baig, *Anisotropic responses, constitutive modeling and the effects of strain-rate and temperature on the formability of an aluminum alloy.* International Journal of Plasticity, 2011. **27**(4): p. 522-538.

91. Khan, A.S. and H. Liu, *Variable strain rate sensitivity in an aluminum alloy: Response and constitutive modeling.* International Journal of Plasticity, 2012. **36**(0): p. 1-14.

92. Khan, A.S. and C.S. Meredith, *Thermo-mechanical response of Al 6061 with and without equal channel angular pressing (ECAP).* International Journal of Plasticity, 2010. **26**(2): p. 189-203.

93. Chaboche, J.L., *A review of some plasticity and viscoplasticity constitutive theories.* International Journal of Plasticity, 2008. **24**(10): p. 1642-1693.

94. Abedrabbo, N., F. Pourboghrat, and J. Carsley, *Forming of aluminum alloys at elevated temperatures – Part 1: Material characterization.* International Journal of Plasticity, 2006. **22**(2): p. 314-341.

95. Abedrabbo, N., F. Pourboghrat, and J. Carsley, *Forming of aluminum alloys at elevated temperatures – Part 2: Numerical modeling and experimental verification.* International Journal of Plasticity, 2006. **22**(2): p. 342-373.

96. Dion‐Martin, O., et al., *Characterization of AA5754 Alloy for Identification of Barlat's YLD2000‐2d Yield Criterion.* Characterization of Minerals, Metals, and Materials 2013, 2013: p. 53-65.

97. Keeler, S.P. and W.A. Backofen, *Plastic instability and fracture in sheets stretched over rigid punches.* Asm Trans Q, 1963. **56**(1): p. 25-48.

98. Graf, A. and W. Hosford, *Effect of changing strain paths on.* Metallurgical Transactions A, 1993. **24**(11): p. 2503-2512.

99. Kleemola, H. and M. Pelkkikangas, *Effect of predeformation and strain path on the forming limits of steel, copper and brass.* Sheet Met Ind, 1977. **64**(6): p. 591-592.

100. Simha, C.H.M., R. Grantab, and M.J. Worswick, *Computational analysis of stress-based forming limit curves.* International Journal of Solids and Structures, 2007. **44**(25–26): p. 8663-8684.

101. Stoughton, T.B., *Stress-Based Forming Limits in Sheet-Metal Forming.* Journal of Engineering Materials and Technology, 2000. **123**(4): p. 417-422.

102. Stoughton, T.B., *A general forming limit criterion for sheet metal forming.* International Journal of Mechanical Sciences, 2000. **42**(1): p. 1-27.

103. Stoughton, T.B., *A non-associated flow rule for sheet metal forming.* International Journal of Plasticity, 2002. **18**(5–6): p. 687-714.

104. Stoughton, T.B. and J.W. Yoon, *Sheet metal formability analysis for anisotropic materials under non-proportional loading.* International Journal of Mechanical Sciences, 2005. **47**(12): p. 1972-2002.

105. Stoughton, T.B. and X. Zhu, *Review of theoretical models of the strain-based FLD and their relevance to the stress-based FLD.* International Journal of Plasticity, 2004. **20**(8–9): p. 1463-1486.

106. Marciniak, Z. and K. Kuczyński, *Limit strains in the processes of stretch-forming sheet metal.* International Journal of Mechanical Sciences, 1967. **9**(9): p. 609-620.

107. Ganjiani, M. and A. Assempour, *An improved analytical approach for determination of forming limit diagrams considering the effects of yield functions.* Journal of Materials Processing Technology, 2007. **182**(1–3): p. 598-607.

108. Ganjiani, M. and A. Assempour, *Implementation of a Robust Algorithm for Prediction of Forming Limit Diagrams.* Journal of Materials Engineering and Performance, 2008. **17**(1): p. 1-6.

109. Yao, H. and J. Cao, *Prediction of forming limit curves using an anisotropic yield function with prestrain induced backstress.* International Journal of Plasticity, 2002. **18**(8): p. 1013-1038.

110. Belhabib, S., et al., *Heterogeneous tensile test on elastoplastic metallic sheets: Comparison between FEM simulations and full-field strain measurements.* International Journal of Mechanical Sciences, 2008. **50**(1): p. 14-21.

111. Chen, X., et al. *The coupled thermo-mechanical-microstructural finite element modeling of hot stamping process in 22MnB5 steel*. in *NUMISHEET 2014: The 9th International Conference and Workshop on Numerical Simulation of 3D Sheet Metal Forming Processes: Part A Benchmark Problems and Results and Part B General Papers*. 2013. AIP Publishing.

112. Del Prete, A., T. Primo, and M. Strano, *The use of FEA packages in the simulation of a drawing operation with springback, in the presence of random uncertainty.* Finite Elements in Analysis and Design, 2010. **46**(7): p. 527-534.

113. Makinouchi, A., *Sheet metal forming simulation in industry.* Proceedings of the 6th International Conference on Metal Forming, 1996. **60**(1–4): p. 19-26.

114. Palaniswamy, H., G. Ngaile, and T. Altan, *Finite element simulation of magnesium alloy sheet forming at elevated temperatures.* Containing research papers on Sheet Forming, Machining and Tube Hydroforming, 2004. **146**(1): p. 52-60.

115. van den Boogaard, A.H. and J. Huétink, *Simulation of aluminium sheet forming at elevated temperatures.* Computational Metal Forming, 2006. **195**(48–49): p. 6691-6709.

116. Armero, F. and J.C. Simo, *A priori stability estimates and unconditionally stable product formula algorithms for nonlinear coupled thermoplasticity.* International Journal of Plasticity, 1993. **9**(6): p. 749-782.

117. Ortiz, M. and J. Simo, *An analysis of a new class of integration algorithms for elastoplastic constitutive relations.* International Journal for Numerical Methods in Engineering, 1986. **23**(3): p. 353-366.

118. Simo, J.C. and M. Ortiz, *A unified approach to finite deformation elastoplastic analysis based on the use of hyperelastic constitutive equations.* Computer Methods in Applied Mechanics and Engineering, 1985. **49**(2): p. 221-245.

119. Hashiguchi, K., *Generalized plastic flow rule.* International Journal of Plasticity, 2005. **21**(2): p. 321-351.

120. Tuğcu, P. and K.W. Neale, *On the implementation of anisotropic yield functions into finite strain problems of sheet metal forming.* International Journal of Plasticity, 1999. **15**(10): p. 1021-1040.

121. Lee, S.W., J.W. Yoon, and D.Y. Yang, *A stress integration algorithm for plane stress elastoplasticity and its applications to explicit finite element analysis of sheet metal forming processes.* Computers & Structures, 1998. **66**(2–3): p. 301-311.

122. Abedrabbo, N., *Forming of Aluminum Alloys at Elevated Temperatures*, in *Department of Mechanical Engineering*. 2005, Michigan State University.

123. Hughes, T.J.R. and E. Carnoy, *Nonlinear finite element shell formulation accounting for large membrane strains.* Computer Methods in Applied Mechanics and Engineering, 1983. **39**(1): p. 69-82.

124. Ponthot, J.P., *Unified stress update algorithms for the numerical simulation of large deformation elasto-plastic and elasto-viscoplastic processes.* International Journal of Plasticity, 2002. **18**(1): p. 91-126.

125. Fotiu, P.A. and S. Nemat-Nasser, *A universal integration algorithm for rate-dependent elastoplasticity.* Computers & Structures, 1996. **59**(6): p. 1173-1184.

126. Saleeb, A.F., T.E. Wilt, and W. Li, *An Implicit integration scheme for generalized viscoplasticity with dynamic recovery.* Computational Mechanics, 1998. **21**(6): p. 429-440.